# Electrically-Small Antenna Performance Enhancement for Near-Field Detuning Environments

Christian W. Hearn

Dissertation submitted to the Faculty of
The Virginia Polytechnic Institute and State University
in partial fulfillment of the requirements for the degree of

Doctor of Philosophy
in
Electrical Engineering

William A. Davis, Chair
Warren L. Stutzman
Majid Manteghi
Timothy Pratt
Werner Kohler

October 25, 2012
Blacksburg, Virginia

Keywords: Multi-resonant small antenna, spherical mode decomposition

Electrically-Small Antenna Performance Enhancement for Near-Field Detuning Environments

Christian W. Hearn

## ABSTRACT

Bandwidth enhancement of low-profile omnidirectional, electrically-small antennas has evolved from the design and construction of AM transmitter towers eighty years ago to current market demand for battery-powered personal communication devices. Electrically-small antenna theory developed with well-known approximations for characterizing radiation properties of antenna structures that are fractions of the radiansphere. Current state-of-the-art wideband small antennas near $ka \approx 1$ have achieved multiple-octave impedance bandwidths when utilizing volume-efficient designs.

Significant advances in both the power and miniaturization of microelectronics have created a second possible approach to enhance bandwidth. Frequency agility, via switch tuning of reconfigurable structures, offers the possibility of the direct integration of high-speed electronics to the antenna structure. The potential result would provide a means to translate a narrow instantaneous bandwidth across a wider operating bandwidth.

One objective of the research was to create a direct comparison of the passive- multi-resonant and active-reconfigurable approaches to enhance bandwidth. Typically, volume-efficient, wideband antennas are unattractive candidates for low-profile applications and conversely, active electronics integrated directly antenna elements continue to introduce problematic loss mechanisms at the proof-of-concept level.

The dissertation presents an analysis method for wide bandwidth self-resonant antennas that exist in the $0.5 \leq ka \leq 1.0$ range. The combined approach utilizes the quality factor extracted directly from impedance response data in addition to near-and-far field modal analyses. Examples from several classes of antennas investigated are presented with practical boundary conditions. The resultant radiation properties of these antenna-finite ground plane systems are characterized by an appreciable percentage of radiated power outside the lowest-order mode.

Volume-efficient structures and non-omnidirectional radiation characteristics are generally not viable for portable devices. Several examples of passive structures, representing different antenna classes are investigated. A PIN diode, switch-tuned low-profile antenna prototype was also developed for the comparison which demonstrated excessive loss in the physical prototype.

Lastly, a passive, low-profile multi-resonant antenna element with monopole radiation is introduced. The structure is an extension of the planar inverted-F antenna with the addition of a capacitance-coupled parasitic to enhance reliable operation in unknown environments.

# ACKNOWLEDGEMENTS

I would like to thank Dr. William A. Davis who served as my committee chairman, advisor, and mentor for the past four years. Not only am I indebted to him for the opportunity to return as a Ph.D. student in the Virginia Tech Antenna Group, but he has also served as an inspiration for his expertise in multiple technical areas.

The award of an engineering Ph.D. to a non-traditional student at mid-career may be considered a testament to the student's patience and persistence. In this particular case, obstinance is a more accurate description. However, the ultimate achievement would not have been possible without support, guidance and mentorship from an impressive roster of professional role models along the way. During the course of my technical career, it has been a distinct honor and privilege to have studied under the directions of Mr. John D. Gordon (retired physicist-NSWC-Carderock, UERD), Dr. William D. Stanley (Eminent Professor Emeritus-ODU), and Mr. Thomas G. Campbell (IEEE Fellow-Advanced Program Director, Applied EM, Inc.).

I am grateful for the support provided by Dr. C.J. Reddy and senior staff at Applied EM, Incorporated. The collaborative relationship between the Virginia Tech Antenna Group, Applied EM Inc., and ZAI, facilitated by Dr. Kevin Baugh, was a lifeline for a significant portion of the dissertation research.

Both my heartfelt gratitude and love belong to my wife Kimberly. Her support, empathy and patience during this academic odyssey kept our family on course with eyes on the finish line. Finally, I am grateful to my entire family, including my father, my dear aunt, my in-laws and the extended family, for their unwavering trust as I climbed higher and higher up the academic mountain. Thank you.

# TABLE OF CONTENTS


1 CHAPTER - Introduction ..... 1

1.1 Overview of Dissertation 2

1.2 References 4

2 CHAPTER - Background ..... 5

2.1 Introduction 5

2.2 Finite Ground Plane Detuning 8

2.3 Low Profile Antenna Solutions - Small versus Low-Profile 10

2.3.1 Planar Inverted-F Antenna 11

2.3.2 Microstrip Antenna 13

2.4 Active Reconfigurable Narrowband Structures 17

2.5 Wideband Electrically-Small Antennas 19

2.6 Summary 21

2.7 References 21

3 CHAPTER - Approach/Tools ..... 23

3.1 Introduction 23

3.2 Analysis Tools - Q and Spherical Mode Decomposition 24

3.2.1 Quality Factor 24

3.2.2 Spherical Mode Decomposition 26

3.3 Examples of Approach 28

3.3.1 Electrically-Small Antenna Ground Plane Interaction - Modal Analysis 29

3.3.2 Far-field versus Near-field Spherical Mode Decomposition 30

3.4 Low-Profile Example – Microstrip Patch Antenna 32

3.5 Summary 36

3.6 References 36

4 CHAPTER - Narrowband Reconfigurable, Active Antenna Systems ..... 38

4.1 Introduction 38

4.2 Short Monopole Placement in Handheld Device Configuration 39

4.3 Planar Inverted-F Antenna 42

4.3.1 Height Reduction Discussion 47

4.3.2 Miniaturization - Single Resonant Antennas 55
4.4 Switch-Tuned PIFA 60
4.5 Conclusions 65
4.6 References 65
5 CHAPTER - Wideband ESA Models ..... 67
5.1 Introduction 67
5.2 Multi-resonant Spiral 68
5.3 Ravipati Antenna 72
5.4 Wideband Compact J-Pole Antenna 78
5.5 Multi-Resonant Patch - U-Slot Antenna 84
5.5.1 Sensitivity to Finite Ground Plane 88
5.5.2 Discussion - U-Slot Microstrip Patch Antenna 89
5.6 Conclusions 89
5.7 References 90
6 CHAPTER - Hardware Technologies ..... 91
6.1 Introduction 91
6.2 High Efficiency Power Amplifiers for Portable Applications 92
6.3 Integrated Inverse Class-F Amplifier Design with low-profile PIFA 92
6.4 Hardware Evaluation 96
6.5 Summary 100
6.6 References 101
7 CHAPTER - Multi-resonant Low-Profile Example ..... 102
7.1 Introduction 102
7.2 The Antenna Structure 102
7.3 Summary 113
7.4 References 113
8 Chapter - Conclusions ..... 115
8.1 Summary 115
8.2 Contributions 117
8.3 Future work 118
8.4 References 118

# LIST OF FIGURES


FIG. 2.1. SCHEMATIC DIAGRAM OF A VERTICALLY-POLARIZED OMNIDIRECTIONAL ANTENNA ENCLOSED BY A SPHERE RADIUS $P=A$, CENTERED ABOUT THE ORIGIN.....5

FIG. 2.2. CAPACITOR AND INDUCTOR OCCUPYING EQUAL CYLINDRICAL VOLUMES. .....6

FIG. 2.3. COMPLEX IMPEDANCE VERSUS DIAMETER OF GROUND PLANE FOR $1<D/\Lambda<10$ FOR A $\Lambda/4$ MONOPOLE. .....8

FIG. 2.4. CADFEKO RENDERING OF DISK-LOADED MONOPOLE.....9

FIG. 2.5. RETURN LOSS (A) AND FRACTIONAL DETUNING (B) VERSUS RADIUS OF GROUND PLANE. .....10

FIG. 2.6. INVERTED-F ANTENNA FORMED FROM A BENT MONOPOLE WITH OFFSET FEED. .....11

FIG. 2.7. CADFEKO RENDERING OF A CONVENTIONAL PIFA SCALED TO $F=1.0$ GHZ. .....12

FIG. 2.8. SMITH CHART (A) AND COMPUTED VSWR (B) OF THE CONVENTIONAL PIFA SHOWN IN FIG. 2.7.....13

FIG. 2.9. $E_\Theta$ AND $E_\Phi$ RADIATION PATTERNS COMPUTED USING FEKO FOR THE CONVENTIONAL PIFA SHOWN IN FIG. 2.7.....13

FIG. 2.10. CADFEKO RENDERING OF A PROBE-FED, SQUARE MICROSTRIP PATCH ANTENNA MOUNTED ON A FINITE GROUND PLANE, $S \approx \Lambda$. .....15

FIG. 2.11. COMPLEX IMPEDANCE RESPONSE OF SQUARE MICROSTRIP PATCH ANTENNA (SHOWN IN FIG. 2.10) MOUNTED ON A FINITE GROUND PLANE, $S \approx \Lambda$ .....16

FIG. 2.12. $E_\Theta$ AND $E_\Phi$ RADIATION PATTERNS ($F=1.0$ GHZ) CALCULATED USING FEKO FOR THE SQUARE MICROSTRIP PATCH ANTENNA (SHOWN IN FIG. 2.10) MOUNTED ON A FINITE GROUND PLANE, $S \approx \Lambda$. .....16

FIG. 2.13. ILLUSTRATION OF MINIMUM ANTENNA DIMENSION FOR NOMINAL SYSTEM BANDWIDTH......18

FIG. 2.14. CADFEKO RENDERING OF RAVIPATI WIDEBAND ESA WITH THREE DOUBLE-TUNING STRUCTURES.....20

FIG. 2.15. VSWR RESPONSES ILLUSTRATING THE WIDEBAND ESA ANTENNA DESIGN.. .....20

FIG. 3.1. THREE-DIMENSIONAL $E_\Theta$ AND $E_\Phi$ RADIATION PATTERNS FROM A SINGLE $TM_{MN}$ SOURCE FOR $M \leq N$, $N=[1,2,3]$. .....28

FIG. 3.2. $E_\Theta$ MODE COMPONENTS FOR $TM_{0N}$.....29

FIG. 3.3. GEOMETRY AND MODAL COMPOSITIONS FOR IDENTICAL SHORT MONOPOLE ELEMENTS AT THE CENTERS OF SQUARE AND CIRCULAR SMALL GROUND PLANES. .....30

FIG. 3.4. CADFEKO RENDERING OF SHORT MONOPOLE OF FINITE GROUND PLANE.....31

FIG. 3.5. NEAR-FIELD TO FAR-FIELD MODAL POWER COMPOSITIONS VERSUS $\kappa R$ FOR $S_{GP}$ OF $2A=\Lambda/\Pi$ AND $\Lambda$.....32

FIG. 3.6. A PROBE-FED, SQUARE MICROSTRIP PATCH ANTENNA MOUNTED ON A FINITE GROUND PLANE, $S \approx \Lambda$. .....33

FIG. 3.7. CALCULATED COMPLEX IMPEDANCE RESPONSE (A) AND VSWR (B) OF SQUARE MICROSTRIP PATCH ANTENNA MOUNTED ON A FINITE GROUND PLANE, $S_{GP} \approx \Lambda$.. .....34

FIG. 3.8. SMITH CHART IMPEDANCE RESPONSE FOR THE SQUARE MICROSTRIP PATCH ANTENNA GEOMETRY SHOWN IN FIG. 3.6 MOUNTED ON A FINITE GROUND PLANE.. .....35

FIG. 4.1. CADFEKO RENDERINGS OF CENTER-MOUNTED (A) AND EDGE-MOUNTED (B) SHORT MONOPOLE INTEGRATED TO A HANDHELD DEVICE. .....39

FIG. 4.2. THREE-DIMENSIONAL $E_\Theta$ AND $E_\Phi$ RADIATION PATTERNS FOR THE CENTER AND EDGE MOUNTED MONOPOLES. .....40

FIG. 4.3. NORMALIZED IMPEDANCE (A) AND VSWR (B) RESPONSES FOR CENTER-MOUNT AND EDGE-MOUNTED MONOPOLES ON A HANDHELD DEVICE SHOWN IN FIG. 4.2. ....41
FIG. 4.4. A THREE-VIEW CADFEKO RENDERING OF THE CONVENTIONAL PIFA MODEL. ....42
FIG. 4.5. SMITH CHART (A) AND COMPUTED VSWR (B) OF A CONVENTIONAL PIFA SHOWN IN FIG. 4.4. ....43
FIG. 4.6. THREE-DIMENSIONAL RADIATION PATTERNS FOR THE CONVENTIONAL PIFA SHOWN IN FIG. 4.4 ($S_{GP} = 0.4\lambda$).. ....44
FIG. 4.7. CADFEKO MODEL RENDERING OF CONVENTIONAL PIFA INTEGRATED TO A HANDHELD DEVICE. ....45
FIG. 4.8. NORMALIZED IMPEDANCE (A) AND VSWR (B) RESPONSES FOR PIFA INTEGRATED TO HANDHELD DEVICE. ....45
FIG 4.9. $E_\Theta$ AND $E_\Phi$ RADIATION PATTERNS FOR CONVENTIONAL PIFA MOUNTED ON HANDHELD STRUCTURE.. ....46
FIG. 4.10. CADFEKO RENDERING OF CAPACITIVE-LOAD PIFA OVER AN INFINITE GROUND PLANE. ....48
FIG. 4.11. CALCULATED IMPEDANCE RESPONSE FOR PIFA RESPONSE, $H=\lambda/35$ TUNED TO RESONANCE AT $F_R=1.0$ GHZ (SEE FIG. 4.10).. ....48
FIG. 4.12. RETURN LOSS AND VSWR RESPONSE SHOWN IN FIG. 4.10 FOR THE PIFA WITH $H=\lambda/35$.. ....49
FIG. 4.13. CADFEKO RENDERING OF PIFA GEOMETRY WITH DIMENSIONS SHOWN IN UNITS OF WAVELENGTH. ....50
FIG. 4.14. CALCULATED $Q_A$ VALUES FOR THE MODEL (SHOWN IN FIG. 4.10) VERSUS ELECTRICAL SIZE $KA$. ....52
FIG. 4.15. CADFEKO RENDERING OF MINIMUM HEIGHT ($H=\lambda/60$), PIFA CONFIGURED ON HANDHELD DEVICE ....53
FIG. 4.16. $E_\Theta$ AND $E_\Phi$ RADIATION PATTERNS FOR MINIMUM HEIGHT FOR THE MINIMUM HEIGHT PIFA, SHOWN IN FIG. 4.15, MOUNTED ON HANDHELD STRUCTURE.. ....54
FIG. 4.17. REPRESENTATIVE ILLUSTRATION OF SLOT-LOADING MINIATURIZATION TECHNIQUE.. ....56
FIG. 4.18. SIDE VIEW CADFEKO MODEL OF PIFA WITH CAPACITIVE LOADING. ....57
FIG. 4.19. CADFEKO RENDERING OF A CONVENTIONAL PIFA WITH CAPACITIVE-LOAD AND MEANDERING FOR MINIATURIZATION. ....57
FIG. 4.20. RETURN LOSS RESPONSES FOR CONVENTIONAL PIFA SHOWN IN FIG. 4.19 FOR THE MINIATURIZATION CONFIGURATIONS. ....59
FIG. 4.21. QUALITY FACTOR VERSUS ELECTRICAL SIZE ($KA$) FOR PIFA MINIATURIZATION CONFIGURATIONS SHOWN IN FIG. 4.19. ....59
FIG. 4.22. ENGINEERING PERSPECTIVE OF THE SWITCH-TUNED PIFA MODEL CREATED IN CADFEKO. ....61
FIG. 4.23. RETURN LOSS RESPONSES FOR THE ACTIVE, SWITCH-TUNED PIFA SHOWN IN FIG. 4.22. ....62
FIG. 4.24. SWITCH-TUNED PIFA WITH CONTROL BOX AND ORIGINAL LENGTH RIBBON CABLE. ....62
FIG. 4.25. VTAG ORIGINAL TEST SETUP OF THE SWITCH-TUNED PIFA SHOWN IN FIG. 4.24 MOUNTED ON A FINITE GROUND PLANE OF DIAMETER $D_{GP} \approx \lambda$. ....63
FIG. 4.26. TOP-VIEW (A) AND SIDE-VIEW (B) OF ACTIVE, SWITCH-TUNED PIFA CADFEKO MODEL WITH CIRCULAR FINITE GROUND PLANE AND SWITCH DETAIL ....64
FIG. 4.27. IDEAL SWITCH SIMULATED RETURN LOSS (A) AND ACTIVE-SWITCH MEASURED RETURN LOSS RESPONSES.. ....64
FIG. 5.1. ENGINEERING PERSPECTIVES SHOWN OF THE STUART-BEST MULTI-RESONANT SPIRAL GENERATED IN CADFEKO. ....68
FIG. 5.2. CALCULATED SMITH CHART (A) AND VSWR (B) RESPONSES FOR DOUBLE-RESONANT SPIRAL COMPRISED OF 2, 4, 6, AND 8 ARMS.. ....69
FIG. 5.3. MULTI-RESONANT SPIRAL (A) GEOMETRY (SEE FIG. 5.1) AND (B) COMPLEX IMPEDANCE RESPONSE. ....70

FIG. 5.4. RESONANCE-TUNED IMPEDANCE RESPONSES AND VSWR RESPONSES FOR THE MULTI-RESONANT SPIRAL ANTENNA EXAMPLE SHOWN IN FIG. 5.1. ....70
FIG. 5.5. THREE-DIMENSIONAL $E_\theta$ AND $E_\Phi$ RADIATION PATTERNS FOR THE MULTI-RESONANT SPIRAL ANTENNA EXAMPLE SHOWN IN FIG. 5.1. ....71
FIG. 5.6. CADFEKO GEOMETRY OF RAVIPATI ANTENNA.. ....73
FIG. 5.7. SIMULATED INPUT IMPEDANCE RESPONSE FOR THE RAVIPATI WIDEBAND ANTENNA WITH DOUBLE-TUNING STRUCTURES..74
FIG. 5.8. $E_\theta$ AND $E_\Phi$ DIRECTIVITY PATTERNS OF THE RAVIPATI ANTENNA (SHOWN IN FIG. 5.6) MOUNTED ON A FINITE GROUND PLANE $S_{GP}=0.4\lambda$ AT $f=1.0$ GHZ. ....74
FIG. 5.9. CADFEKO RENDERING OF THE (A) RAVIPATI ANTENNA SHOWN IN FIG. 5.6 WITH THE CALCULATED SMITH CHART IMPEDANCE RESPONSE (B). ....76
FIG. 5.10. $E_\theta$ MODE COMPONENTS SHOWN FOR $TM_{0N}$. ....76
FIG. 5.11. LOW AND HIGH FREQUENCY *TM* PERCENT POWER MODE DISTRIBUTIONS FOR RAVIPATI ANTENNA ON SMALL FINITE GROUND PLANE – $S_{GP}=2A$. ....77
FIG. 5.12 LOW AND HIGH FREQUENCY TM PERCENT POWER MODE DISTRIBUTIONS FOR RAVIPATI ANTENNA ON FINITE GROUND PLANE – $S_{GP}=\lambda$. ....77
FIG. 5.13. CADFEKO RENDERING OF WIDEBAND COMPACT (WC) J-POLE ANTENNA. ....79
FIG. 5.14. SIMULATED INPUT IMPEDANCE (A) AND VSWR RESPONSE (B) FOR WIDEBAND COMPACT J-POLE ANTENNA SHOWN IN FIG. 5.13. ....80
FIG. 5.15. $E_\theta$ AND $E_\Phi$ DIRECTIVITIES FOR WIDEBAND COMPACT J-POLE ANTENNA.. ....80
FIG. 5.16. CADFEKO RENDERING OF WC J-POLE ANTENNA MOUNTED ON HANDHELD WITH SAME FORM-FACTOR AS ORIGINAL BASE PLATE. ....81
FIG. 5.17. SMITH CHART AND VSWR RESPONSES OF WC J-POLE ANTENNA ON ORIGINAL BASEPLATE (SOLID) AND MOUNTED ON THE HAND-HELD FIXTURE SHOWN IN THE PREVIOUS FIGURE (DASHED).. ....82
FIG. 5.18. $E_\theta$ AND $E_\Phi$ DIRECTIVITIES FOR THE WIDEBAND COMPACT J-POLE ANTENNA MOUNTED ON A HANDHELD FIXTURE, $f_o=1.0$ GHZ.. ....83
FIG. 5.19. CADFEKO RENDERING OF THE U-SLOT MICROSTRIP ANTENNA MODEL. ....85
FIG. 5.20. COMPOSITE VSWR RESPONSES OF THE RADIATION COMPONENTS OF THE U-SLOT MICROSTRIP ANTENNA. ....86
FIG. 5.21. $E_\theta$ AND $E_\Phi$ DIRECTIVITIES FOR THE U-SLOT MICROSTRIP ANTENNA MOUNTED ON A FINITE GROUND PLANE AT $f=1.0$ GHZ (SEE FIG. 5.19).. ....87
FIG. 5.22. $E_\theta$ AND $E_\Phi$ DIRECTIVITIES FOR THE SQUARE MICROSTRIP PATCH ANTENNA MOUNTED ON A FINITE GROUND PLANE AT $f=1.0$ GHZ (SEE FIG. 3.6). ....87
FIG. 5.23. CADFEKO RENDERING OF U-SLOT MICROSTRIP ANTENNA MOUNTED ON SMALL SQUARE GROUND PLANE. ....88
FIG. 5.24. SMITH CHART (A) AND VSWR (B) RESPONSES OF U-SLOT MICROSTRIP ANTENNA ON MINIMUM SQUARE GROUND PLANE. ....89
FIG. 6.1. THREE-VIEW ILLUSTRATION OF PIFA FEKO MODEL DESIGNED FOR INVERSE CLASS-F AMPLIFIER INTEGRATION.. ....94

FIG. 6.2. COMPLEX IMPEDANCE RESPONSES VERSUS SHORTING PIN FOR THE PIFA MODEL (SHOWN IN FIG. 6.1) DESIGNED FOR INTEGRATION TO AN INVERSE CLASS-F AMPLIFIER.. ....95
FIG. 6.3. SMITH CHART FORMAT OF HARMONIC-TUNED PIFA (SHOWN IN FIG. 6.1) OPTIMIZED FOR INVERSE CLASS-F AMPLIFIER INTEGRATION. ....96
FIG. 6.4. CADFEKO RENDERING OF SWITCH-TUNED PIFA WITH CAPACITIVE-LOADING. ....98
FIG. 6.5. IDEAL SWITCH SIMULATED RETURN LOSS (A) AND ACTIVE-SWITCH MEASURED RETURN LOSS RESPONSES. ....99
FIG. 7.1. CADFEKO RENDERING OF MULTI-RESONANT PLANAR INVERTED-F ANTENNA....103
FIG. 7.2. NORMALIZED IMPEDANCE (A) AND VSWR (B) RESPONSES FOR MULTI-RESONANT (SOLID – SEE FIG. 7.1) AND SINGLE-RESONANT (DASHED) PLANAR INVERTED-F ANTENNAS WITH SIMILAR FORM-FACTORS. ....104
FIG. 7.3. VSWR RESPONSE VERSUS SLOT-HEIGHT ON PIFA VERTICAL SHORTING BAR....104
FIG. 7.4. VSWR RESPONSE VERSUS SLOT-WIDTH ON PIFA. ....105
FIG. 7.5. THREE-DIMENSIONAL $E_{\Theta}$ (A) AND $E_{\Phi}$ (B) RADIATION PATTERNS FOR THE MULTI-RESONANT PIFA MOUNTED ON A SQUARE FINITE GROUND PLANE $S_{GP}=\lambda$. ....106
FIG. 7.6. FAR-FIELD *TM* AND *TE* MODE COMPOSITIONS FOR MULTI-RESONANT PIFA MOUNTED ON A FINITE GROUND PLANE $S_{GP}=\lambda$.. ....107
FIG. 7.7. CADFEKO RENDERINGS OF MULTI-RESONANT PIFA INTEGRATED TO A HANDHELD DEVICE.. ....108
FIG. 7.8. NORMALIZED IMPEDANCE (A) AND VSWR (B) RESPONSES FOR MULTI-RESONANT PLANAR INVERTED-F ANTENNA MOUNTED ON A HANDHELD DEVICE.. ....109
FIG. 7.9. $E_{\Theta}$ (A) AND $E_{\Phi}$ (B) RADIATION PATTERNS FOR THE MULTI-RESONANT PIFA MOUNTED ON AHANDHELD CHASSIS....110
FIG. 7.10. NORMALIZED IMPEDANCE (A) AND VSWR (B) RESPONSES FOR TUNED MULTI-RESONANT (BLACK-SOLID) AND SINGLE-RESONANT (BLUE-DASHED) PIFAS MOUNTED ON THE HANDHELD CHASSIS.. ....111
FIG. 7.11. SURFACE CURRENT DISTRIBUTIONS ON HANDHELD PIFA GEOMETRY (SHOWN IN FIG. 7.7) FOR $\Omega_T=[0^o,90^o,180^o,270^o]$. ....112
FIG. 7.12. TANGENTIAL NEAR FIELDS IN SPHERICAL COORDINATES FOR THE HANDHELD PIFA GEOMETRY (SHOWN IN FIG. 7.7) FOR $\Omega_T=[0^o,90^o,180^o,270^o]$. ....113

# LIST OF TABLES


TABLE 1. DIMENSIONS OF THE *KA=0.5* DISK-LOADED MONOPOLE SHOWN IN FIG. 2.4 $R_{GP}=1.5A$. ....10

TABLE 2. DIMENSIONS OF THE CONVENTIONAL PIFA SHOWN IN FIG. 2.7. ....12

TABLE 3. DIMENSIONS AND MATERIAL PROPERTIES FOR THE SQUARE MICROSTRIP PATCH ANTENNA (SEE FIG. 2.10). ....15

TABLE 4. DIMENSIONS AND MATERIAL PROPERTIES FOR THE SQUARE MICROSTRIP PATCH ANTENNA (SEE FIG. 3.6). ....33

TABLE 5. CALCULATED IMPEDANCE VALUES AT RESONANCE AND HALF-POWER BANDWIDTH FREQUENCIES TO CALCULATE QUALITY FACTOR(S) FOR THE ANTENNA GEOMETRY SHOWN IN FIG. 3.6 AND TABLE 4. ....35

TABLE 6. FAR-FIELD RELATIVE POWER PERCENTAGES $TM_{MN}$ -$TE_{MN}$ DATA FOR SQUARE MICROSTRIP PATCH ANTENNA MOUNTED ON A FINITE GROUND PLANE (SEE FIG. 3.6). ....36

TABLE 7. DIMENSIONS (IN CM) OF THE SHORT MONOPOLE (SHOWN IN FIG. 4.1) INTEGRATED TO A HANDHELD DEVICE. ....39

TABLE 8. $TM_{MN}$ MODE COMPOSITIONS FOR CENTER AND EDGE-MOUNTED MONOPOLES SHOWN IN FIG. 4.2. ....41

TABLE 9. DIMENSIONS (IN CM) OF THE CONVENTIONAL PIFA GEOMETRY SHOWN IN FIG. 4.4 ....42

TABLE 10. RESONANCE AND HALF-POWER BANDWIDTH TABULATED VALUES FOR THE PIFA SHOWN IN FIG. 4.4. ....43

TABLE 11. CALCULATED FAR-FIELD *TM* AND *TE* MODE COMPOSITIONS FOR CONVENTIONAL PIFA SHOWN IN FIG. 4.4. ....44

TABLE 12. RESONANCE AND HALF-POWER BANDWIDTH TABULATED VALUES FOR THE PIFA INTEGRATED TO THE HANDHELD DEVICE SHOWN (SEE FIG. 4.7). ....45

TABLE 13. FAR-FIELD *TM* AND *TE* MODE COMPOSITIONS FOR PIFA MOUNTED ON HANDHELD STRUCTURE. ....46

TABLE 14. RESONANCE AND HALF-POWER BANDWIDTH TABULATED VALUES FOR THE PIFA SHOWN IN FIG. 4.10 WITH $H=\lambda/35$ ....49

TABLE 15. QUALITY-FACTOR VERSUS HEIGHT FOR A LOSSLESS PIFA OVER AN INFINITE GROUND PLANE (SEE FIG. 4.10). ....52

TABLE 16. FAR-FIELD *TM* AND *TE* MODE COMPOSITIONS FOR MINIMUM HEIGHT PIFA MOUNTED ON THE HANDHELD DEVICE (SEE FIG. 4.15). ....54

TABLE 17. DIMENSIONS FOR CONVENTIONAL PIFA WITH CAPACITIVE-LOAD AND MEANDERING FOR MINIATURIZATION SHOWN IN FIG. 4.19. ....58

TABLE 18. CALCULATED IMPEDANCE AND QUALITY FACTOR VALUES FOR THE FOUR MINIATURIZATION CONFIGURATIONS BASED UPON THE MODEL SHOWN IN FIG. 4.19. ....58

TABLE 19. DIMENSIONS OF THE ACTIVE, SWITCH-TUNED PIFA MODEL WITH CAPACITIVE- LOADING SHOWN IN FIG. 4.22. ....61

TABLE 20. DIMENSIONS OF THE STUART-BEST DOUBLE RESONANT SPIRAL ANTENNA GEOMETRY SHOWN IN FIG. 5.1. ....69

TABLE 21. FAR-FIELD *TM* AND *TE* MODE COMPOSITIONS FOR MULTI-RESONANT SPIRAL ANTENNA. ....71

TABLE 22. DIMENSIONS OF THE CADFEKO GEOMETRY OF THE RAVIPATI ANTENNA SHOWN IN FIG. 5.6. ....73

TABLE 23. FAR-FIELD *TM* AND *TE* MODE COMPOSITIONS FOR RAVIPATI WB ANTENNA AT *F=1.0 GHZ*. ....74

TABLE 24. DIMENSIONS FOR THE AIR-BACKED WC J-POLE ANTENNA SHOWN IN FIG. 5.13 ....79

TABLE 25. FAR-FIELD *TM* AND *TE* MODE COMPOSITIONS FOR WIDEBAND COMPACT J-POLE ANTENNA AT *F=1.0 GHZ*. ....80

TABLE 26. DIMENSIONS FOR THE WIDEBAND-COMPACT J-POLE ANTENNA MOUNTED ON HANDHELD FIXTURE SHOWN IN FIG. 5.16. ....82
TABLE 27. FAR-FIELD *TM* AND *TE* MODE COMPOSITIONS FOR WIDEBAND COMPACT J-POLE ANTENNA MOUNTED ON HANDHELD FIXTURE, $f_o = 1.0$ *GHz* (SEE FIG. 5.16). ....83
TABLE 28. DIMENSIONS FOR THE AIR-BACKED U-SLOT ANTENNA SHOWN IN FIG. 5.19.. ....85
TABLE 29. FAR-FIELD *TM* AND *TE* MODE COMPOSITIONS FOR U-SLOT WIDE-BAND ANTENNA AT $f$=*1.0* GHZ. ....88
TABLE 30. CLASS-F AND INVERSE CLASS-F AMPLIFIER HARMONIC TERMINATIONS ....93
TABLE31. DIMENSIONS FOR THE PIFA MODEL (SHOWN IN FIG. 6.1) DESIGNED FOR DIRECT INTEGRATION TO AN INVERSE CLASS-F AMPLIFIER. ....94
TABLE 32. DIMENSIONS FOR THE MODEL GEOMETRY OF THE MULTI-RESONANT PIFA SHOWN IN FIG. 7.1. ....103
TABLE 33. FAR-FIELD *TM* AND *TE* MODE COMPOSITIONS FOR THE MULTI-RESONANT PIFA MOUNTED ON A HANDHELD CHASSIS (SEE FIG. 7.7) ....111

# 1 CHAPTER - Introduction

Resonance of mechanical and structural systems is a physical phenomenon engineers in the mechanical and civil engineering disciplines traditionally avoid. The design of acoustic instruments is a specialized exception. Electrical engineering is distinguished from classical engineering disciplines by a design philosophy that consistently targets resonance.

Radiation of a continuous wave through free space is a form of resonance where the far-field wave energy oscillates between electric and magnetic fields transverse to the direction of propagation. Passive antennas are reciprocal devices that, convert a guided wave to free space radiation. Similar to instrumentation sensors, antennas are transducers connected to electronic systems for signal detection, amplification and processing. Recognition of the physical antenna as a transducer bound by the size of the free-space wavelength may have influenced Harold Wheeler's observation, 'antennas and propagation will always retain their identity, being immune to miniaturization and digitization' [1].

Limitations to miniaturization may exist, however multiple classes of antennas have evolved to address engineering challenges since the early experiments of Hertz. Antennas are typically categorized into one of three categories by their electrical size relative to the free-space wavelength. The relatively narrow region of resonant antennas divides the two broader classes of electrically-large and electrically-small antennas.

The physical dimension of a resonant antenna is on the order of the free space wavelength, $\lambda$. Highly-directive, traveling-wave, and broadband antennas are electrically-large with physical dimensions that are multiple free-space wavelengths. Electrically-small antennas are characterized by constant, low-valued directivity and physical dimensions $L_{ANT}$ that are a fraction of the free-space wavelength of the radiated fields.

Historically, small antennas have been a constant presence in antenna research and development. Beginning with the first commercial amplitude modulation radio systems of the 1920’s, antenna engineers were challenged by the RF performance limitations of physically-large radio towers mounted over lossy ground planes, carefully stabilized with combinations of insulated and loaded guy-wires [2]. During the decades preceding World War II, antenna

engineering was focused on increasing efficiency and maintaining bandwidth while reducing height and coupling loss.

World War II was a highly productive period for European, American, and Japanese research in HF, VHF, and UHF technologies[11]. Radar and electronic warfare systems are two examples of the technological advances during World War II [3]. Soon after the peace, scientists and engineers returned to the open research community with appreciable insight and understanding to share with colleagues. Harold Wheeler and L.J. Chu, two pioneers of small antenna research, both made significant contributions to the war effort and the research community in the years afterwards.

Dr. Wheeler's broad observation regarding antennas retaining their identity may ultimately be accurate, however the explosion of handheld and portable devices has created an environment to test the limits of antenna miniaturization and integration. Current research on small-antenna systems is focused on active, reconfigurable structures, broadband reception, and improved efficiency. Electrically-small, tunable or wideband antennas are integrated in or on similarly-sized packaging.

The objective of the dissertation is to develop techniques for the analysis of ground plane coupling and interaction of electrically-small device platforms with integrated antenna elements. Modal analysis, both in the far-field and near-field is proposed as a method to gain insight to the nature of small-antennas, coupling and the interaction with portable-device packaging. A focus of the research presented in the dissertation is to address small-antennas near the upper limit defined by Wheeler. Several antennas in the range of $0.5<ka<1.0$ are self-resonant and have attractive wideband impedance response characteristics. Fundamental limit theory for electrically-small antennas better approximates performance for antennas in the range $ka<<0.5$.

## 1.1 Overview of Dissertation

This dissertation is organized into four parts. Chapter 2 includes a historical review and survey of previous work to provide background information. Previous work investigating impedance and

[1] HF - High Frequency (3-30 MHz), VHF - Very High Frequency (30-300 MHz)
UHF - Ultra High-Frequency (300-3000 MHz)

bandwidth sensitivity to finite ground plane dimensions is revisited. Popular classes of low-profile and narrow and wide bandwidth electrically-small antennas are introduced.

Chapter 3 outlines the approach and methods chosen for the analysis. An important relation between antenna quality factor and matched-load fractional bandwidth is discussed. Spherical Mode Decomposition algorithms for far-field and near-field calculations are reviewed and implemented in computer algorithms. A canonical low-profile, probe-fed microstrip patch antenna on a finite ground plane is presented as an example to demonstrate the nature and variation in antenna/ground-plane coupling.

The second part of the dissertation, contained in Chapters 4 and 5, presents similar analyses for several classes of interesting small antennas. Chapter 4 investigates narrowband antennas. The Planar Inverted-F Antenna (PIFA) as a narrowband single-resonant structure is subjected a height reduction study in addition to several miniaturization techniques. A reconfigurable, switch-tuned model is also introduced.

Chapter 5 is similar to Chapter 4 with multi-resonant, wideband small antennas chosen for investigation. Different variations of volumetric, in addition to low-profile, double-tuned antennas are studied to quantify their ground plane coupling characteristics.

Chapter 6 investigates hardware integration in small antenna devices. An example illustrating the harmonic design of a PIFA antenna element as a load resistance for an Inverse Class-F power amplifier is presented. The emphasis is not on the amplifier, but rather the tuning feature. An evaluation of current hardware technologies and their applications to active antenna elements is also included.

Chapter 7 introduces a passive, low-profile multi-resonant antenna element with monopole-class omnidirectional radiation. The antenna is well-suited for handheld, portable commercial applications and could be modified for integration with high-efficiency power amplifiers with harmonic tuning.

Conclusions and suggestions for future work provide the final focus.

## 1.2 References


[1] H.A. Wheeler, "Antenna Topics in My Experience ", IEEE Transactions on Antennas and Propagation, vol.AP-33, no. 2, February 1985, pp. 144-151.

[2] J. Wood, "AM Terrestrial Broadcasting, Past Present, and Future," IEE Review, vol. 35 March 1989, pp.89-91.

[3] Alfred Price, *The History of US Electronic Warfare*, vol. 1, The Association of Old Crows, pp. 1-7.

# 2 CHAPTER - Background

## 2.1 Introduction

Electrically-small antennas (ESAs) are distinguished from the broad category of radiating elements by physical dimensions $L_{ANT}$ that are fractions of the free-space wavelengths of the radiated fields. The broadest category of ESA includes any antenna that may be circumscribed by a radiansphere of radius $a$ as depicted in Fig. 2.1, related to the free-space wavenumber $k = 2\pi/\lambda$, such that $ka \le 1$ or $a = \lambda/2\pi$.

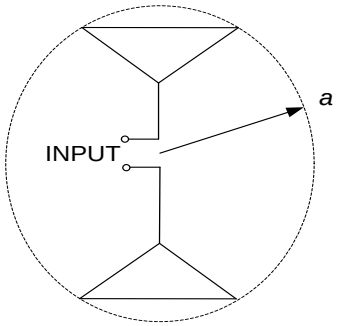


**Fig. 2.1. Schematic Diagram of a Vertically-Polarized Omnidirectional Antenna enclosed by a sphere radius $\rho$=$a$, centered about the origin.**

H.A. Wheeler's article [1] published shortly after World War II was the first to relate antenna size, bandwidth and efficiency. He modeled small dipole antennas (electric and magnetic) using discrete reactances (parallel capacitance and series inductance) in circuits with the far-field radiation resistance. His seminal paper published in 1947 is not only an elegant illustration of duality for electric and magnetic dipole parameters, but offered practical insight to the physical limitations of small antennas.

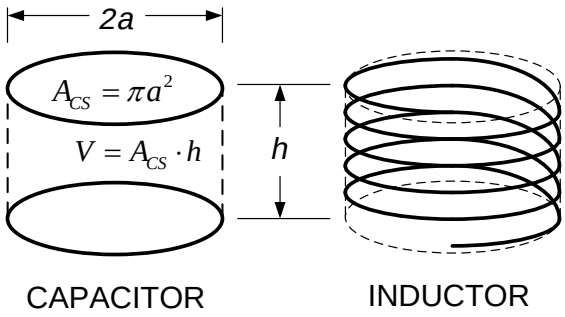


**Fig. 2.2**. **Capacitor and Inductor occupying equal cylindrical volumes.**

Wheeler related antenna height and cylindrical volume to a radiation power factor, a ratio of the antenna circuit real power to the reactive energy. Radiation power factor is the inverse of the quality factor. Inverting the power factor, $p = (ka)^3$, provides a very good approximation for the minimum $Q$ using field equation approaches [2].

Wheeler made several interesting observations regarding a height reduction for small antennas. Antenna efficiency may be stated in terms of the power radiated from the transmitting antenna and the available power from the receiving antenna to a load. Loading in a circuit, either coupling the source to a transmit antenna or the receive antenna to a load, limits the output power to a fraction of the available power and is defined as the coupling efficiency.

The current distribution of a resonant length dipole antenna element is nearly sinusoidal with maximum current at the center, and zero current at each end. As the physical length of the element is decreased, the current assumes a triangular distribution with the same boundary conditions. The resulting radiation pattern is omnidirectional in azimuth with a fixed directivity of 3/2. Once the current distribution is essentially triangular and the physical dimensions of the antenna element are reduced further, the far-field radiated power decreases with corresponding reductions in physical length or area of the transmitting antenna shown in (1). The resulting decrease in radiation resistance relative to the other resistance in either coupling circuit degrades coupling efficiency and is one of the principal limitations of small antennas [1].

$$R_{RAD} = \frac{P_{RAD}}{2|I_o|^2} \propto \left[ \frac{L_{DIPOLE}}{\lambda} \right]^2 \tag{1}$$

The results for $R_{RAD}$ and $Q$ in (1) and (2) respectively, indicate the equivalent circuit quality factor is a function of height ($h$) and cylindrical volume ($V_{CYL}=A_{CS}\cdot h$) as shown in Fig. 2.2. The radiation resistance is only function of electrical height. Wheeler found these quantities to be,

$$Q = 6\pi \left[ \frac{\left(\lambda/2\pi\right)^3}{A_{CS} h} \right]_{k_a=1} \tag{2}$$

$$R_{RAD} \propto \left( \frac{h}{\lambda} \right)^2 \tag{3}$$

Soon after Wheeler's work, L.J. Chu [4] derived a minimum quality factor based on an expansion of the fields in terms of spherical modes. For the ideal case of a lossless antenna, the antenna quality factor $Q_A$, is defined by the ratio of stored energy to radiated power at a particular frequency to give

$$Q_A = \omega \frac{W}{P_{RAD}}, \; where \; W = 2\max\left(W_m, W_e\right). \tag{4}$$

The calculation of $Q_A$ is not straightforward because the total time-average stored energy outside the sphere is infinite. A series of papers have investigated different approaches to separate the non-propagating energy from the total energy [5, 6, 7]. The approaches are valid in concept, but difficult to implement in practice.

Wheeler modeled the small antenna as a single-pole, series RL or shunt RC circuit. Chu modeled equivalent circuits for $TE_{MN}$ or $TM_{MN}$ spherical mode radiation. Collin, Rothchild [5], and McLean [6] subtracted the energy associated with the far-field radiation to determine a $Q_A$ for each mode. However, for all approaches, an expression for the lowest order spherical mode found by all is given as

$$Q_A = \left. \frac{1}{\left(ka\right)^3} \right|_{ka<<1}. \tag{5}$$

If the antenna is not sufficiently small, additional modes are required to represent the radiated power and the lowest order approximation shown in (5) is misleading.

Yaghjian and Best [7] established an approximate relation between $\left|\partial Z/\partial\omega\right|$ at resonance to fractional bandwidth and $Q_A$ [7]. For the case of half-power fractional bandwidth for a matched

input, the relation to $Q_A$ simplifies. Yaghjian's approach to tie fractional bandwidth to antenna quality factor will be discussed in Chapter 3.

## 2.2 Finite Ground Plane Detuning

The oscillatory behavior of the antenna impedance as a function of ground plane diameter has been well understood for resonant antennas (e.g. quarter-wave monopoles) mounted on large circular ground planes. Published results for analytical investigations and measurement campaigns are readily available [8, 9, 10].

The Cartesian form of the universal curve shown in Fig. 2.3 (b) is interesting and worth considering if small antennas on small ground planes demonstrate the same behavior. A preliminary step was completed with a quarter-wave monopole mounted on a large ground plane to validate the simulation approach. The size of the ground plane was reduced to $1<D_{GP}/\lambda<10$. Simulated results shown in Fig. 2.3 (a) and (b) clearly show the oscillatory characteristic of the complex impedance versus the diameter of the ground plane.

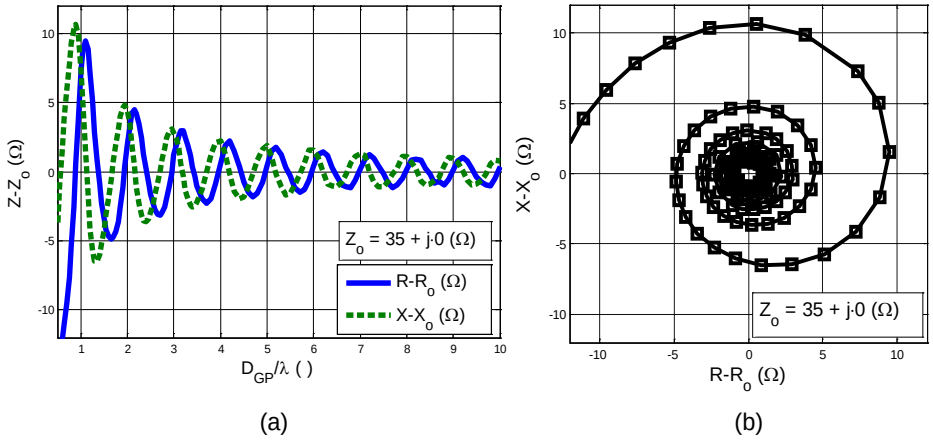


**Fig. 2.3. Complex Impedance versus Diameter of Ground Plane for *1<D/λ<10* for a *λ/4* monopole. Impedance values shown were calculated using FEKO with a reference impedance of a monopole model on an infinite ground plane, $Z_O=35+j0$.**

The sensitivity of a disk-loaded monopole (*ka=0.5*) attached to a comparable ground plane was considered. Fig. 2.4 is an illustration of the antenna geometry. Table 1 lists the corresponding dimensions of the disk-loaded monopole model. The circular ground plane was

varied for values of $R_{MIN}=a$ to $R_{MAX}=8a$, where $R_{GP}=a$ is equivalent to the circumscribing radius of the disk-loaded monopole.

Fig. 2.5 (a) and (b) are plots of the Return Loss response and Fractional Bandwidth versus Radius of Ground Plane, $1<R_{GP}/a<10$. The Return Loss response curves indicate the dimension of the ground plane does not significantly influence the resonant frequency of the disk-loaded monopole for values of $R>2a=\lambda/2\pi$. For each finite ground plane geometry, a detuning ratio, $\Delta f / f_R$ is defined as the fractional change in tuned frequency with respect to the infinite ground plane tuned frequency. Fig. 2.5 (b) shows a detuning ratio $\Delta f / f_R$ with the impedance bandwidth (VSWR<2:1) bands as a function of the normalized ground plane radius, $R_{GP}/a$. The plot indicates detuning becomes negligible for $R_{GP}>2a$ with improving impedance bandwidth as $R_{GP}$ increases.

From the results shown in Fig. 2.5 the detuning ratio of less than five percent occurs for a ground plane dimension of $R_{GP}>2a$. If a lower threshold or minimum ground plane dimension of $R_{GP}>2a$ is chosen to bound the detuning ratio,

$$ka = 0.5 \rightarrow a = \frac{\lambda}{2\pi} \cdot \frac{1}{2} = \frac{\lambda}{4\pi} \tag{6}$$

The minimum dimension of the ground plane

$$R_{GP} \geq 2 \cdot \frac{\lambda}{4\pi} = \frac{\lambda}{2\pi} \tag{7}$$

The minimum radius shown corresponds to a minimum diameter $D_{MIN} \geq 0.3\lambda$ which is in the vicinity of square ground-plane dimension greater than $0.2\lambda$ observed for a similar investigation of another small monopole-class antenna [12].

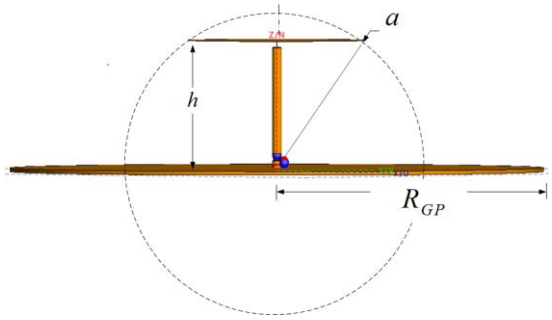


**Fig. 2.4. CADFEKO rendering of disk-loaded monopole.**

| $f$ [MHz] | $\lambda$ [cm] | $ka$ [ ] | $a$ [cm] | $h$ [cm] | $R_{GP}$ [cm] |
|---|---|---|---|---|---|
| 900 | 33.3 | 0.5 | 2.72 | 2.35 | 4.08 |

**Table 1. Dimensions of the *ka=0.5* disk-loaded monopole shown in Fig. 2.4 $R_{GP}$=1.5a.**

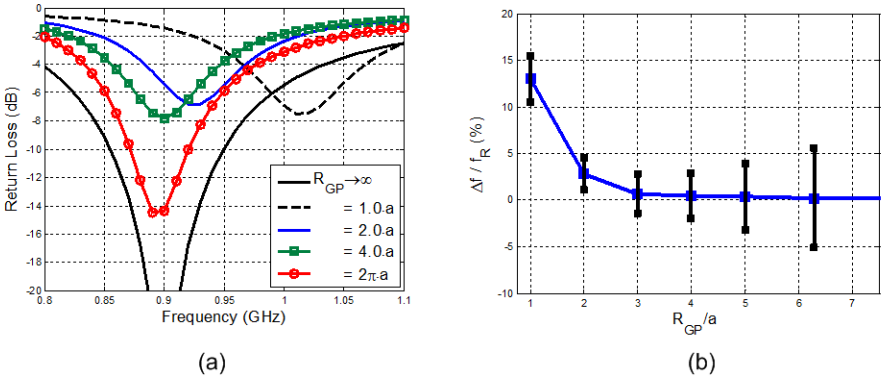


**Fig. 2.5. Return Loss (a) and fractional detuning (b) versus radius of ground plane. Impedance calculations were made using FEKO. The error bars indicate the impedance bandwidth at the detuned center frequency**

Disk-loaded monopoles are used to reduce height and are low-profile, but require external matching to achieve an impedance match. A low-profile, self-resonant monopole-class antenna is the planar inverted-F antenna (PIFA), where the placement of the feed acts as a Gamma match to tune the antenna. The PIFA is discussed in the next section.

## 2.3 Low Profile Antenna Solutions - Small versus Low-Profile

Consumers enjoy properly functioning antennas on-board their personal communication devices, but unfortunately they have never learned to appreciate the intrinsic beauty of antennas. Urban cell phone antenna towers are often concealed from pedestrian view, and every effort has been made to reduce the form factor of handheld terminal antennas. As a result, low-profile, small, and inefficient antennas are market-driven solutions for consumer-oriented specifications in many portable designs.

Two classes of low-profile antennas, the planar inverted-F antenna and the microstrip antenna are used for a majority of handheld wireless devices. An emerging third class of

antennas acts as a source to excite the entire handset structure with a small antenna element. An example is presented in Chapter 5.

Planar inverted-F antennas (PIFAs) are popular due to their physical size requirement in cellular communication frequency bands. PIFAs are compact and maintain a radiation pattern that is predominately omnidirectional in azimuth. Microstrip patch antennas are characterized by radiation normal to the planar surface and are well-suited for satellite communication devices.

### 2.3.1 Planar Inverted-F Antenna

The Planar Inverted-F Antenna (PIFA) is a bandwidth enhancing extension of the wire-based Inverted-F antenna (IFA) used in aviation. The IFA may be considered as a transmission line loaded monopole with a gamma match at the feed. As shown in Fig. 2.6, offsetting the feed from the structural connection point introduces loop inductance to improve tuning capability.

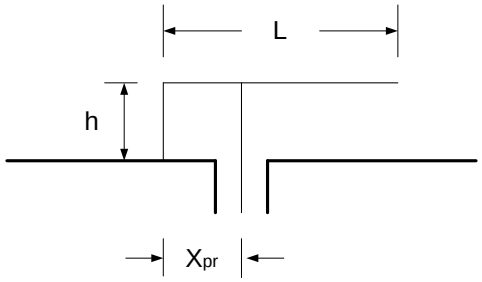


**Fig. 2.6. Inverted-F Antenna formed from a bent monopole with offset feed. The inductance loop loads the antenna at the input to improve impedance matching.**

The PIFA is a self-resonant top-loaded monopole class radiating structure with some tuning control achieved by varying the position of the probe-feed in relation to the shorting bar/strap and the free-end. PIFAs require a ground plane and the geometry of the antenna location with respect to the ground plane determines the nature of the coupling of the antenna currents to the ground plane surface currents.

A thorough parametric study of ground plane effects on PIFA antenna performance was completed by Huynh and Stutzman [12]. As a starting point for this effort, the square PIFA and ground-planes used in [12] were scaled to $f = 1.0$ *GHz* to establish a benchmark for additional narrowband and wideband antenna models. Fig. 2.7 is an engineering perspective of the PIFA geometry with a square conducting plate and ground plane. The dimensions for model of a

conventional PIFA are presented in Table 2. Fig. 2.8 illustrates the single-resonant impedance characteristics of the conventional PIFA shown. Fig. 2.9 (a) and (b) are three-dimension renderings of $E_\theta$ and $E_\Phi$ radiation patterns for conventional PIFA. The $E_\theta$ is principally omnidirectional.

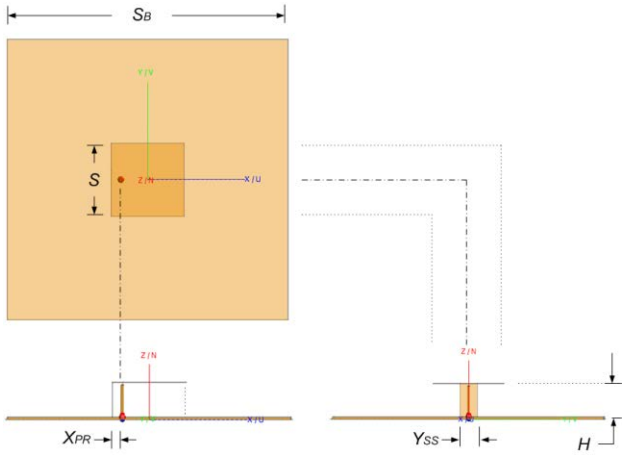


**Fig. 2.7. CADFEKO rendering of a conventional PIFA scaled to *f=1.0 GHz.***

| $S_B$ [cm] | $S$ [cm] | $H$ [cm] | $X_{PR}$ [mm] | $Y_{SS}$ [cm] |
|---|---|---|---|---|
| 15.0 | 3.92 | 1.86 | 5.4 | 0.98 |

**Table 2. Dimensions of the conventional PIFA shown in Fig. 2.7.**

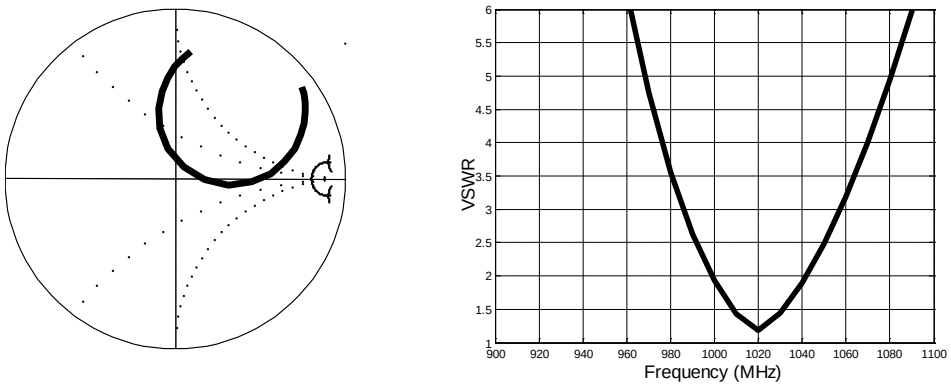


**Fig. 2.8. Smith chart (a) and computed VSWR (b) of the conventional PIFA shown in Fig. 2.7. Impedance response calculations were obtained using FEKO.**

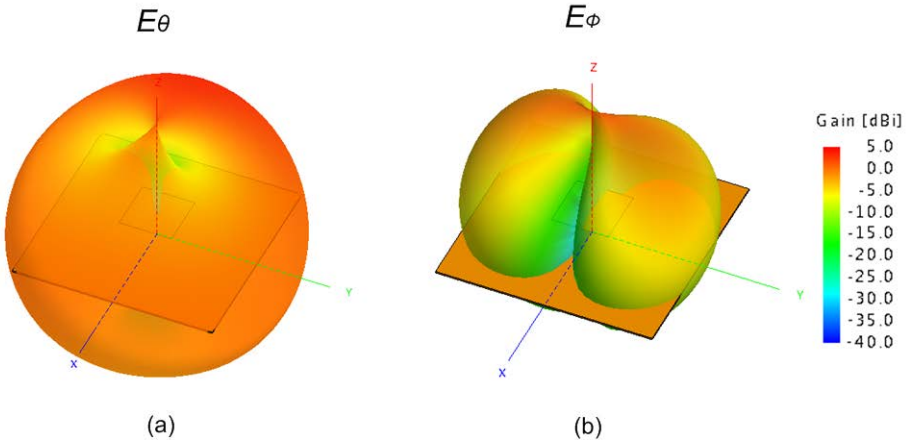


**Fig. 2.9. $E_\theta$ and $E_\phi$ radiation patterns computed using FEKO for the conventional PIFA shown in Fig. 2.7.**

The low-profile self-resonant properties of the PIFA antenna are optimal for wireless applications. In terms of form factor, the PIFA is ideal for integration into a top corner of the handheld device structure. The radiation patterns are predominately omnidirectional. However, the single-resonant nature of the conventional PIFA element is limited in terms of fractional bandwidth (VSWR<2:1) to less than ten percent for practical electrical heights shorter than λ/20.

### 2.3.2 Microstrip Antenna

The microstrip patch antenna is another example of a low-profile resonant antenna that is also band limited. A microstrip antenna (MSA) is a resonant device comprised of a dielectric

substrate between and upper conductor and ground plane. Microstrip antennas are low-profile, conformable, and easily manufactured. The resonant microstrip antenna has a frequency dependent surface current distribution that is typically excited with a microstrip feed line or coaxial probe.

The largest dimension for a resonant microstrip antenna is found from,

$$L_{MSA} \approx \frac{\lambda_R}{2} = \frac{1}{2} \cdot \frac{\lambda_o}{\sqrt{\varepsilon_R}} \tag{9}$$

where $\varepsilon_R$ is the relative permittivity of the dielectric substrate. Physical size limitations typically restrict MSA applications to frequencies above *f=1 GHz* [13]. High dielectric materials may be considered for miniaturization, but the unfortunate penalty is an additional reduction in bandwidth.

A number of methods have been developed to model the radiation characteristics of the microstrip antenna. The transmission line model treats the radiating edges as a pair of transmission lines $180^o$ out of phase. The model neglects feed effects and field variations along the radiating edges. An even more intuitive perspective is to consider the fringing currents as two radiating slots separated by the width of the microstrip patch. Two similar slots in-phase, approximately $\lambda_R/2$ apart, will generate peak radiation amplitude normal to the plane of the microstrip.

Fig. 2.10 is an engineering perspective of a probe-fed, square, microstrip patch antenna model created for the analysis described in Chapter 3. The substrate is modeled as a volume of lossless media with a relative permittivity of $\varepsilon_R=1.05$. Dimensions and material properties for the microstrip antenna are presented in Table 3. Dimensions and material properties for the square microstrip patch antenna (see Fig. 2.10).

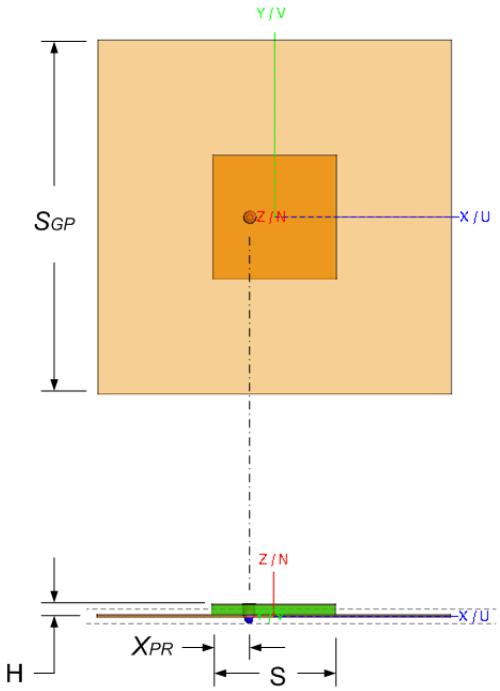


**Fig. 2.10. CADFEKO rendering of a probe-fed, square microstrip patch antenna mounted on a finite ground plane, $S \approx \lambda$. A lossless low-valued dielectric has been chosen to maximize bandwidth.**

| $S_{GP}$ [cm] | $S$ [cm] | $H$ [cm] | $X_{PR}$ [cm] | $\varepsilon_R$ [ ] | $tan\delta$ [ ] |
|---|---|---|---|---|---|
| 32 | 12.5 | 1.0 | 3.74 | 1.05 | 0.0001 |

**Table 3. Dimensions and material properties for the square microstrip patch antenna (see Fig. 2.10).**

Fig. 2.11 shows the parallel resonance complex impedance response (a), and the corresponding VSWR with a reference impedance of $R_o$=50 Ω. The 2:1 VSWR bandwidth determined primarily from the height is approximately 4 %. The $E_\theta$ and $E_\phi$ radiation patterns for the microstrip antenna on a square ground plane are shown in Fig. 2.12. The $E_\theta$ and $E_\phi$ patterns are comparable in magnitude which indicates comparable percent powers in the *TM* and *TE* mode decompositions. The resulting patterns are not omnidirectional in azimuth, nor representative of monopole-class radiation.

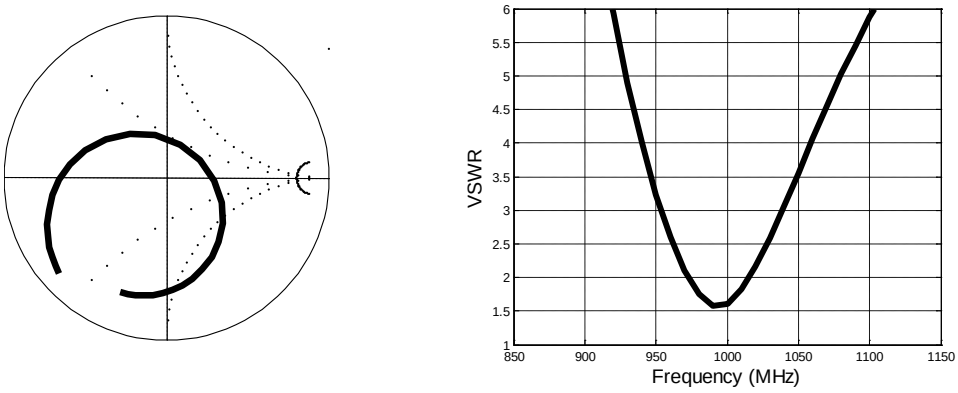


**Fig. 2.11. Complex Impedance Response of Square Microstrip Patch Antenna (shown in Fig. 2.10) mounted on a finite ground plane, $S \approx \lambda$. Impedance calculations were obtained using FEKO.**

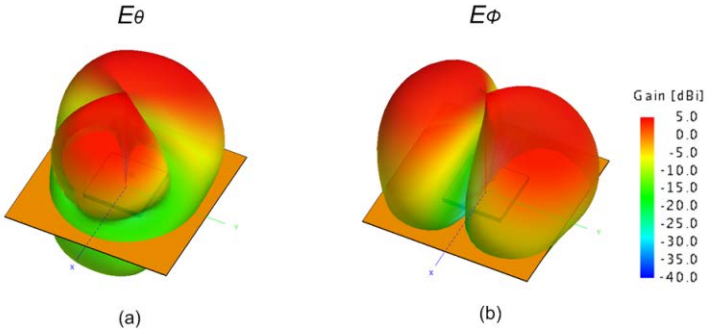


**Fig. 2.12. $E_\theta$ and $E_\phi$ radiation patterns ($f$=1.0 GHz) calculated using FEKO for the square microstrip patch antenna (shown in Fig. 2.10) mounted on a finite ground plane, $S \approx \lambda$.**

Microstrip antennas are used in a variety of interesting applications. For example, single element MSAs are utilized for GPS satellite reception with a low-noise amplifier and front-end circuitry integrated immediately behind the antenna probe feed. Multiple element planar arrays are configured for avionic conformal surfaces. Current engineering research focuses on robotic spray applications of conductive paints and dielectrics to utilize physical surface areas on carbon fiber unmanned autonomous vehicles (UAVs) and aircraft. In this arrangement, a single-probe through the wall of a carbon-fiber structure feeds a microstrip feed manifold that may be applied with robotic spray applique procedures [14].

The single-probe-to-microstrip-feed array manifold concept has great appeal to lightweight UAV systems, however line tolerances for spray application methods present challenges in

actual fabrication for radar apertures. An additional technical concern is to separate and accurately estimate the feed manifold and array efficiencies. Stutzman described a design tradeoff for microstrip array feed manifolds where the challenge is to create loosely bound radiating fields at the antenna element(s), while maintaining tightly bound guided-wave fields along the microstrip feed line [13].

The planar inverted-F antenna and the microstrip antenna are practical solutions for low-profile and portable device applications. The PIFA generates a radiation pattern that is typically omnidirectional in azimuth. The microstrip antenna is more of a low-profile structure than 'electrically-small'. The microstrip antenna generates a radiation pattern normal to the planar surface of the element. Both antennas are bandwidth-limited. Conventional heights chosen for the PIFA and microstrip antenna classes restrict the 2:1 VSWR bandwidths to less typically less than ten and five percent respectively.

## 2.4 Active Reconfigurable Narrowband Structures

Advances in microelectronics have led to increasing speed and computing power in addition to reductions in form factors. Bandwidth and efficiency specifications have challenged small antenna design and radio engineers for generations. The current market desires high data rate wireless links requiring instantaneous bandwidths greater than five percent and that are entirely portable.

The system design must strike a balance between consumer demand and physical limits. One larger and simpler solution to increase bandwidth would utilize passive, wide bandwidth 'small' antennas with sufficient instantaneous bandwidth to operate over a detuning range.

Another solution is to integrate active-circuitry in a smaller, narrowband device and utilize frequency-agility to maintain efficient operation over the detuning band. There is interest in and applications for a small, handheld or highly portable device with a relatively narrow instantaneous bandwidth that may operate across a larger overall bandwidth.

The advantage is the potential viability of a very low-profile communication device utilizing active controls to compensate for variations in the near-field. For example, a relatively narrow system bandwidth ($B_{SYS} \approx 5\%$) could theoretically be sustained by an antenna circumscribed by a sphere radius, $a_{MIN}$. Fig. 2.13 is an illustration of the circumscribing sphere for a narrow-band

antenna communication system. The antenna bandwidth for a matched-load case would be half the system bandwidth.

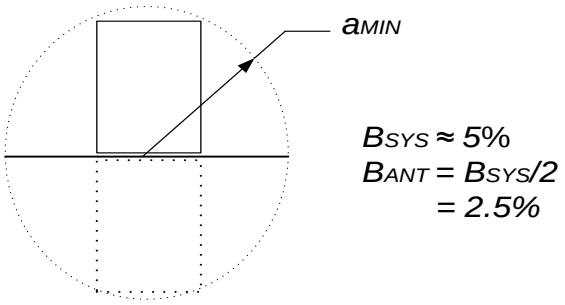


**Fig. 2.13. Illustration of minimum antenna dimension for nominal system bandwidth. The hypothetical antenna is mounted on a finite ground plane large enough the image currents may be included in the circumscribing sphere, radius $a_{MIN}$. The antenna impedance bandwidth for the case of the matched-source impedance is one-half the system impedance.**

Harrington's approximation relating bandwidth and geometry may be used to solve for the electrical size of the smallest radiating element.

$$B_{ANT} \approx \left(ka_{MIN}\right)^3 \tag{10}$$

Rearranging and substituting, $k = 2\pi/\lambda$

$$a_{MIN} = \frac{\sqrt[3]{B_{ANT}}}{\left(2\pi/\lambda\right)} \tag{11}$$

The smallest antenna dimension in units of free-space wavelength

$$\frac{a_{MIN}}{\lambda} = \frac{\sqrt[3]{B_{ANT}}}{2\pi} \approx \frac{1}{20} \tag{12}$$

The approximate electrical size of the antenna corresponds to

$$a_{MIN} \approx \frac{\lambda}{20} \quad \rightarrow \quad ka_{MIN} \approx \frac{\pi}{10} = 0.31 \tag{13}$$

Low-profile antennas are not volume-efficient and hardly approach the fundamental limits. However, bandwidths on the order of five percent from a radiating element with a maximum height of approximately $h_{MAX} \approx \lambda/20$ are practical design specifications in current research and commercial environments.

## 2.5 Wideband Electrically-Small Antennas

Active-controlled reconfigurable antennas have great appeal in current research, however, passive electrically-small antennas designed for an additional margin of bandwidth are attractive and more reliable alternatives. The devices are simpler in form and the antenna remains a transducer in its purest definition.

Traditional impedance matching for the AM transmitter and the amateur radio bands is achieved with tunable discrete reactive elements. Current small antenna designs for center frequencies in the range of $f = 1.0\ GHz$ use an approach that may be simpler in concept, but require a designer's insight and understanding to successfully implement. Instead of adding matching or tuning elements external to the antenna, frequency-dependent reactances are integrated directly within the antenna structure. The addition of double-tuning elements within the antenna radiansphere increases frequency-dependent current paths and improves the overall impedance bandwidth.

Fig. 2.14 is an example of a wideband electrically-small antenna with three double tuning structures. The initial antenna element is the disk-loaded cone. Two tuning bars provide low-frequency double-tuning. The partial resonant cylinder interacts with both the shorting bars and the disk-loaded cone. Fig. 2.15 illustrates the VSWR responses for the three wide bandwidth structures utilized in the example.

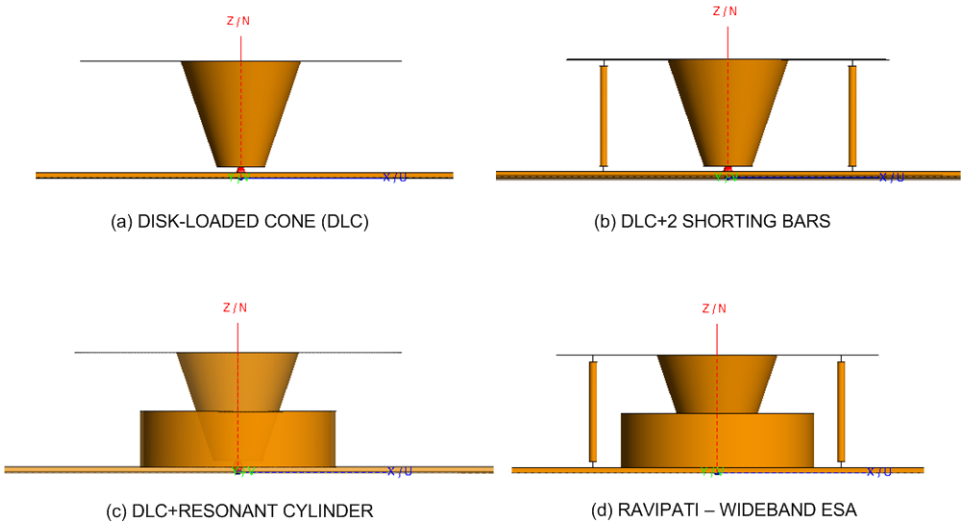


**Fig. 2.14. CADFEKO rendering of Ravipati wideband ESA with three double-tuning structures. The initial antenna element (a) is the disk-loaded cone (DLC). Two tuning bars provide Low-frequency double-tuning (DLC+2 SB). The resonant cylinder interacts with both the shorting bars and the disk-loaded cone.**

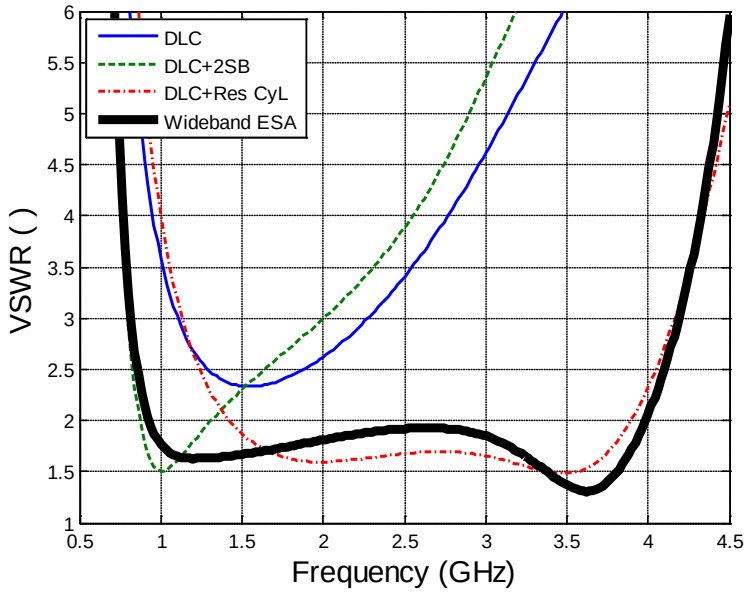


**Fig. 2.15. VSWR Responses illustrating the Wideband ESA antenna design. The impedance responses were calculated using FEKO for the four antenna geometries. The initial antenna element (a) is the disk-loaded cone (DLC). Two tuning bars provide Low-frequency double-tuning (DLC+2 SB). The resonant cylinder interacts with both the shorting bars and the disk-loaded cone.**

## 2.6 Summary

The chapter reviewed historical background in small antenna theory, and demonstrated an example of near-field detuning and bandwidth degradation for a small disk-loaded monopole on a small circular ground plane. The planar inverted-F antenna and the microstrip antenna were introduced and discussed in a small antenna context. Active control to create a reconfigurable antenna structure was discussed as one method to acquire sufficient instantaneous bandwidth. Electrically-small wideband antennas were also introduced as a potential passive solution to the enhancement of bandwidth for near-field detuning.

Chapter 3 will continue the small antenna theory and introduce the bandwidth-quality factor relationship used with several other approaches to estimate fractional bandwidth. Spherical mode decomposition will also be another tool to gain additional insight on small antenna performance enhancement.

## 2.7 References


[ 1] H.A. Wheeler, "Fundamental Limits of Small Antennas," *Proc. IRE*, vol. 35, Dec. 1947, pp. 1479-1484.

[ 2] D.F. Sievenpiper et al., "Experimental Validation of Performance Limits and Design Guidelines for Small Antennas," IEEE Transactions on Antennas and Propagation, vol. 60, no.1, January 2012, pp. 8-19.

[ 3] H.A. Wheeler, "The Radiansphere Around a Small Antenna," Proc. IRE, vol. 47, 1959, pp. 1325-1331.

[ 4] L.J. Chu, "Physical Limitations of Omni-Directional Antennas," Journal of Applied Physics, vol.19, Dec. 1948, pp. 1163-1175.

[ 5] R. Collin and S. Rothschild, "Evaluation of Antenna Q," IEEE Transactions on Antennas and Propagation, vol. 12, 1964, pp. 23-27.

[ 6] J.S. McLean, "A Re-Examination of the Fundamental Limits on the Radiation Q of Electrically-Small Antennas," IEEE Transactions on Antennas and Propagation, vol. 44, no. 5, May 1996, pp. 672-676.

[ 8] A.D. Yaghjian, S.R. Best, "Impedance, Bandwidth, and Q of Antennas," IEEE Transactions on Antennas and Propagation, vol. 53, no. 4, April 2005, pp.1298-1324.

[ 9] Henry Jasik, *Antenna Engineering Handbook*, McGraw-Hill, 1961, pp. 3-23

[10] J.E. Storer, "The Impedance of an Antenna over a Large Circular Screen," Journal of Applied Physics, vol. 12, August 1951, pp. 1058.

[11] M.M. Weiner, 'Monopole Element at the Center of a Circular Ground Plane Whose Radius is Small or Comparable to Wavelength," IEEE Transactions on Antennas and Propagation, vol.35, no.5, May 1987, pp. 488-495.

[12] M.C. Huynh, W.L. Stutzman, "Ground Plane Effects on Planar-Inverted-F Antenna (PIFA) Performance," IEE Proceedings on Microwave Antennas and Propagation, vol. 150, No. 4, August 2003, pp. 209-213.

[13] W.L. Stutzman, G.A. Thiele, *Antenna Theory and Design*, 2nd ed. pp. 210-218

[14] Applied EM, Inc. – correspondence with Mr. T. G. Campbell

# 3 CHAPTER - Approach/Tools

## 3.1 Introduction

Since Wheeler and Chu first described the inherent limitations of electrically-small antennas, several researchers have dedicated entire careers to the physics of inducing radiation from inefficient, non-resonant structures. The interaction or coupling of a finite ground plane or feed to an electrically-small antenna is a complex problem that is difficult to isolate from the small antenna. Steve Best has made numerous contributions to small antenna research since his early collaboration with Yaghjian mentioned in the previous chapter.

Best describes the unknown nature of and the difficulty in characterizing the antenna/ground plane interaction [1]. It may be intuitive to accept surface currents from a small ground plane contribute to the total radiation, but a quantitative characterization is not straightforward. In addition to the example shown in the Chapter 2, previous studies of monopole-class antennas over finite ground planes have investigated detuning, impedance response, radiation patterns and their sensitivity to changes ground plane size and antenna location [2-4].

Best also made an interesting qualitative comment that different classes of antennas couple differently to the ground plane. His observation indicates the assumption of single-mode radiation small antennas may not apply for all cases of small, monopole-class structures mounted on finite ground planes. Other classes of small low-profile antennas are designed to utilize the ground-plane as part of the radiating structure [5, 6].

The distinction between antenna and the fixture (finite ground plane or handheld chassis) is often blurred. How much radiation is from the antenna or the fixture? Investigation of the modal content may provide clues. Sievenpiper observed that often the electrical size of the antenna is not measured properly for 'feeder' antennas that excite a radiation mode in the structure [5]. Another point to consider is the reality that many self-resonant antennas are not 'small' in the strictest ($ka \leq 0.5$) sense and the single-mode approximation may not be valid. McLean observed that several very useful antennas fall into this range [7].

Rather than restrict the effort to a lower limit on electrical size (e.g. $ka \leq 0.5$), the following examples were chosen due to their popularity for wireless applications. An investigation of the

antenna classes in a quality factor and modal context would also be helpful to those in the antenna community who wish to apply theory to practical problems.

A number of self-resonant antenna designs are in the $0.5 \leq ka \leq 1$ range ideal for simulation and post-processing for modal content. Direct comparisons of different classes of antennas scaled to similar size and subjected to identical boundary conditions are presented in the following chapters. Simulation results from a compilation of antenna geometries will offer insight to the nature of antenna ground coupling in a spherical mode context.

Spherical mode decomposition of far-field radiation pattern data utilizing commercial method-of-moments software (FEKO) will be used in an example to quantitatively demonstrate the coupling of identical small, center-mounted monopoles over circular and square small ground planes.

A subsequent section will then compare the same far-field spherical mode decomposition to near-field mode decomposition. Comparisons of the modal components as a function of the radial distance to the field point are presented to validate the near-field algorithm. The tools developed in this section will be used with the addition of the antenna $Q$ approximation to investigate near-field variations and transitions in mode compositions from near- to far-field radiation regions. An example with a canonical microstrip antenna will conclude the chapter.

## 3.2 Analysis Tools - Q and Spherical Mode Decomposition

### 3.2.1 Quality Factor

Wheeler established a relation between an electric or magnetic dipole equivalent cylindrical volume with the radiation power factor, or $1/Q$. Chu correlated antenna quality factor and modal characteristics for $m=0$, for Transverse Electric or Magnetic, $TE_{0N}$ or $TM_{0N}$ respectively. Additional work [8-11] generalized the theory for different conditions including polarization, however the most-cited work on the subject restricts the theory to $TE_{0N}$ and $TM_{0N}$ radiation.

For a lossless, linearly polarized antenna, the antenna quality factor for the lowest order spherical mode is given [12].

$$Q_A \approx \left. \frac{1}{(ka)^3} \right|_{(ka) \ll 1} \tag{1}$$

Several different expressions for $Q_A$ exist and are still debated within the research community. However, impedance fractional bandwidth, *B,* and efficiency are the critical parameters for engineers and designers of small antennas.

A.D. Yaghjian and Steve Best derived a valuable relationship between impedance bandwidth and antenna quality factor for the case of a small antenna with a reactive matching element at resonance [13]. The derivation by Yaghjian is complete and general in form. A summary is presented below for the half-power fractional bandwidth of a lossless, small-antenna, impedance matched at resonance and propagating in a non-dispersive medium.

$$X_o(\omega) = X(\omega) + X_s(\omega) \tag{2}$$

$$\frac{\partial X_o}{\partial \omega_o} = \frac{\partial X}{\partial \omega_o} + \frac{|X_o|}{\omega_o} \tag{3}$$

An expression based for the fractional bandwidth is developed from the reflection coefficient. Specifically, the matched impedance bandwidth determined from the half-power frequencies,

$$\Gamma_{HP} = \frac{Z(\omega_-^+) - Z_o}{Z(\omega_-^+) + Z_o} = \frac{1}{\sqrt{2}} \qquad \text{and} \qquad \beta_{HP} = \frac{|\Gamma_{HP}|^2}{1 - |\Gamma_{HP}|^2} = 1$$

The half-power fractional bandwidth, where $\omega_-^+$ represents the upper and lower frequencies of the matched impedance bandwidth near $\omega_o$. For the half-power impedance bandwidth,

$$\frac{\left[X_o(\omega_-^+)\right]^2 + \left[R(\omega_-^+) - R_o\right]^2}{R(\omega_-^+)} = 4R_o \tag{4}$$

The relationship between the half-power fractional bandwidth and $\partial Z/\partial\omega$ is made with a Taylor series about $\omega = \omega_o$, where the fractional bandwidth $B_{HP} = \frac{\omega_+ - \omega_-}{\omega_o}$ 1.

$$B_{HP} \approx 4\left[\frac{R_o}{\omega_o |\partial Z/\partial\omega|}\right] \tag{5}$$

Field approach-

$$Q(\omega) = \frac{\omega \left| W(\omega) \right|}{P_A(\omega)} \tag{6}$$

$$P_A(\omega) = \frac{1}{2} \cdot \left| I_o \right|^2 R_o(\omega) \tag{7}$$

Yaghjian combined Maxwell's equations with the frequency derivative of Maxwell's equations to develop a field-based expression for $\partial X / \partial \omega \big|_{\omega=\omega_o}$

$$\left| I_o \right|^2 \frac{\partial X_o}{\partial \omega} = 4\left[ W(\omega) + W_L(\omega) + W_R(\omega) \right] \tag{8}$$

For a lossless ($W_L = 0$) antenna radiating in non-dispersive media, ($W_R = 0$) ,(8) simplifies to

$$W(\omega) = \frac{\left| I_o \right|^2}{4} \frac{\partial X_o}{\partial \omega}. \tag{9}$$

Substituting in quality factor (6) and for the case of highly reactive, low-radiation resistance electrically-small antennas

$$Q(\omega) = \frac{\omega}{2R_o} \left| \frac{\partial X_o}{\partial \omega} \right| \approx \frac{\omega}{2R_o} \left| \frac{\partial Z_o}{\partial \omega} \right| \tag{10}$$

For the specialized case of a small antenna radiating in a lossless, non-dispersive media, the relation between $Q$ and $B_{HP}$ is linked by $\partial X_o / \partial \omega$

$$Q(\omega) \approx \frac{2}{B_{HP}} \approx \frac{\omega}{2R_o} \sqrt{\left[ \frac{\partial R}{\partial \omega} \right]^2 + \left[ \frac{\partial X}{\partial \omega} + \frac{|X|}{\omega} \right]^2} \tag{11}$$

Yaghjian's relationship between $Q_A$ and $B_{HP}$ for a matched source antenna circuit is often overlooked, and $Q_A$ is typically calculated from (1). It is worth noting the simplicity of the inverse relationship in post-processing measured or simulated impedance data.

### 3.2.2 Spherical Mode Decomposition

Commercial method-of-moments programs offer spherical mode decomposition based on far-field radiated power. Computational algorithms may solve for the complex mode coefficients based on orthogonal separable functions, or utilize a point-matching method to overcome

computational obstacles. A summary of the solution approach using orthogonal functions is shown below [14, 15].

Harrington [14] defined the tangential field components $E_\theta = E_\theta(\theta,\phi)$ and $E_\phi = E_\phi(\theta,\phi)$ are related to the radial components of the vector potentials $F_r$ and $A_r$

$$\overline{E} = \begin{Bmatrix} E_\theta \\ E_\phi \end{Bmatrix} = \frac{1}{r}\begin{bmatrix} -\left(\frac{1}{\sin\theta}\right)\frac{\partial}{\partial\phi} & \frac{\partial}{\partial\theta} \\ \frac{\partial}{\partial\theta} & \left(\frac{1}{\sin\theta}\right)\frac{\partial}{\partial\phi} \end{bmatrix}\begin{Bmatrix} F_r \\ \left(\frac{1}{j\omega\varepsilon}\right)\frac{\partial A_r}{\partial r} \end{Bmatrix} \tag{5}$$

where $F_r$ and $\frac{\partial A_r}{\partial r}$ may be decoupled and defined in terms of $E_\theta$ and $E_\phi$

$$F_r = f\left(E_\theta, E_\phi\right) \quad ; \quad \frac{\partial A_r}{\partial r} = g\left(E_\theta, E_\phi\right) \tag{6}$$

The functions $F_r$ and $A_r$ may be represented as spherical-mode expansions given by

$$F_r = \sum_{o}^{n}\sum_{-m}^{+m} f_{mn} P_n^{|m|} e^{jm\phi} \quad ; \quad A_r = \sum_{o}^{n}\sum_{-m}^{+m} a_{mn} P_n^{|m|} e^{jm\phi} \tag{7}$$

where $P_n^{|m|} = P_n^{|m|}(\cos\theta)$, and the $\phi$ dependence is expressed in complex exponential form. The coefficients $f_{mn}$ and $a_{mn}$ may be solved directly with the orthogonal relationship

$$\int_0^{2\pi}\int_0^{\pi} P_n^m \cdot P_p^q \cdot e^{j(m-q)\phi} \sin\theta d\theta d\phi = 2\pi \cdot \left[\frac{2}{2n+1}\cdot\frac{(n+m)!}{(n-m)!}\right] = \frac{1}{K_{mn}} \tag{8}$$

The general form of complex mode coefficients used for relative power comparisons

$$f_{mn} = \left[\frac{K_{mn}}{r}\right]\cdot\int_0^{2\pi}\int_0^{\pi}\left\{-\frac{\partial}{\partial\theta}\left[\sin\theta E_\phi\right] + \frac{\partial}{\partial\varphi}E_\theta\right\}P_n^{|m|}e^{-jm\phi}d\theta d\phi \tag{10}$$

$$a_{mn} = j\omega\varepsilon\cdot\left[\frac{K_{mn}}{r}\right]\cdot\int_0^{\pi}\int_0^{2\pi}\left\{-\frac{\partial}{\partial\theta}\left[\sin\theta E_\theta\right] - \frac{\partial}{\partial\phi}E_\phi\right\}P_n^{|m|}e^{-jm\phi}d\theta d\phi\,. \tag{11}$$

Fig. 3.1 tabulates the $E_\theta$ and $E_\Phi$ three-dimensional radiation patterns from a single $TM_{mn}$ source for $m \le n$, $n$ = [*1,2,3*]. One may observe the omnidirectional characteristic of the *m=0* patterns

for $n=1, 2, 3$ with no $E_\Phi$ component. Cross-polarization in mode compositions appears for $m \geq 1$ in both $E_\theta$ and $E_\Phi$.

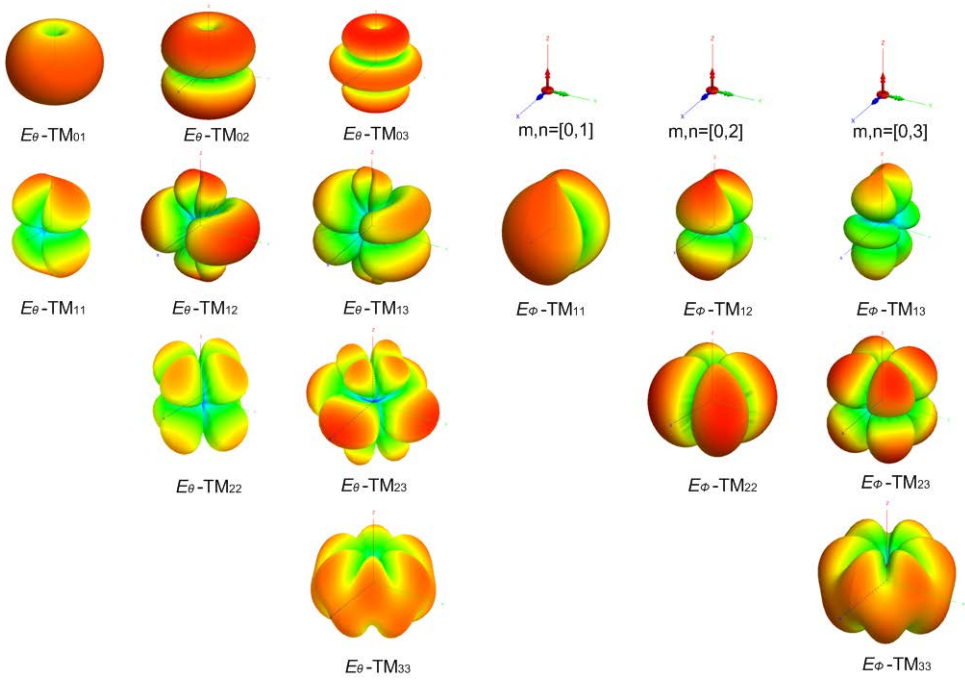


**Fig. 3.1 Three-dimensional $E_\theta$ and $E_\Phi$ radiation patterns from a single $TM_{mn}$ source for $m \leq n$, $n=[1,2,3]$. The far-field patterns are calculated in FEKO for single-mode source excitations. Omnidirectional in azimuth is observed for the $m=0$ patterns for $n=0, 1, 2, 3$ with no $E_\Phi$ components. Cross-polarization in mode compositions appears for $m \geq 1$ in both $E_\theta$ and $E_\Phi$.**

## 3.3 Examples of Approach

Two examples chosen to illustrate the approach utilize short monopoles mounted on finite-ground planes. The first compares the far-field modal distributions versus finite ground plane size for identical short monopoles over circular and square ground planes. The second example illustrates the near-field to far-field modal distributions for identical monopoles mounted over a small ($S=2a$) and approaching large ($S=\lambda$) ground planes to illustrate the variations in modal distributions.

A comparison of the square and the circular ground plane example illustrates the region ( $S \approx \lambda/2$) where differences in modal distributions become apparent. Range values are varied for the

near field algorithm to plot the transition of modal powers from the beyond the radiansphere to the far field modal powers calculated using commercial software (FEKO).

### 3.3.1 Electrically-Small Antenna Ground Plane Interaction - Modal Analysis

Early investigations of electrical properties of center-mounted monopoles over finite ground planes selected circular ground plane geometries, for analytical validation [16], or because the electrical characteristics are a function primarily of the element length, element radius and ground plane radius [17]. Wireless device packaging has shifted the interest in the direction of square, rectangular and edge-mounted geometries.

The following example demonstrates the far-field modal power distribution of a short center-mounted monopole for the square and circular ground plane geometries. The element is a short monopole with reactive loading to resonate at $f=1.0$ GHz. The height is chosen such that $ka \approx 1$. The side length of the square ground plane is increased in a similar manner to the radius of the circular ground plane. Modal radiated power percentages below $P_{MN}<0.5\%$ are omitted from the following tables for clarity. The results show all power radiated may be characterized by $TM_{0N}$ for $N=1, 2$ modes.

Fig. 3.2 is a rendering of $TM_{0N}$ modes for $N=1$-$4$. Combinations of $TM_{0N}$ modes are still omnidirectional with higher order modes typically present to account for the dimpling and shaping of the pattern due to the finite ground plane.

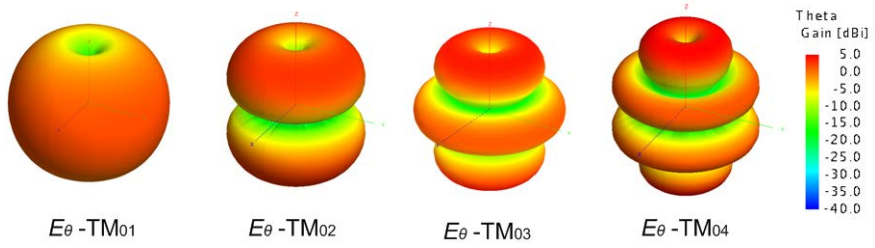


**Fig. 3.2. $E_\theta$ Mode Components for $TM_{0N}$. The four far-field patterns are calculated in FEKO for single $TM_{0N}$ source excitations.**

Modal power percentages shown in Fig. 3.3 (a) and (b) are presented for both the square and round ground plane of the limiting cases of a vanishing ground plane and the ground plane approaching infinity. Some differences appear in the half-wavelength region of the two plots. The coupling between the monopole element and the finite ground plane referred to by Best [1]

would appear to be the response of the $TM_{02}$ component in the half-wavelength region for both the square and circular ground planes.

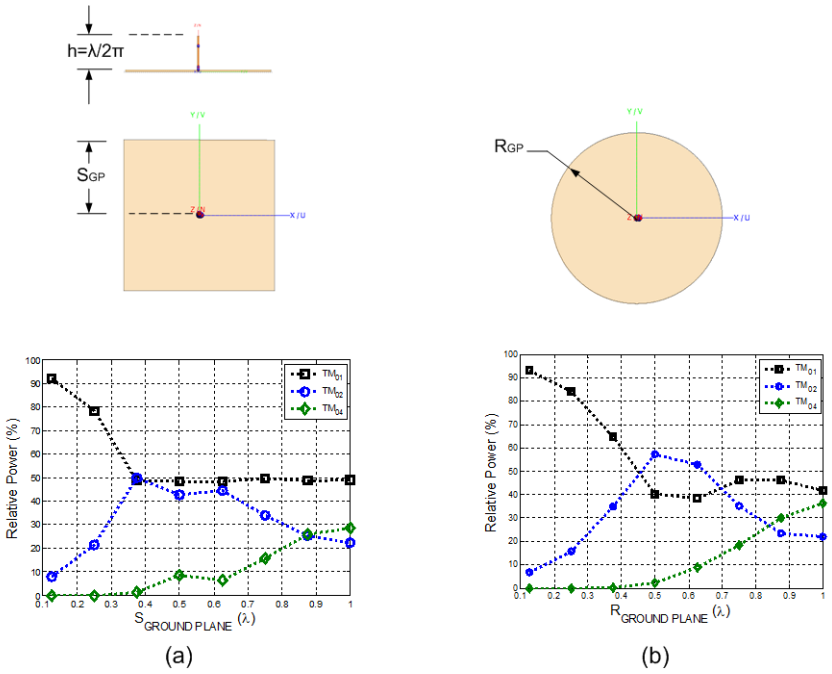


**Fig. 3.3. Geometry and modal compositions for identical short monopole elements at the centers of square and circular small ground planes. Both the square side length $S_{GP}$ and the circular radius $R_{GP}$ are varied from up to one wavelength. The results shown were far-field mode decomposition results from FEKO radiation pattern calculations.**

### 3.3.2 Far-field versus Near-field Spherical Mode Decomposition

A near-field mode decomposition algorithm was developed as part of the dissertation research. Tangential field quantities computed from calculated near-field strengths are read into a MATLAB subroutine that performs the spherical mode decomposition integrations described earlier. Comparisons of the modal components as a function of the radial distance to the field point are presented as a first step to validate the near-field algorithm.

Fig. 3.4 includes a side view (a) and top view (b) the test geometry parameters. The antenna height is chosen such that $ka \approx 1$, where $h=a$. Two ground plane sizes are chosen: the smaller, $S_{GP}=2a=\lambda/\pi$, and $S_{GP}=\pi$.

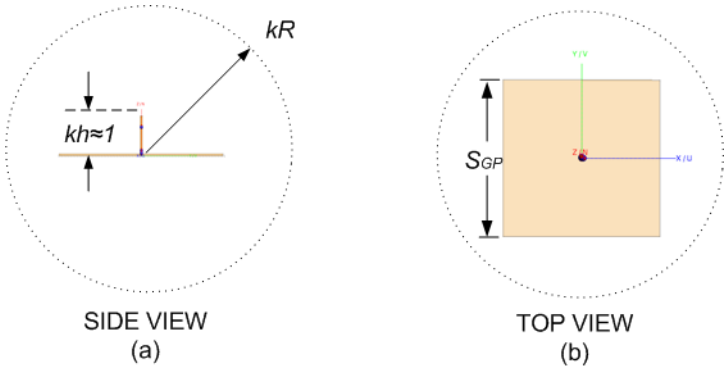


**Fig. 3.4. CADFEKO rendering of short monopole of finite ground plane. The side view (a) and top view (b) of short monopole are shown mounted at center of small, square ground plane.**

Fig. 3.5 plots the near-field to far-field modal power compositions for the two finite ground plane cases. The smaller ground plane has a modal power composition that is similar to a dipole, because nearly all the ground plane is enclosed by the radiansphere volume. There is some variation as $kR \rightarrow \infty$ and the $TM_{01}$ components for the larger values of $kR$ converge to the far-field values calculated with the commercial method-of-moments solver (FEKO).

For small values of $kR$, the larger ground has a modal power distribution similar to that of a dipole, however the power is evenly split between the $TM_{01}$ and $TM_{02}$ for larger values of $kR$ as they converge to the far-field percent power values.

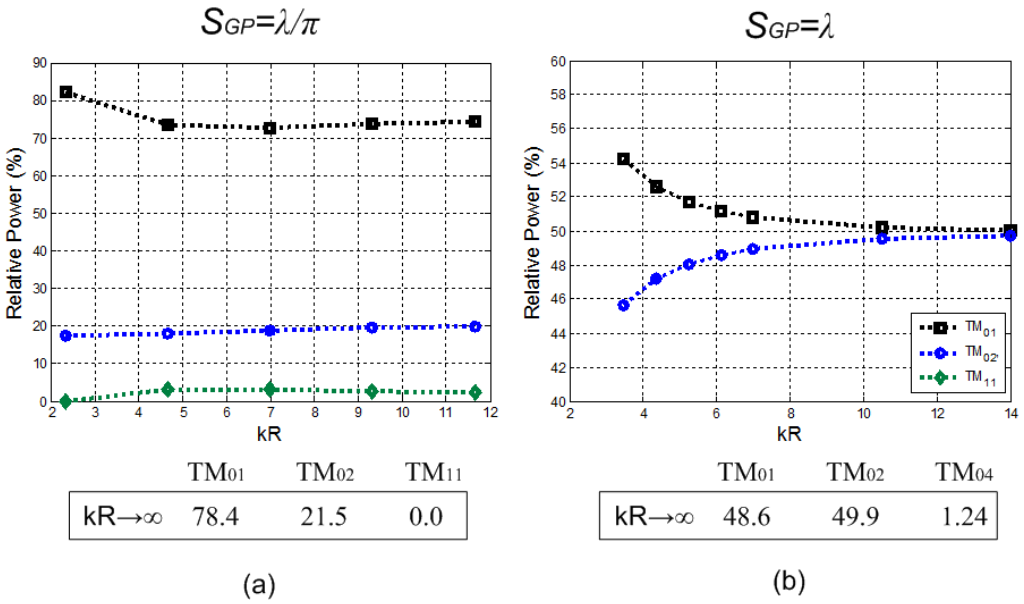


**Fig. 3.5. Near-Field to Far-field Modal Power Compositions versus *kR* for $S_{GP}$ of *2a=λ/π* and *λ*. The far-field values shown for *kR*→∞ were far-field mode decomposition results obtained from FEKO simulations.**

## 3.4 Low-Profile Example – Microstrip Patch Antenna

An example with the microstrip patch antenna is presented to illustrate the utility of the matched half-power bandwidth algorithm from Yaghjian and Best. The microstrip antenna is low-profile, easy to manufacture and has multiple applications in satellite communications. The microstrip antenna is a resonant structure with an overall dimension on the order of one-half wavelength, which precludes it from the class of electrically-small antennas presented in Chapter 4.

Fig. 3.6 is an engineering perspective of a probe-fed, square, microstrip patch antenna model created for the analysis. Dimensions and material properties for the square microstrip patch antenna are presented in Table 4. The antenna is designed for a resonant frequency of $f \approx 1.0GHz$. The substrate is modeled as a volume of lossless media with a relative permittivity of $\varepsilon_R=1.05$. Fig. 3.7. Calculated complex impedance response (a) and VSWR (b) of square microstrip patch antenna mounted on a finite ground plane, $S_{GP} \approx \lambda$. The impedance responses shown were calculated using FEKO. shows the parallel resonance complex impedance response (a), and the corresponding VSWR with a reference impedance of $R_o=50\ \Omega$. The 2:1 VSWR bandwidth determined primarily from the height is approximately *4 %*.

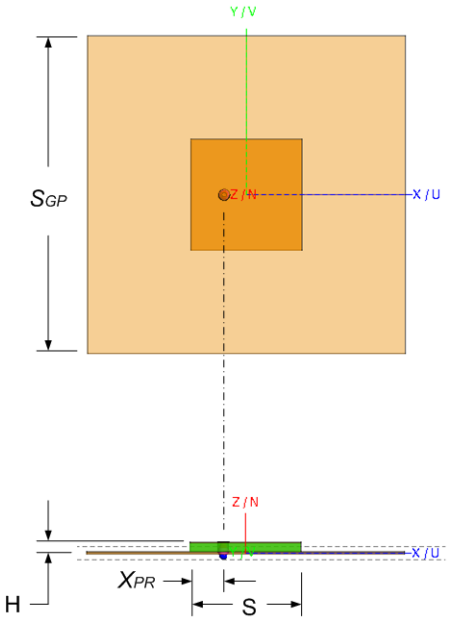


**Fig. 3.6. A probe-fed, square microstrip patch antenna mounted on a finite ground plane, $S \approx \lambda$. The antenna is designed for a resonant frequency of $f \approx 1.0$ GHz. A lossless low-valued dielectric has been chosen to maximize bandwidth.**

| $S_{GP}$ [cm] | $S$ [cm] | $H$ [cm] | $X_{PR}$ [cm] | $\varepsilon_R$ [ ] | $tan\delta$ [ ] |
|---|---|---|---|---|---|
| 32 | 12.5 | 1.0 | 3.74 | 1.05 | 0.0001 |

**Table 4. Dimensions and material properties for the square microstrip patch antenna (see Fig. 3.6).**

Fig. 3.7 (a) and (b) are three-dimensional $E_\theta$ and $E_\phi$ Radiation Patterns for the square microstrip patch antenna mounted on a finite ground plane. Maximum radiation visualized from the fringing currents as two radiating slots or magnetic dipole, is normal to the planar surface. The surface currents from the top plate contribute to the magnetic dipoles to create nulls in both the $E_\theta$ and $E_\phi$ patterns.

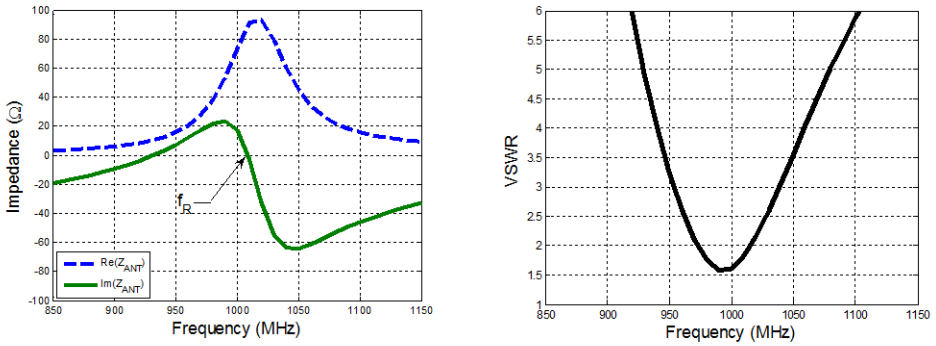


**Fig. 3.7. Calculated complex impedance response (a) and VSWR (b) of square microstrip patch antenna mounted on a finite ground plane, $S_{GP} \approx \lambda$. The impedance responses shown were calculated using FEKO.**

Fig. 3.8 is the normalized complex impedance response for the square microstrip-patch antenna in the same configuration. The solid trace is the complex impedance response normalized to the $R_{RAD}$ at resonance. Based on $Q$-$B_{HP}$ relationship developed by Yaghjian and Best, the half-power bandwidth of the matched impedance response should yield a very good estimate of the system $Q$ and one-half $Q_A$ for the single resonant element. $Q_A$ may be directly calculated from the antenna input impedance as [12]

$$Q_A(\omega) \approx \frac{2}{B_{HP}} \approx \frac{\omega}{2R_o}\sqrt{\left[\frac{\partial R}{\partial \omega}\right]^2 + \left[\frac{\partial X}{\partial \omega} + \frac{|X|}{\omega}\right]^2} \,. \tag{12}$$

Both $\partial R/\partial \omega$ and $\partial X/\partial \omega$ are determined from a linear approximation from the adjacent points from the impedance response data. Table 6 is a listing of the $Q$ and half-power bandwidth data collected from the resonance-matched impedance response shown in Fig. 3.8.

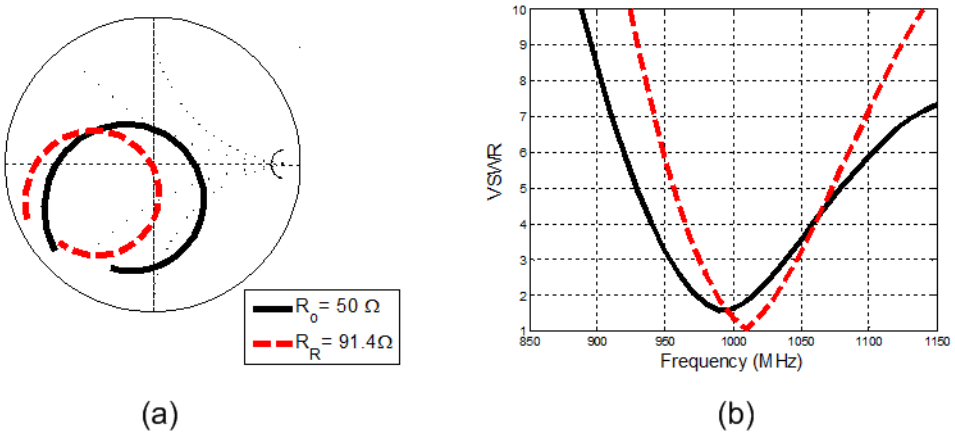


**Fig. 3.8. Smith chart impedance response for the square microstrip patch antenna geometry shown in Fig. 3.6 mounted on a finite ground plane. *Q* is determined directly from the VSWR bandwidth calculated with reference impedance equal to the antenna radiation resistance at resonance.**

| $f_R$ [GHz] | $R_R$ [Ω] | $X_R$ [Ω] | $Q$ [cm] | $f_L$ [GHz] | $f_L$ [GHz] | $B_{HP}$ [%] | $Q_{HP}$ [ ] |
|---|---|---|---|---|---|---|---|
| 1.01 | 91.4 | -3.1 | 14.8 | 0.94 | 1.09 | 14.9 | 6.7 |

**Table 5. Calculated impedance values at resonance and half-power bandwidth frequencies to calculate quality factor(s) for the antenna geometry shown in Fig. 3.6 and Table 4. The values shown were found using FEKO.**

The information relating antenna quality factor to fractional bandwidth is useful from a designer perspective. Quality factor for electrically-small antennas is typically used as a figure-of-merit relative to a lowest-order, single-mode fundamental limit. The relationship of $Q$ to fractional bandwidth for a general antenna, not the smallest, is applicable for antenna designs for wireless terminals.

The second half of the microstrip antenna example examines the far-field percent power spherical mode distributions. The far-field spherical mode coefficients are calculated directly from the method-of-moments software (FEKO) used for all models in the dissertation.

Table 6 collects data from the far-field mode decomposition for the microstrip patch antenna. A first look at the far-field relative power percentages for the microstrip antenna shown indicates that less than 5% of the power radiated to the far-field is omnidirectional ($TE_{0N}$ or $TM_{0N}$). Nearly equal power is distributed between the $TM_{11}$ and $TE_{11}$ modes. With correct phasing, the MSA may be designed for circular polarization, within a limited sector defined by the Axial Ratio.

| | $TM_{mn}$ | | | $TE_{mn}$ | | |
|---|---|---|---|---|---|---|
| ***m*** | ***n=1*** | ***n=2*** | ***n=3*** | ***n=1*** | ***n=2*** | ***n=3*** |
| -1 | 17.3 | 7.4 | 2.1 | 16.2 | 4.4 | - |
| 0 | 2.0 | 1.6 | - | - | - | - |
| +1 | 17.3 | 7.4 | 2.1 | 16.1 | 4.4 | - |

**Table 6. Far-field relative power percentages *TMmn -TEmn* data for square microstrip patch antenna mounted on a finite ground plane (see Fig. 3.6). Far-field radiation patterns and corresponding mode decompositions were obtained using FEKO.**

An underlying stipulation of small antenna theory is the omnidirectional radiation characteristic is the $TM_{01}$ or $TE_{01}$ is assumed when discussing fundamental limits. A design guideline typically halves the quality factor (doubles the fractional bandwidth) to estimate optimum realizable performance of a practical system.

## 3.5 Summary

A number of realistic antennas fit within the broad definition of small antennas ($ka \leq 1$) but are somewhat larger than the stricter definition ($ka \leq 0.5$). The range $0.5 \leq ka \leq 1$ is valuable territory for antenna system design. Self-resonant antennas exist in this range, which also includes several wideband small antennas. A combined approach of working with the quality factor calculated or extracted from impedance response data, with near-and far-field modal analyses to characterize bandwidth, radiation patterns, and ground plane compatibility facilitates the analysis of several different narrow and wide-bandwidth antennas in Chapters 4 and 5.

## 3.6 References


[ 1] S.R. Best, "A Discussion on Small Antennas Operating with Small Finite Ground Planes," 2006 IEEE, pp. 152-155.

[ 2] Henry Jasik, *Antenna Engineering Handbook*, McGraw-Hill, 1961, pp. 3-23

[ 3] M.M. Weiner, "Monopole Element at the Center of a Circular Ground Plane Whose Radius is Small or Comparable to Wavelength," IEEE Transactions on Antennas and Propagation, vol. 35, no. 5, May 1987, pp. 488-495.

[ 4] M.C. Huynh, W.L. Stutzman, "Ground Plane Effects on Planar-Inverted-F Antenna (PIFA) Performance," IEE Proceedings on Microwaves Antennas and Propagation, vol. 150, no. 4, August 2003, pp.209-213.

[ 5] D.F. Sievenpiper et al., “Experimental Validation of Performance Limits and Design Guidelines for Small Antennas,” IEEE Transactions on Antennas and Propagation, vol. 60, no.1, January 2012, pp.8-19.

[ 6] M.C. Huynh, "Wideband Compact Antennas for Wireless Communication Applications," Ph.D. Dissertation, Virginia Tech Department of Electrical and Computer Engineering, Nov. 22, 2004

[ 7] J.S. McLean, "A Re-Examination of the Fundamental Limits on the Radiation Q of Electrically-Small Antennas," IEEE Transactions on Antennas and Propagation, vol. 44, no. 5, May 1996, pp.672-676.

[ 8] H.A. Wheeler, "The Radiansphere Around a Small Antenna," Proc. IRE, vol. 47, 1959, pp. 1325-1331.

[ 9] R. Collin and S. Rothschild, "Evaluation of Antenna Q," IEEE Transactions on Antennas and Propagation, vol. 12, 1964, pp. 23-27.

[10] R.L. Fante, "Quality Factor of General Ideal Antennas," IEEE Transactions on Antennas and Propagation, vol. 17, no. 3, March 1969, pp. 151-155.

[11] J.S. McLean, "A Re-Examination of the Fundamental Limits on the Radiation Q of Electrically-Small Antennas" , IEEE Transactions on Antennas and Propagation, vol. 44, no. 5, May 1996, pp.672-676.

[12] A.D. Yaghjian, S.R. Best, "Impedance, Bandwidth, and Q of Antennas" , IEEE Transactions on Antennas and Propagation, vol. 53, no. 4, April 2005, pp.1298-1324.

[13] J.L. Volakis , C.-C. Chen, and K. Fujimoto, *Small Antennas: Miniaturization Techniques and Applications*. New York: McGraw-Hill 2010, pp.95-103

[14] Lecture Notes provided by W.A. Davis and Taeyoung Yang

[15] R.F. Harrington, "*Time-Harmonic Electromagnetic Fields*," McGraw-Hill, 1961

[16] J.E. Storer, "The Impedance of an Antenna over a Large Circular Screen," Journal of Applied Physics, vol. 12, August 1951, pp.1058.

[17] M.M. Weiner, 'Monopole Element at the Center of a Circular Ground Plane Whose Radius is Small or Comparable to Wavelength," IEEE Transactions on Antennas and Propagation, vol.35, no.5, May 1987, pp.488-495.

# 4 CHAPTER - Narrowband Reconfigurable, Active Antenna Systems

## 4.1 Introduction

Current handheld communication devices are designed primarily for cellular and microcellular architectures. Free-space wavelengths are on the order of $\lambda \approx 30cm$ *(1ft)*. Cell-tower antenna arrays are vertically-polarized at low elevations. Portable devices should maximize pattern directivity at low elevation angles and coverage should be omnidirectional in azimuth. A spherical mode decomposition of radiation patterns should be primarily composed of an $m=0$ component representations for small antennas. Power observed in the $m \neq 0$ mode distributions reduce efficiency of the communication link and is equivalent to system loss for a vertically-polarized antenna system.

Chapter Four implements the far-field and near-field modal decomposition methods illustrated in the previous chapter to review and investigate several configurations of the traditional monopole and more modern planar inverted-F antenna integrated into a handheld device fixture. The first example is a continuation of the ground plane exercise introduced in the previous chapter. A short-monopole is mounted in two different locations on an approximate handheld fixture to illustrate the change in radiation patterns both visually and in terms of modal content.

The planar inverted-F antenna is a very popular, small and relatively low-profile, vertically-polarized communications antenna characterized by radiation patterns that are nearly omnidirectional in the azimuth (XY) plane. An introductory finite-ground plane example is presented before configuring it on the same hand-held fixture used for the monopole exercise.

An investigation of the bandwidth properties of the PIFA when subjected to reduction in height is then considered with some useful small antenna design guidelines. Current research trends to miniaturize antennas are investigated with practical examples.

## 4.2 Short Monopole Placement in Handheld Device Configuration

A realistic example of a single antenna coupling differently to a finite structure is presented. A short ($h_{MP} \approx \lambda/2\pi$) monopole shown in Fig. 4.1, is mounted at two common locations of a representative perfect-electric-conductor (PEC) handheld device fixture. Short monopoles are typically rugged antennas, but the position of a monopole on a handheld chassis is a good entry-point for investigating narrowband devices interacting with the immediate near-field.

Fig. 4.1 is an illustration of the monopole used in the previous chapter integrated to a metallic handheld device. The monopole height is approximately 5 cm, the chassis dimensions are shown in Table 7. Center-mount and edge-mount on the top of the structure are the two positions.

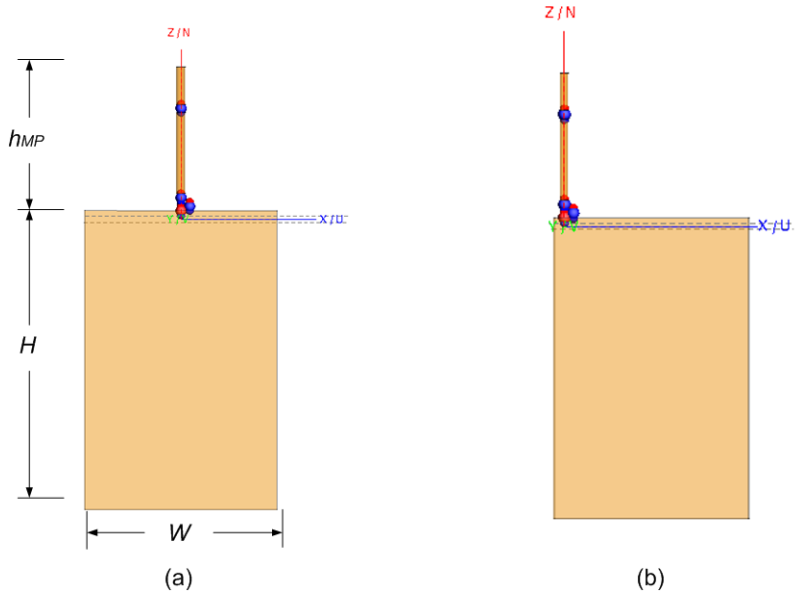


**Fig. 4.1 CADFEKO renderings of center-mounted (a) and edge-mounted (b) short monopole integrated to a handheld device.**

| $h_{MP}$ [cm] | $H$ [cm] | $W$ [cm] | $D$ [cm] |
|---|---|---|---|
| 4.77 | 10.0 | 6.5 | 4.0 |

**Table 7. Dimensions (in cm) of the short monopole (shown in Fig. 4.1) integrated to a handheld device.**

Fig. 4.2 compares the $E_\theta$ and $E_\Phi$ radiation patterns for the center-mount and edge-mount geometries respectively. The center-mount monopole couples to the fixture and sets up symmetric surface currents on the chassis. The resulting patterns are primarily $TM_{01}$ and $TM_{02}$.

The edge mount geometry illustrates the inevitable asymmetry due to the location of the monopole element. Surface currents on the chassis are altered with asymmetric contributions to the total radiation. The resulting nulls or dimples in the patterns are represented with additional modes in the *TM* and *TE* power distributions. Table 4.2.1 provides the *TM* mode representations for the center- and edge- mounted monopole geometries. Approximately 25% of the far-field radiated power is transferred $m \neq 0$ modes.

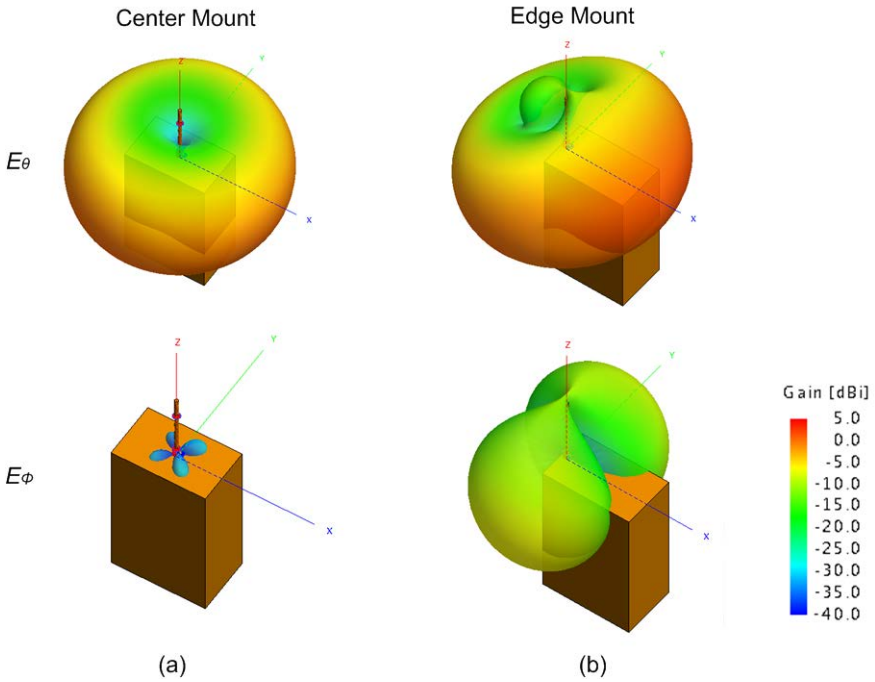


**Fig. 4.2 Three-Dimensional $E_\theta$ and $E_\Phi$ Radiation Patterns for the Center and Edge Mounted Monopoles. Far-field radiation patterns were obtained using FEKO.**

| | Center-Mount Monopole | | Edge-Mount Monopole | |
|---|---|---|---|---|
| *m* | *n=1* | *n=2* | *n=1* | *n=2* |
| -1 | - | - | 8.7 | 2.2 |
| 0 | 86.7 | 12.6 | 66.8 | 7.9 |
| +1 | - | - | 8.7 | 2.2 |

**Table 8.** ***$TM_{mn}$*** **mode compositions for center and edge-mounted monopoles shown in Fig. 4.2. The far-field mode decompositions were obtained using FEKO.**

Minimal detuning due to the physical geometry of the monopole location is also shown in the impedance response plots shown in Fig. 4.3 (a) Smith Chart and (b) VSWR response.

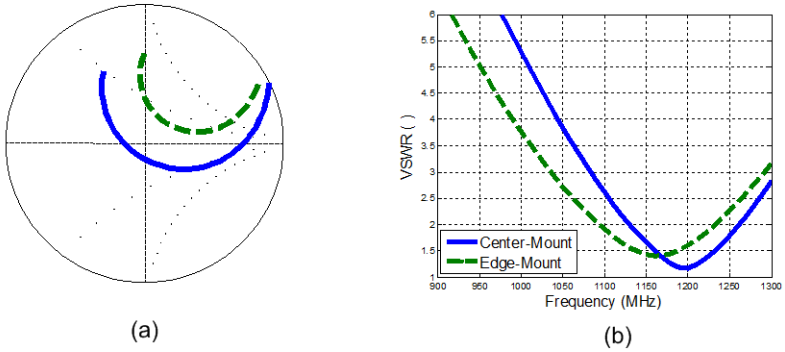


**Fig. 4.3. Normalized Impedance (a) and VSWR (b) responses for center-mount and edge-mounted monopoles on a handheld device shown in Fig. 4.2. Impedance calculations were obtained using FEKO.**

The monopole on the mobile device is not highly sensitive to either of the two locations. The dimpling of the pattern as a result of the edge mount geometry is minimal, and the pattern remains predominately omnidirectional. Dielectric loading with a hand or head will result in some additional pattern forming, but a majority of the power radiated into the far-field will remain in the $TM_{0N}$ modes. Surface currents that are established on the mobile terminal chassis will create a sufficient counterpoise to maintain low-order *TM* modes. A more common antenna for current handheld devices is the planar inverted-F antenna (PIFA), allowing an embedded type of structure. In the next section we consider the basic PIFA and then evaluate the performance when mounted on a handheld device.

## 4.3 Planar Inverted-F Antenna

Many portable device-integrated designs are based upon the planar inverted-F antenna (PIFA). The low-profile, single-resonant class antenna has evolved in aerospace applications from the inverted -L (bent monopole) with a parallel stub gamma section for impedance matching, and is planar to increase conductor surface area and resulting impedance bandwidth.

The PIFA shown in Fig. 4.4 is attached to a center of a finite ground plane. The geometry chosen for the model is similar to the simulated and measured results from Huynh [1]. Dimensions for the scaled model are included in Table 5. Fig. 4.5 includes the complex impedance and VSWR responses for the unmatched ($R_O$=50Ω) and matched ($R_R$=64.1Ω) reference loads. Table 10 presents the calculated values for antenna and system quality factors. The half-power fractional bandwidth is approximately fourteen percent, but the impedance bandwidth (VSWR<2.1) is less than five percent.

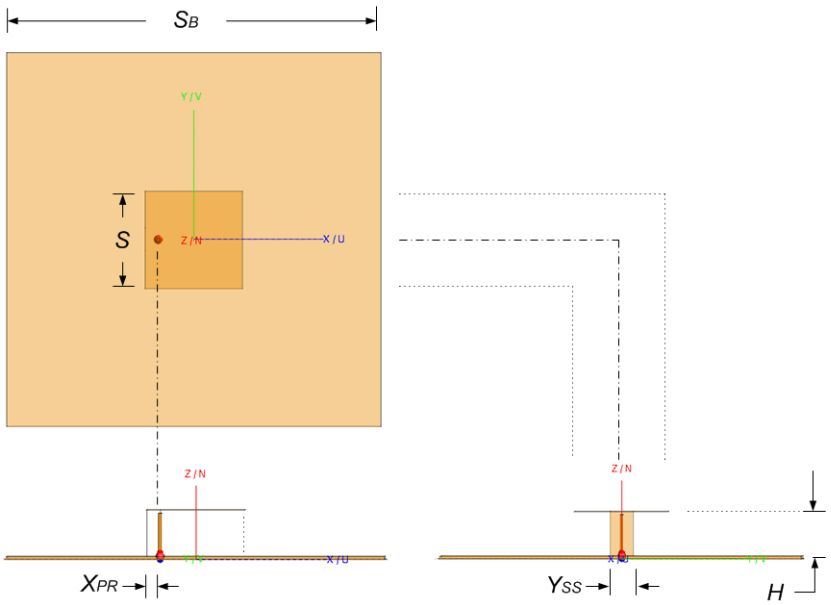


**Fig. 4.4. A three-view CADFEKO rendering of the conventional PIFA model.**

| $S_B$ [cm] | $S$ [cm] | $H$ [cm] | $X_{PR}$ [cm] | $Y_{SS}$ [cm] | $ka$ [ ] |
|---|---|---|---|---|---|
| 15.0 | 3.91 | 1.86 | 0.54 | 1.0 | 0.70 |

**Table 9. Dimensions (in cm) of the conventional PIFA geometry shown in Fig. 4.4**

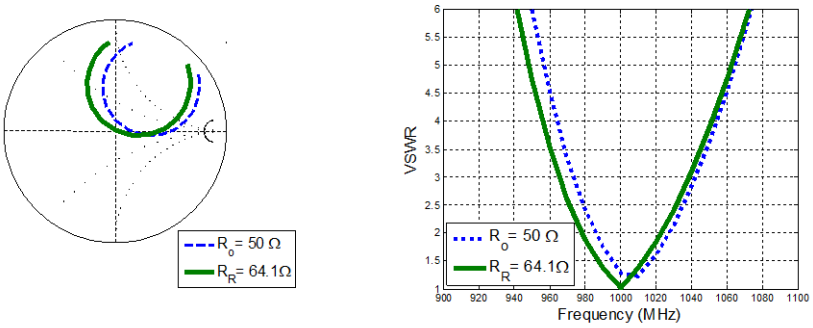


**Fig. 4.5. Smith Chart (a) and computed VSWR (b) of a conventional PIFA shown in Fig. 4.4. Impedance responses were calculated using FEKO.**

| $f_R$ [GHz] | $R_R$ [Ω] | $X_R$ [Ω] | $Q$ [cm] | $f_L$ [GHz] | $f_H$ [GHz] | $B_{HP}$ [%] | $Q_{HP}$ [ ] |
|---|---|---|---|---|---|---|---|
| 1.0 | 64.1 | 1.1 | 18.6 | 0.94 | 1.08 | 14 | 7.1 |

**Table 10. Resonance and half-power bandwidth tabulated values for the PIFA shown in Fig. 4.4.**

Fig. 4.6 (a) and (b) include three-dimensional renderings of the $E_\theta$ and $E_\phi$ radiation patterns for the PIFA mounted on a finite ground plane. Table 11 lists the far-field percent power mode distribution for the conventional PIFA. The $E_\theta$ radiation patterns in the XZ and YZ plane are essentially omni-directional, however, nearly 30% of the power is not in $TM_{0N}$ components. Approximately 65% of the radiated power is in the $TM_{0N}$ modes with 20% in the $TM_{11}$ and a result of the pattern shaping from the finite ground plane. Just over 10% of the far-field radiated power is horizontally polarized and represented by the $TE_{11}$ modes.

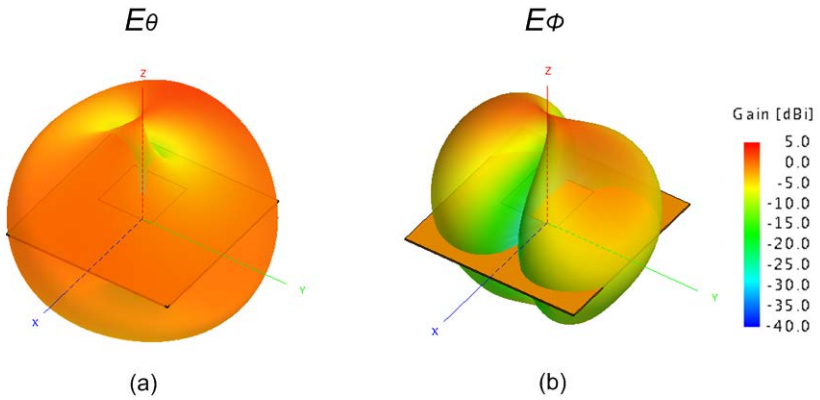


**Fig. 4.6. Three-dimensional radiation patterns for the conventional PIFA shown in Fig. 4.4 ($S_{GP}$ = $0.4\lambda$). The (a) $E_\theta$ and (b) $E_\Phi$ radiation patterns were calculated in FEKO.**

| | $TM_{mn}$ | | $TE_{mn}$ | |
|---|---|---|---|---|
| ***m*** | ***n=1*** | ***n=2*** | ***n=1*** | ***n=2*** |
| -1 | 10.5 | - | 5.4 | - |
| 0 | 60.5 | 6.5 | - | - |
| +1 | 10.6 | - | 5.4 | - |

**Table 11. Calculated far-field *TM* and *TE* mode compositions for conventional PIFA shown in Fig. 4.4. Far-field radiation patterns and corresponding mode decompositions were calculated using FEKO.**

Fig. 4.7 is an illustration of the same PIFA mounted on a similar mobile chassis shown in the monopole example. Fig. 4.8 contains both Smith Chart (a) and VSWR (b) forms of the impedance response. Minimal detuning for the PIFA is the result of the antenna's monopole characteristic and predominately vertical surface currents established on the handheld fixture. Fig 4.9 (a) and (b) are $E_\theta$ and $E_\Phi$ Radiation Patterns for the conventional PIFA mounted on chassis.

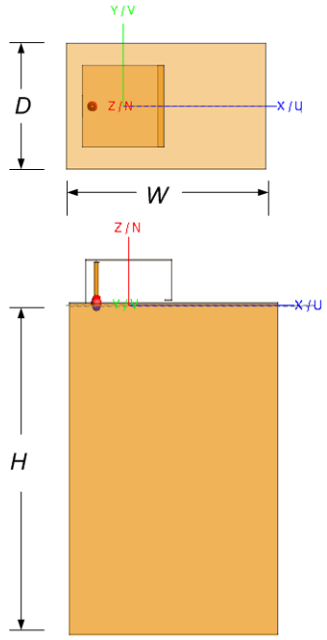


**Fig. 4.7. CADFEKO model rendering of conventional PIFA integrated to a handheld device. The dimensions of the chassis are approximately *H=10cm* tall, *W=6.5cm*, and *D=4cm*.**

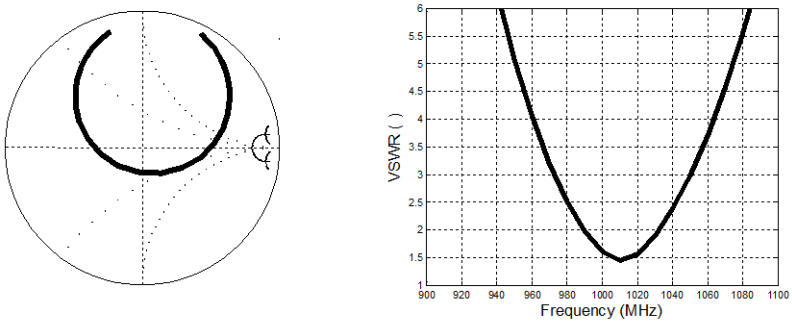


**Fig. 4.8. Normalized Impedance (a) and VSWR (b) responses for PIFA integrated to Handheld Device. Impedance response calculations were obtained using FEKO.**

| $f_R$ [GHz] | $R_R$ [Ω] | $X_R$ [Ω] | $Q$ [ ] | $f_L$ [GHz] | $f_L$ [GHz] | $B_{HP}$ [ ] | $Q_{HP}$ [ ] |
|---|---|---|---|---|---|---|---|
| 1.04 | 21.2 | 3.62 | 19.6 | .98 | 1.1 | .115 | 8.67 |

**Table 12. Resonance and Half-Power Bandwidth Tabulated Values for the PIFA integrated to the handheld device shown (see Fig. 4.7).**

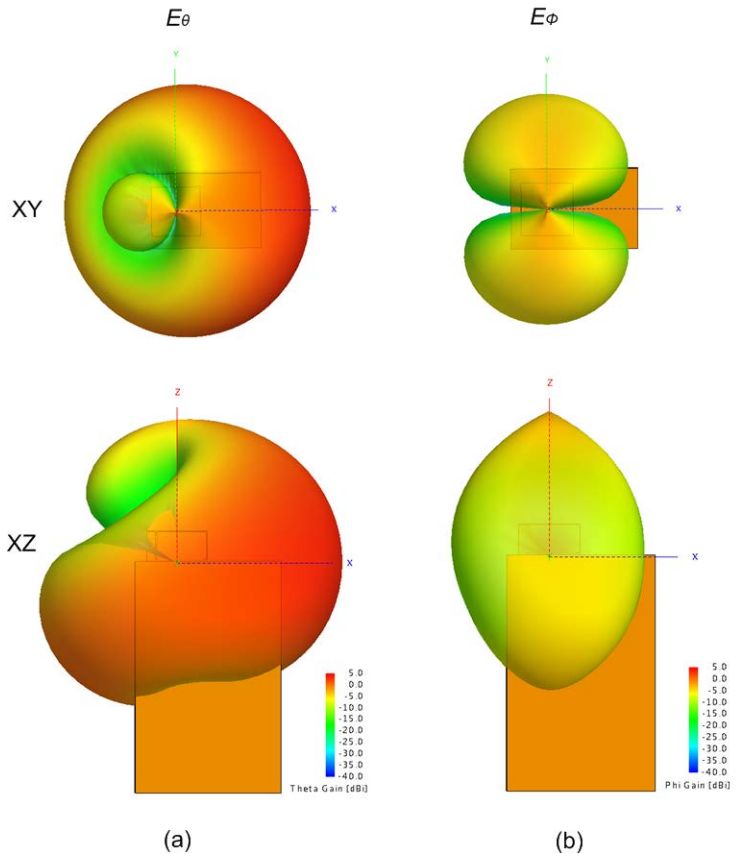


**Fig 4.9.** ***$E_\theta$*** **and** ***$E_\phi$*** **Radiation Patterns for Conventional PIFA mounted on Handheld Structure. The** ***$E_\theta$*** **(a) and** ***$E_\phi$*** **(b) radiation patterns were calculated in FEKO.**

| | | ***$TM_{mn}$*** | ***$TE_{mn}$*** | |
|---|---|---|---|---|
| ***m*** | ***n=1*** | ***n=2*** | ***n=1*** | ***n=2*** |
| -1 | 8.3 | 1.0 | 7.7 | - |
| 0 | 58.8 | 6.1 | - | - |
| +1 | 8.3 | 1.0 | 7.7 | - |

**Table 13. Far-Field *TM* and *TE* mode Compositions for PIFA mounted on Handheld Structure. Far-field radiation patterns and corresponding mode decompositions were calculated using FEKO.**

The PIFA shown in the finite ground plane and ground plane geometries provides a sufficient omnidirectional radiation pattern with some horizontal polarization as a result of the surface currents on the top plate of the antenna element. The height of the PIFA for the two examples is nearly 2 cm. A slightly more uniform $E_\theta$ radiation pattern would result from repositioning the PIFA to the center of the handheld. However, Huyhn and Stutzman [1] observed that PIFAs

realize better gain and bandwidth performance when the short-circuit plate is near the ground plane edge. It should be noted that the pattern of the PIFA on this handheld is similar to the monopole mounted near the edge of the platform. This suggests the primary radiation from the PIFA is emanating from the shorting bar of the PIFA that is near the edge.

A parameter of interest for potential applications of integrating a PIFA to a portable device is the effect of the structure height on the bandwidth. The next section investigates a capacitance-loaded PIFA subjected to a controlled reduction height. Small antenna parameters and modal content are considered for the height reduction exercise with other variables (e.g., form factor, $f_R$) held constant.

### 4.3.1 Height Reduction Discussion

The following exercise investigates the PIFA impedance bandwidth as a function of the PIFA height. The purpose of the investigation is to validate the relation of $Q$ to $B_{HP}$ developed by Yaghjian for practical antennas in the small antenna range of $0.5<ka<1.0$, as well as a comparison to the fundamental limit in a volumetric sense. It is interesting to compare the Chu first-order spherical mode and Wheeler cylindrical approximations to the simulated results [2, 3]. Relative changes in fractional bandwidth to changes in height may be directly obtained from the results shown.

The geometry of the square PIFA shown in Fig. 4.10, with infinite ground plane as a boundary condition, was used for all computations. The square form-factor ($W = L$) is fixed where the overall height is decreased from $h_{MAX}= \lambda/15$ to $h_{MIN} = \lambda/60$. The denominator of the electrical height shown as $h=\lambda/N$, where $N$ is varied from $15<N<60$. The center frequency for the models was $f_R = 1.0$ GHz. Adjustment of the capacitive-loading parameters and the probe position along the x-axis were required to resonate the ten models at $f_R=1.0$ GHz. The geometry is similar to the antenna chosen by Huynh [1] for a study of finite ground plane effects on PIFA performance with the addition of capacitive loading for miniaturization. Fig. 4.11 is the complex impedance response for the PIFA with height, $h= \lambda/35$ ~9mm. The radiation resistance $R_R=2.5\Omega$ at resonance ($f=1.0$ GHz).

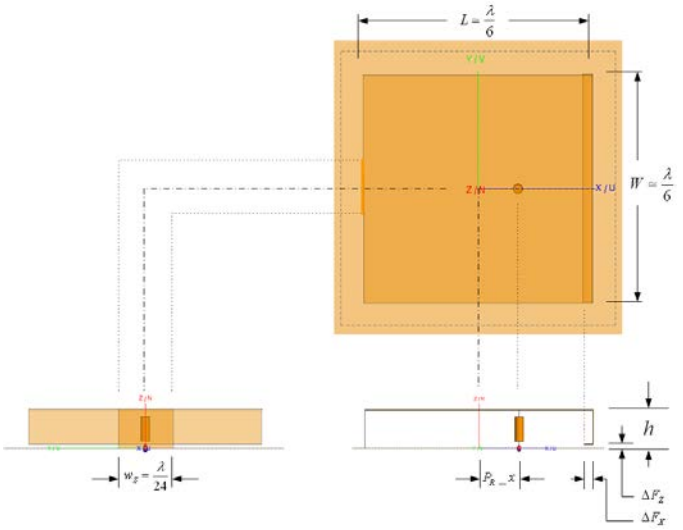

**Fig. 4.10. CADFEKO rendering of capacitive-load PIFA over an infinite ground plane. Tuning for resonance at $f_R$=1.0 GHz is achieved by movement of probe along x-axis (*Pr_x*) and adjustment of effective capacitive loading.**

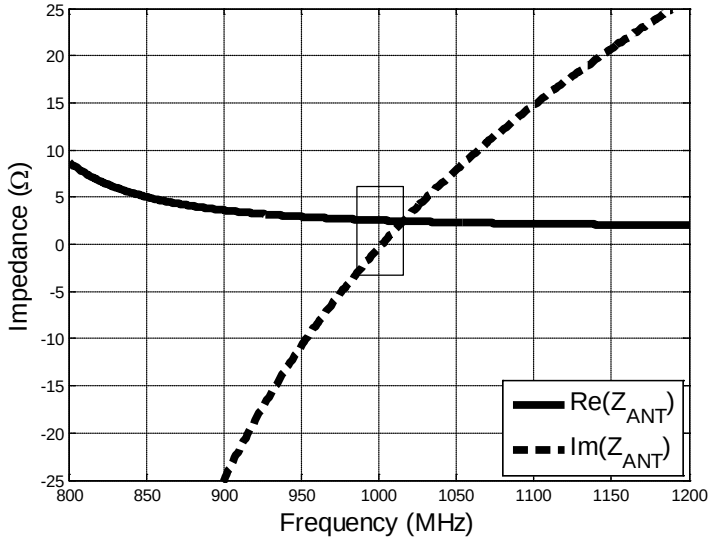


**Fig. 4.11. Calculated impedance response for PIFA response, *h=λ/35* tuned to resonance at $f_R$=1.0 GHz (see Fig. 4.10). The impedance response was calculated using FEKO. $R_R$ is the real part of the complex impedance at resonance and is the reference to calculate VSWR and half-power bandwidth response shown in Fig. 4.12.**

Fig. 4.12 compares the Return Loss and VSWR responses for $R_o=R_R=2.5\ \Omega$ to the $R_0=50\ \Omega$. The half-power bandwidth ($RL<3dB$, $VSWR<5.8$) and corresponding $Q_{HP}$ is computed and shown in Equations (6) and (7).

$$B_{HP} = \frac{f_U - f_L}{f_R} = \frac{(1.031 - 0.974)\,GHz}{1.002\,GHz} = 0.0569 \tag{6}$$

$$Q_{HP} \approx \frac{1}{B_{HP}} = 17.58 \tag{7}$$

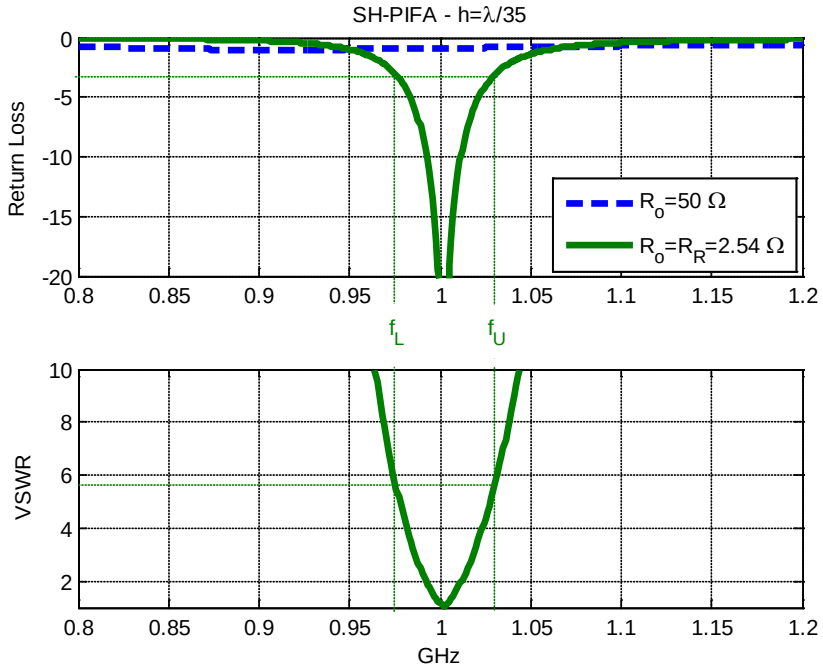


**Fig. 4.12. Return Loss and VSWR response shown in Fig. 4.10 for the PIFA with *h=λ/35*. The impedance response was calculated using FEKO. The antenna resistance ($R_R$) at resonance is determined from the simulation output and used the reference load to calculate VSWR.**

| $f_R$ [GHz] | $R_R$ [Ω] | $X_R$ [Ω] | $Q$ [ ] | $f_L$ [GHz] | $f_L$ [GHz] | $B_{HP}$ [%] | $Q_{HP}$ [ ] |
|---|---|---|---|---|---|---|---|
| 1.00 | 2.54 | 0.01 | 35.7 | 1.031 | 0.974 | 5.7 | 17.6 |

**Table 14. Resonance and Half-Power Bandwidth Tabulated Values for the PIFA shown in Fig. 4.10 with *h=λ /35*.**

The geometry of the structure shown in Fig. 4.13 leads to the calculation of the radiansphere

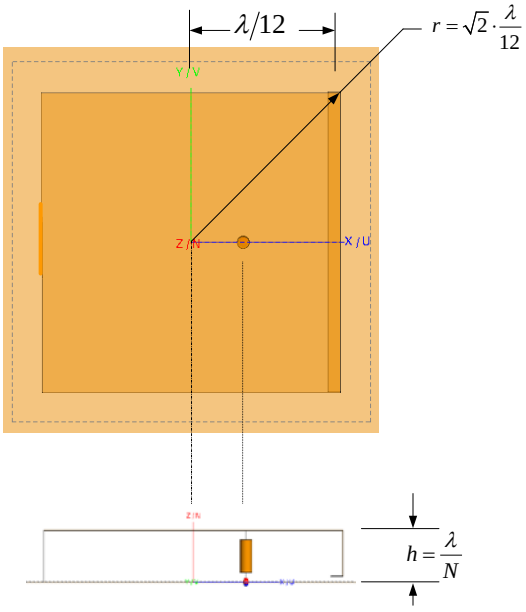


**Fig. 4.13. CADFEKO rendering of PIFA geometry with dimensions shown in units of wavelength.**

$$a = \sqrt{r^2 + h^2} = \lambda\sqrt{\frac{1}{72} + \frac{1}{N^2}} \approx \frac{\lambda}{6\sqrt{2}} \tag{8}$$

$$k\,a = \frac{2\pi}{\lambda} \cdot \frac{\lambda}{6\sqrt{2}} \approx 0.75 \tag{9}$$

The lowest-order approximation given by Chu [2] and introduced in Chapter 3

$$Q_{01} = \frac{1}{(ka)^3} \approx 2.4 \tag{10}$$

The approximation developed by Wheeler [3] is based upon a cylindrical volume.

$$Q_{CYL} = \left(\frac{6\pi}{k_s \cdot A \cdot h}\right) \cdot \left(\frac{\lambda}{2\pi}\right)^3 \tag{11}$$

The shape factor from Wheeler for the low-profile, square volume element may be approximated, $k_s \approx 1$ and $A = \lambda^2/36$.

$$Q_{CYL} = \left(\frac{27}{\pi^2}\right) \cdot N = 96 \tag{12}$$

For the highlighted case $N = 35 \rightarrow h = \lambda / N$ is referred to earlier with bandwidth and quality factor calculations based upon Fig. 4.13, the Wheeler approximation yields, $Q_{CYL} \approx 96$. The example shown is consistent with the observation by McLean, 'for values of *ka* near one (but still less than one) the expressions (from Chu and Wheeler) differ significantly. This range of electrical size is important in that a number of antenna designs fall into this range.' [4].

A straightforward and practical approximation for antenna quality factor is based upon an equivalent spherical volume approach. The physical volume of a rectangular (in this case) element is set equal to a spheroidal volume of radius $a_{EQ}$. The radius of the equivalent sphere is used in the Chu approximation to estimate *Q*.

$$V_{PHY} = \frac{4}{3}\pi \cdot a_{EQ}^3 \tag{13}$$

For the case shown in Figure 4.3.8, where $h = \frac{\lambda}{N} = \frac{\lambda}{35}$ ,

$$V_{PHY} = L \times W \times h = \frac{\lambda}{6} \times \frac{\lambda}{6} \times \frac{\lambda}{35} = \frac{\lambda^3}{1260} \tag{14}$$

The terms $ka_{EQ}$ and $Q_{EQ}$ are easily calculated to determine a very good estimate of the actual $Q \approx 36$.

$$ka_{EQ} = \frac{2\pi}{\lambda} \cdot \frac{\lambda}{17.4} \approx 0.36 \tag{15}$$

$$Q_{EQ} \approx \frac{1}{\left(ka_{EQ}\right)^3} = 21.3 \tag{16}$$

Table 15 lists the ten models created to illustrate the relationship between overall height and antenna quality factor, calculated using the impedance relationships developed by Yaghjian and Best ($Q_A$), in addition to the direct determination of the half-power VSWR bandwidth for a matched reference ($Q_{HP}$). Fig. 4.14 plots the calculated values of quality factors versus the theoretical minimum *Q*. The VSWR bandwidth is the loaded *Q* of the antenna with source described earlier, and $Q_A$ represents the unloaded *Q* of the independent antenna. $Q_A$ is calculated

directly from $|\partial Z/\partial\omega|$ and requires the numerical approximation of derivatives. The half-power calculation of $Q_{HP}$ validates the direct formula and does not require the numerical approximation of derivatives.

| $f_R = 1\,GHz$<br>$\lambda_R = 30\,cm$ | $N$ | $h = \frac{\lambda_R}{N}\,(cm)$ | $R_R$ ($\Omega$) | $Q_A$ ( ) | $Q_{HP}$ ( ) | $Q_{EQ}$ ( ) |
|---|---|---|---|---|---|---|
| 1 | 15 | 2.00 | 27.29 | 7.21 | 3.47 | 9.11 |
| 2 | 20 | 1.50 | 10.06 | 13.96 | 6.72 | 12.15 |
| 3 | 25 | 1.20 | 4.88 | 21.23 | 10.53 | 15.19 |
| 4 | 30 | 1.00 | 3.27 | 26.19 | 14.33 | 18.22 |
| 5 | 35 | 0.86 | 2.54 | 35.72 | 17.58 | 21.26 |
| 6 | 40 | 0.75 | 1.75 | 50.09 | 21.53 | 24.29 |
| 7 | 45 | 0.66 | 1.70 | 56.63 | 23.86 | 27.33 |
| 8 | 50 | 0.60 | 1.39 | 59.14 | 28.54 | 30.37 |
| 9 | 55 | 0.55 | 1.32 | 56.87 | 29.50 | 33.41 |
| 10 | 60 | 0.50 | 1.12 | 67.37 | 33.47 | 36.44 |

**Table 15. Quality-factor versus height for a lossless PIFA over an infinite ground plane (see Fig. 4.10). Impedance responses for the ten configurations were calculated using FEKO. The direct calculation based on Yaghjian Best and the half-power bandwidth methods differ by a factor of two.**

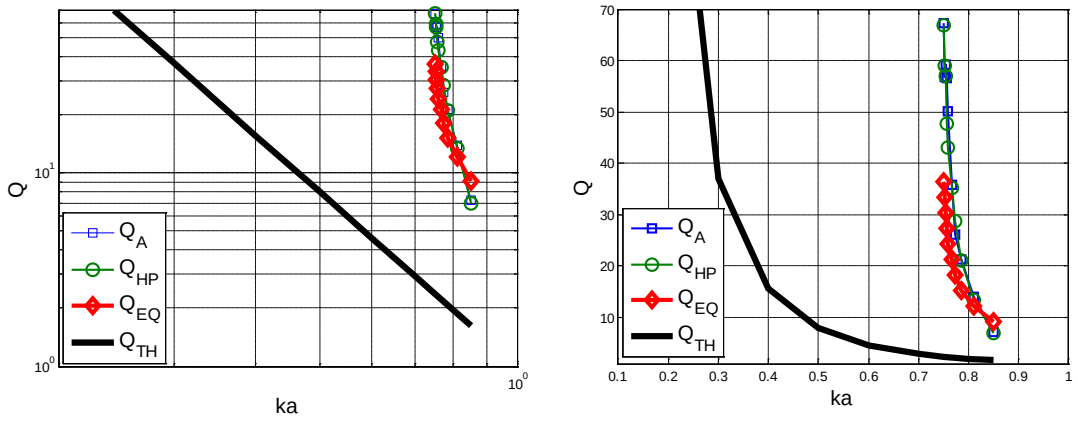


**Fig. 4.14. Calculated $Q_A$ values for the model (shown in Fig. 4.10) versus electrical size *ka*. The theoretical minimum, $Q_{TH}$ curve is shown in black.**

An additional step was taken to attach the minimum-height model to the handheld chassis introduced earlier to observe the overall performance. The width of the minimum-height PIFA was reduced to fit on the handheld fixture used previously, as shown in Fig. 4.15. The $E_\theta$ and $E_\Phi$ radiation patterns for the mobile terminal are shown in Fig. 4.16. The dimpling of the $E_\theta$ pattern on the edge side of the device is similar to the monopole case shown previously. The percent power mode distribution for the case indicates greater than 75% of the radiated power is retained in the $TM_{0N}$ modes.

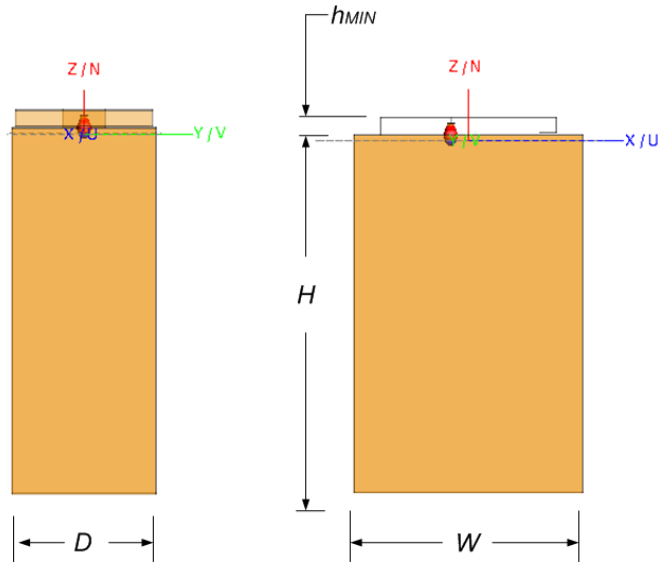


**Fig. 4.15. CADFEKO rendering of minimum height (*h=λ/60*), PIFA configured on handheld device. The dimensions of the chassis are approximately *H=10cm* tall, *W=6.5cm*, and *D=4cm*.**

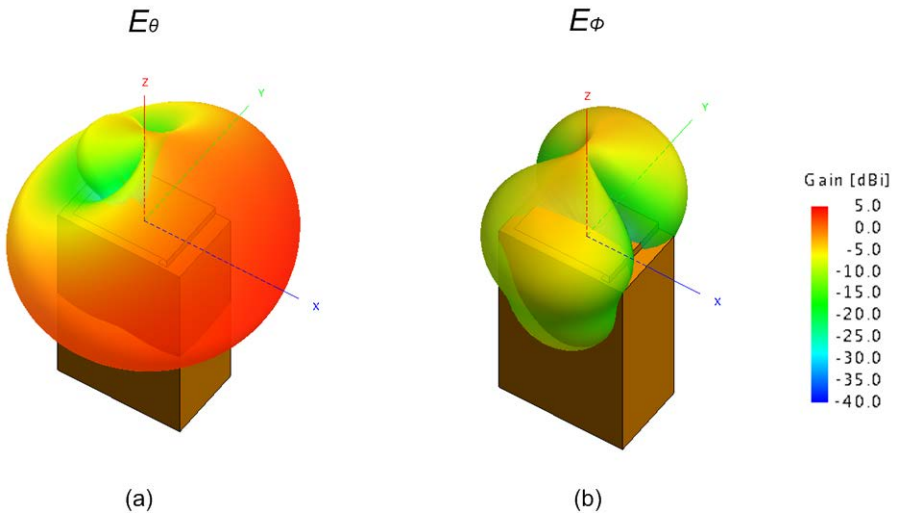


**Fig. 4.16. $E_\theta$ and $E_\Phi$ Radiation Patterns for minimum height for the minimum height PIFA, shown in Fig. 4.15, mounted on handheld structure. Far-field radiation patterns were calculated using FEKO.**

| | $TM_{mn}$ | | $TE_{mn}$ | |
|---|---|---|---|---|
| ***m*** | ***n=1*** | ***n=2*** | ***n=1*** | ***n=2*** |
| -1 | 2.5 | 0.4 | 9.3 | - |
| 0 | 65.8 | 8.9 | - | - |
| +1 | 2.5 | 0.4 | 9.3 | - |

**Table 16. Far-Field *TM* and *TE* mode Compositions for Minimum Height PIFA mounted on the Handheld Device (see Fig. 4.15). Far-field radiation patterns and corresponding mode decompositions were calculated using FEKO.**

Comparison of the conventional and the minimum height PIFA-integrated handheld geometries indicate an increase in the half-power bandwidth calculated quality factor from $8.7<Q_{HP}<33.5$. Changes in modal content are less significant with a slight increase in $TM_{0N}$ power for the minimum height PIFA configuration. For the case of the conventional PIFA mounted on a handheld, the $TM_{0N}$ percentage power was approximately 65% of the total power. The minimum height example shown in Table 4.3.6 indicates nearly 75% of the total radiated power is in the $TM_{0N}$ modes. The increase in $TM_{0N}$ power for the short PIFA is the result of a smaller contribution of radiation from the horizontal plate and a larger contribution of surface current radiation from the handheld chassis.

The following section reviews miniaturization techniques for antenna size reduction and their applications to the low-profile PIFA mounted on a portable device or handheld chassis.

### 4.3.2 Miniaturization - Single Resonant Antennas

Advances in microelectronics have led to significant size reduction in portable electronics and microprocessor computing. However, limitations in small antenna efficiency and bandwidth have precluded similar progress in the miniaturization of RF front-ends and antennas.

Wheeler noted the role of the volume occupied by a given antenna in determining its radiation power factor ($1/Q_{ANT}$) [3]. Efficient, small antennas utilize the maximum amount of volume defined by the circumscribing radius. Low-profile antennas are not volume-efficient but are best suited for certain mobile applications. A review of techniques for miniaturization for small, low-profile, single-resonant antennas are presented with results shown for the conventional PIFA introduced earlier.

Four practical techniques for miniaturization of small and low-profile antennas include: [5]

1. Lumped components - reactive matching
2. High contrast material loading
3. Meta-materials
4. Shape Optimization - bending, folding, meandering, slot-loading

Lower frequency systems, including amateur radio bands, may match high input reactances of small antennas with discrete or lumped elements. Better designs for cellular band systems, implement tuning reactances directly in the antenna structure. The gamma match characteristic utilized in the inverted-F antenna and the planar inverted-F antenna is an example narrowband matching at the antenna input.

High-contrast material loading, often referred to as a ‘holy grail’ for antenna design, has been pursued with the development of low-loss magneto-dielectric materials. The objective is to decrease the wave velocity through an antenna substrate or medium, where $c_o = 1/\sqrt{\mu\varepsilon}$ . A smooth transition or decrease could be achieved if balanced increases in both the permittivity and permeability were possible. Low-loss, high permittivity materials exist and are readily available, however, low-loss magnetic materials with commensurate values of relative permeability have yet to be created.

Engineered materials or meta-materials have periodic structure embedded in a relatively low-loss medium to synthesize a magnetic medium, typically used as a quasi PMC (perfectly

magnetic conducting) ground plane. Current meta-materials are still too lossy for antenna fabrication, and by nature of their periodic structures are bandwidth-limited.

Shape optimization for an air-backed or low-permittivity media is well-established in small antenna design. Disk-loaded or bent monopoles, meander lines, and slot-loading of planar structures increase the surface current path(s) on a given structure to lower the resonant frequency. Fig. 4.17 (a) and (b) illustrate the resulting longer surface current path due to the slot-loading of a PIFA element. The illustration also hints to the higher current density which generally increases the antenna quality factor.

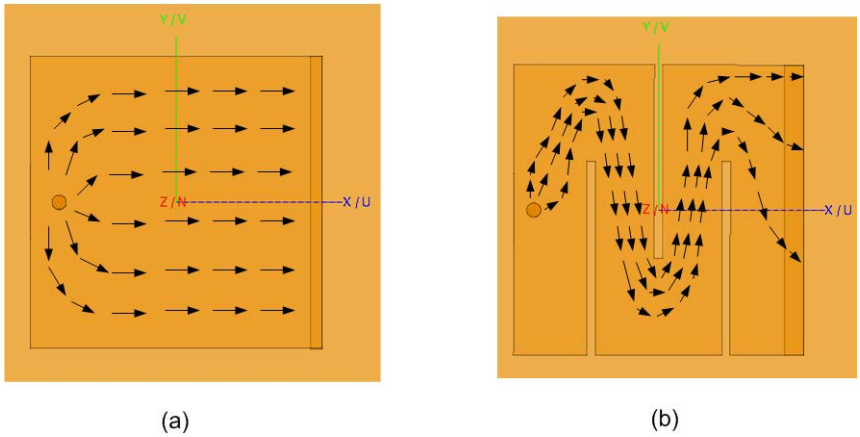


**Fig. 4.17. Representative illustration of slot-loading miniaturization technique. The resulting increase in surface current path length lowers resonant frequency and increases surface current density.**

Shape optimization also includes bending which is an ideal mechanical solution for the free end of the PIFA's top plate. Rolling the free end to create a parallel plate capacitance with the ground plane seen in Fig. 4.18 achieves miniaturization and improves the structural integrity of an antenna mounted on a mobile terminal. The free end of a conventional PIFA is an unsupported cantilever beam that may be easily deformed in an antenna-hostile environment outside the laboratory. A low-loss dielectric can be used as a substrate and bonded for extra strength.

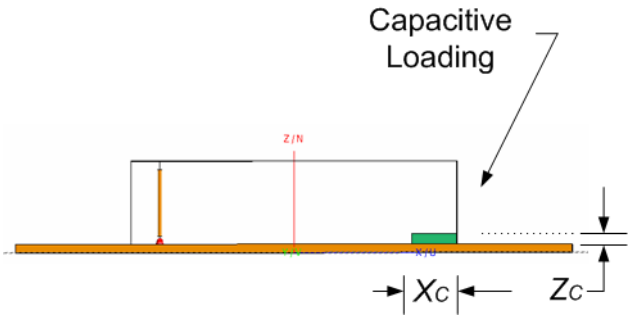


**Fig. 4.18. Side view CADFEKO model of PIFA with capacitive loading. The capacitive load is a low-loss, low-permittivity dielectric foam.**

The PIFA was scaled such that the original structure with no miniaturization had a resonant frequency of approximately $f_o = 1.5\ GHz$. Fig. 4.19 is an engineering perspective of the structure shown with the slot loading and capacitive feed for miniaturization. Table 17 lists the dimensions with the original $k_o a \approx 0.73$.

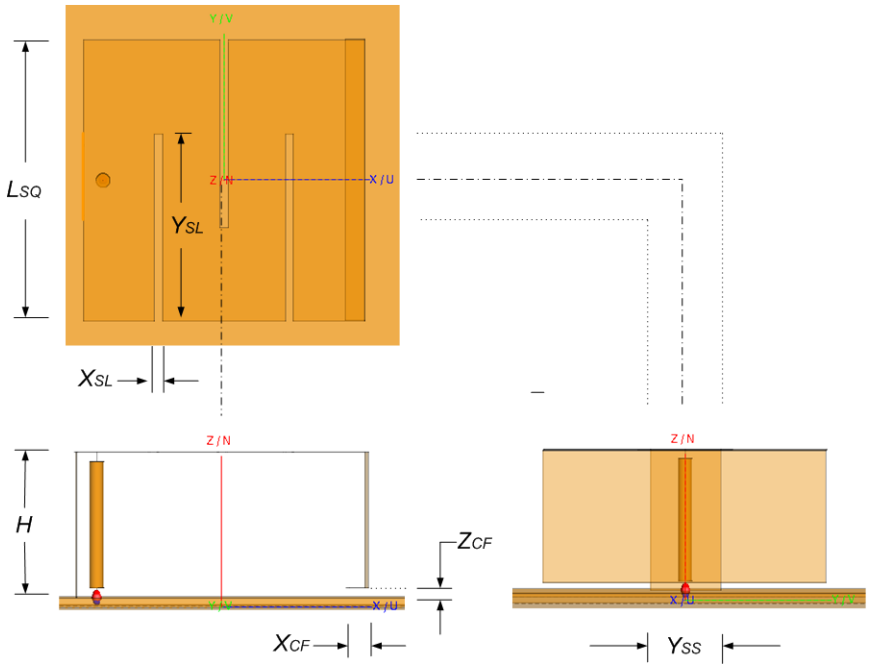


**Fig. 4.19. CADFEKO rendering of a conventional PIFA with capacitive-load and meandering for miniaturization.**

| $L_{SQ}$ [cm] | $H$ [cm] | $X_{SL}$ [mm] | $Y_{SL}$ [cm] | $X_{CF}$ [mm] | $Z_{CF}$ [mm] | $Y_{SS}$ [mm] | $k_o a$ [ ] |
|---|---|---|---|---|---|---|---|
| 2.62 | 1.31 | 1.0 | 1.75 | 1.75 | 1.0 | 6.5 | 0.73 |

**Table 17. Dimensions for conventional PIFA with capacitive-load and meandering for miniaturization shown in Fig. 4.19.**

Table 18 illustrates the decrease in frequency for the combination of miniaturization techniques with the corresponding increases in antenna quality factor. For this example, when the original PIFA is modified to include both slot-loading and capacitive loading the resonant frequency scales by a factor of *1/2*. The calculated Return Loss traces and corresponding changes in antenna quality factor are shown in Fig. 4.20 (a) and (b) respectively. Fig. 4.21 plots the Quality-Factor versus *ka* for the two miniaturization methods. The combinations are shown and plotted against the theoretical minimum.

| | | $f_R$ (GHz) | $ka$ ( ) | $R_{RAD}$ (Ω) | $X_R$ (Ω) | $Q_A$ ( ) | $Q_{HP}$ ( ) | $Q_{EQ}$ ( ) |
|---|---|---|---|---|---|---|---|---|
| 1 | *ORIG_FGP* | 1.536 | 0.73 | 36.8 | 0.9 | 14.1 | 6.74 | 17.28 |
| 2 | *MNDR_FGP* | 1.256 | 0.59 | 20.8 | 3.6 | 34.9 | 16.5 | 31.60 |
| 3 | *ORCL_FGP* | 1.02 | 0.49 | 10.0 | 1.6 | 65.2 | 28.3 | 59.00 |
| 4 | *MNCL_FGP* | 0.768 | 0.37 | 4.24 | 1.2 | 411.1 | 96.0 | 138.24 |

**Table 18. Calculated impedance and quality factor values for the four miniaturization configurations based upon the model shown in Fig. 4.19. Impedance response calculations were obtained using FEKO. The quality factor calculations compare the direct calculation based upon Yaghjian's relationship ($Q_A$), a half-power matched-load calculation ($Q_{HP}$), and an equivalent volume approximation ($Q_{EQ}$).**

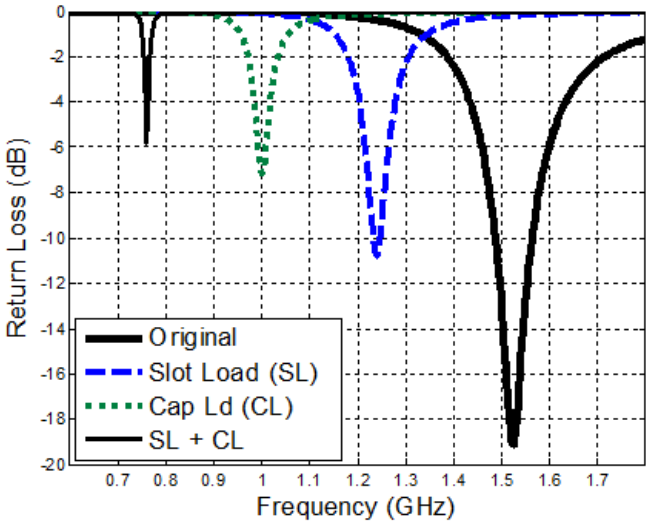


**Fig. 4.20. Return Loss responses for conventional PIFA shown in Fig. 4.19 for the miniaturization configurations. The original PIFA is scaled to approximately *f=1.5 GHz*. Two methods of miniaturization are shown slot-loading and capacitive-loading. Impedance responses shown were calculated using FEKO.**

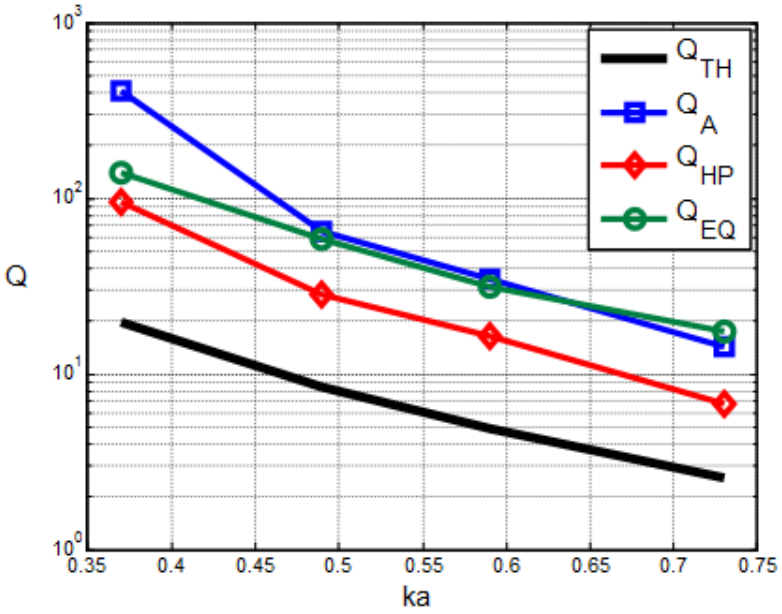


**Fig. 4.21. Quality Factor versus electrical size (*ka*) for PIFA miniaturization configurations shown in Fig. 4.19. The original PIFA is scaled to approximately *f=1.5 GHz*. Two methods of miniaturization shown are slot-loading and capacitive loading. $Q_{TH}$ represents the lowest order mode or fundamental limit. $Q_A$ represents the unloaded antenna *Q* and is calculated directly from the closed-form impedance relationship developed by Yaghjian and Best. $Q_{HP}$ represents the matched-load system Q and is determined from the half-power VSWR bandwidth with a matched reference. $Q_{EQ}$ is an approximation for antenna quality factor based upon an equivalent spherical volume.**

It is helpful to evaluate the Wheeler and Chu approximations at the minimum and maximum values of *ka*, where *0.37< ka<0.74*. The PIFA has overall dimensions, $L_{SQ} \approx \lambda/8$, and $h = \lambda/16$. The Chu and Wheeler approximations,

$$Q_{01} = \frac{1}{(ka)^3} \tag{17}$$

$$Q_{CYL} = \left(\frac{6\pi}{L_{SQ}^2 \cdot h}\right) \cdot \left(\frac{\lambda}{2\pi}\right)^3 = \left(\frac{3}{4\pi^2}\right)\left(\frac{\lambda}{L_{SQ}}\right)^2 \left(\frac{\lambda}{h}\right) \tag{18}$$

The Chu approximation for the range of *ka* shown varies $2.47 \leq Q_{01} \leq 19.8$. The Wheeler approximation based upon a cylindrical volume with the shape factor assumed to be unity. The range of $Q_{CYL}$ for the given geometry varies from $77.8 \leq Q_{CYL} \leq 622.4$.

The Wheeler approximation of the antenna quality factor is a more conservative estimate of the half-power bandwidth related quality factor developed by Yaghjian. Low-profile structures are bandwidth-limited and targets for bandwidth enhancement using electronics or even 'digitization' as Dr. Wheeler once described [8]. Active tuning for reconfigurable structures offers an alternative to the small wideband design. Such research was considered by Applied EM, Inc. as one component of the dissertation research.

Reconfigurable antennas are straightforward in concept and generate a great deal of excitement in the antenna research community. However, the engineering challenges present with the integration of DC-current driven electronics with surface current induced radiation are yet unresolved. In the next section we consider one such alternative.

## 4.4 Switch-Tuned PIFA

Active control of impedance tuning is made possible by active switch control of the inductive loop between the feed probe and the shorting bar. Adjustment of the shorting bar width controls equivalent inductance seen from the feed probe and has a limited impact on the surface current path on the top plate. When all switches are in the closed position, the probe inductance is at a maximum and the surface currents paths are the shortest. These conditions correspond to the

upper limit of the operating frequency range. All switches open leaves only the permanent shorting bar which minimizes the effective inductance and maximizes the surface current paths.

The front view of the switch-tuned PIFA shown in Fig. 4.22 illustrates the fixed shorting strap with three switch-controlled tuning straps. The switches were modeled as lossless metallic elements inserted/removed for the closed/open switch states. The quality of the overall impedance match decreased for the two outer switch states (000, 111). Fig. 4.23 plots the four principal tuned frequencies for the switch-tuned PIFA simulation model. The half-power bandwidth for the lossless PIFA simulation model measured from the minimum and maximum frequencies for $|RL| \geq 3dB$ about a center frequency, $f_c \approx 975\ MHz$, corresponds to approximately $B_{HP} \approx 10.3\%$.

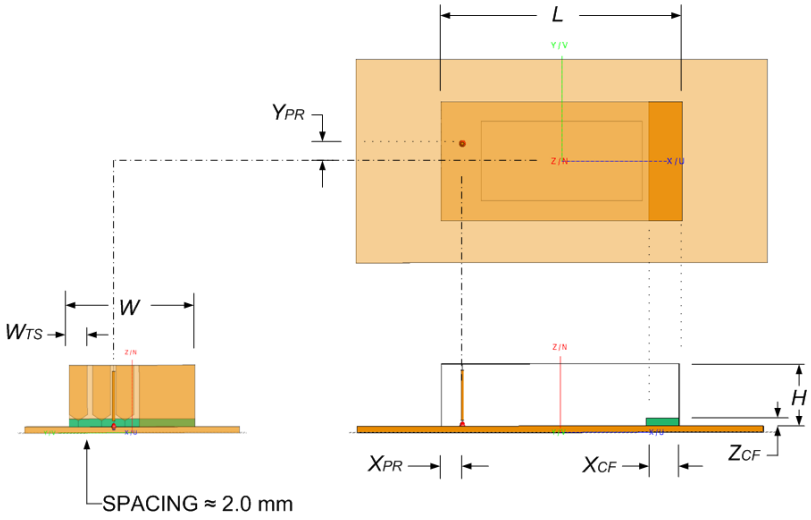


**Fig. 4.22. Engineering perspective of the switch-tuned PIFA model created in CADFEKO. The effective inductance created between the feed probe and vertical shorting bar is adjusted by short-circuit or open-circuit settings for the tuning 'straps' of width $W_{TS}$. The capacitive loading is achieved with the low-loss, low-dielectric separating the parallel plate section at the opposite end.**

| $W$ [cm] | $L$ [cm] | $H$ [cm] | $W_{TS}$ [cm] | $X_{PR}$ [cm] | $Y_{PR}$ [cm] | $X_{CF}$ [cm] | $Z_{CF}$ [cm] |
|---|---|---|---|---|---|---|---|
| 4.06 | 8.15 | 2.00 | 0.58 | 0.72 | 0.60 | 1.14 | 0.25 |

**Table 19. Dimensions of the active, switch-tuned PIFA model with capacitive-loading shown in Fig. 4.22.**

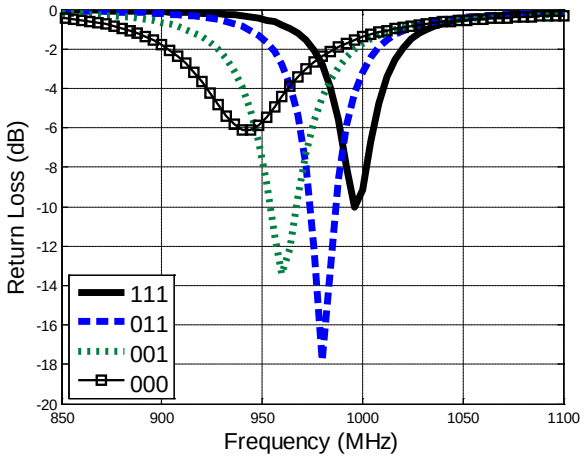


**Fig. 4.23. Return Loss responses for the active, switch-tuned PIFA shown in Fig. 4.22. Impedance response calculations were obtained using FEKO. The impedance responses shown for the four switched states are for the infinite ground plane boundary condition.**

Prototypes with low insertion loss RF pin diodes were with fabricated with biasing circuit and switch hardware shown in Fig. 4.24. The fabrication of the prototypes was part of the research collaboration with Applied EM, Inc. Fig. 4.25 shows the original test setup with a smaller circular ground plane that was conducive when the cables for the control box were shortened to reduce potential coupling.

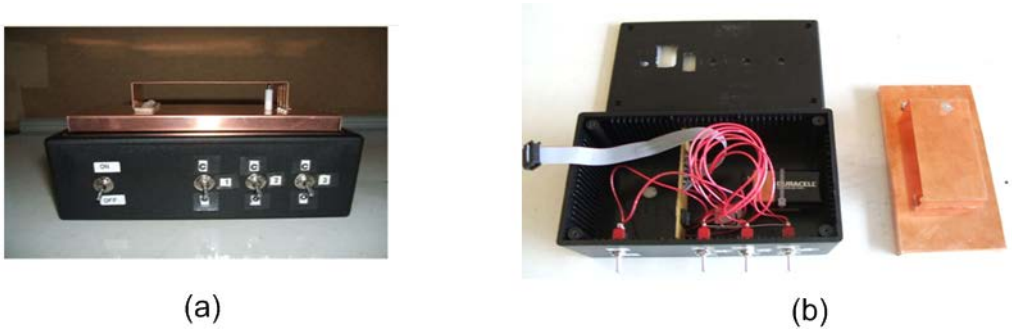


**Fig. 4.24. Switch-Tuned PIFA with control box and original length ribbon cable.**


**Fig. 4.25. VTAG original test setup of the switch-tuned PIFA shown in Fig. 4.24 mounted on a finite ground plane of diameter $D_{GP} \approx \lambda$.**

Fig. 4.26 is a rendering of the switch-tuned PIFA simulation model with a similarly-scaled circular ground plane. The switches were modeled as ideal where the actual switch was a wire, cylindrical element that was in place for 'closed' and removed for 'open'. Fig. 4.27 compares the simulated (a) return loss responses for the four switch states compared to the measured (b) return loss. Both loss and additional reactance accounted for the apparent better return-loss response, with increased operating and instantaneous bandwidths. The measured half-power bandwidths for the lossless FEKO simulation model (ideal) and the physical prototype-engineering development model (EDM) with active switch-tuning elements were $B_{HP}\big|_{ideal} \approx 11\%$ and $B_{HP}\big|_{EDM} \approx 38\%$ respectively, where the increase in bandwidth directly correlates with an increase in system loss and decrease in efficiency.

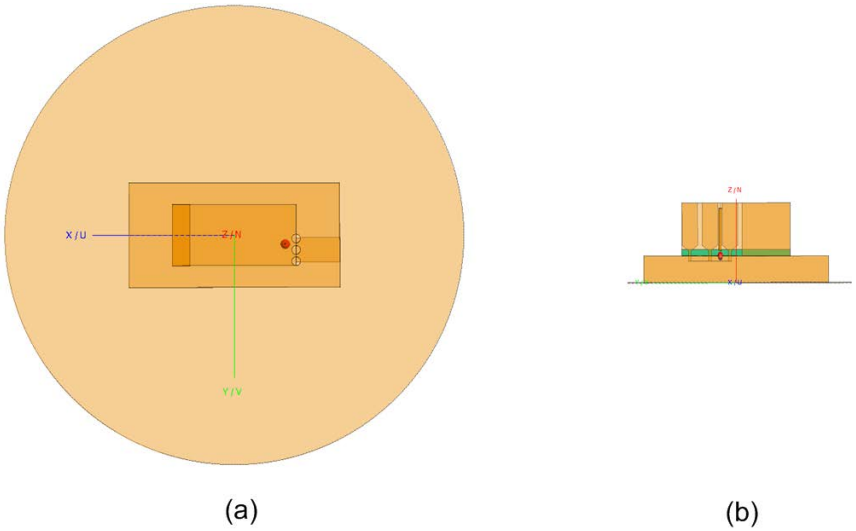


**Fig. 4.26. Top-view (a) and side-view (b) of active, switch-tuned PIFA CADFEKO model with circular finite ground plane and switch detail .**

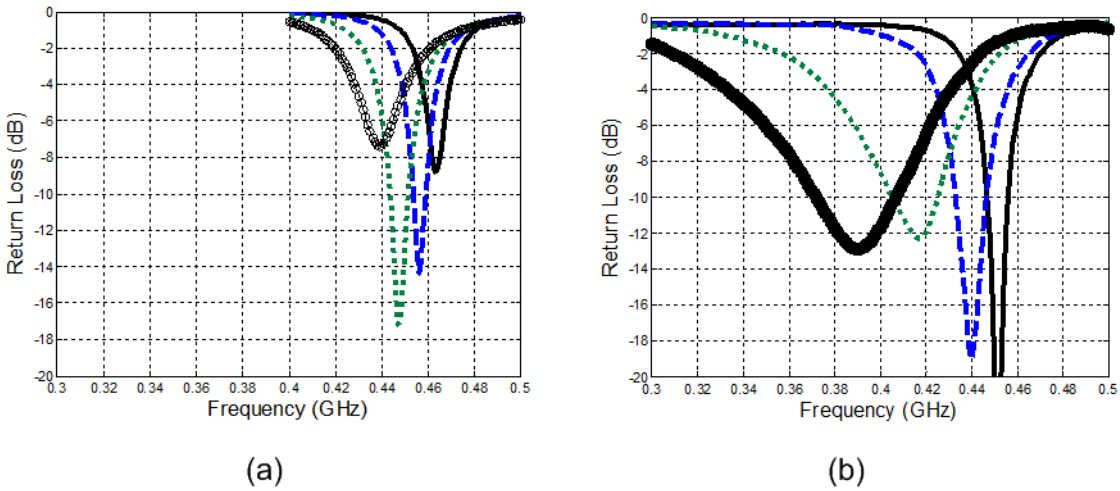


**Fig. 4.27. Ideal switch simulated Return Loss (a) and active-switch measured Return Loss responses. The test setup was modified with the switch control box mounted directly under the finite ground plane to reduce the ribbon cable length. Observed differences as a result of shortening the ribbon cable length were negligible.**

## 4.5 Conclusions

The sensitivities of a single-resonant monopole and the PIFA are minimal in terms of modal content and bandwidth. The examples were focused on antenna quality factor and modal content for handheld portable fixtures. Additional modal content accounts for the minimal dimpling and shaping of the $E_\theta$ radiation pattern. However, the dominant majority of the far-field radiated power can be represented as combinations of $TM_{01}$ and $TM_{02}$ spherical modes, the latter often to provide the cancellation of the fields below the ground plane.

Bandwidth and quality factor for a PIFA successively reduced in height was considered. A straightforward equivalent volume estimation method was introduced with good agreement to the results that would be expected from the fundamental-limit theory. Miniaturization, as a means to lower the single-resonant antenna operating frequency, was reviewed and followed with a relevant example.

Active impedance control was introduced using switched components as an alternative to passive antenna bandwidth design. A switch-tuned PIFA was simulated and compared to measured data. The contrast between the simulated and measured results indicates loss typical switch components and parasitic causing frequency shifts. The following chapter will investigate passive antennas with wideband characteristics as a solution to the inherent bandwidth limitations of single resonant low-profile antennas for wireless communications.

## 4.6 References


[1] M.C. Huynh, W.L. Stutzman, "Ground Plane Effects on Planar-Inverted-F Antenna (PIFA) Performance," IEE Proceedings on Microwaves, Antennas, and Propagation., vol. 150, no. 4, August 2003, pp.209-213.

[2] L.J. Chu, "Physical Limitations of Omni-Directional Antennas," Journal of Applied Physics, vol.19, Dec. 1948pp. 1163-1175.

[3] H.A. Wheeler, "Fundamental Limits of Small Antennas," *Proc. IRE*, vol. 35, Dec. 1947, pp. 1479-1484.

[4] J.S. McLean, "A Re-Examination of the Fundamental Limits on the Radiation Q of Electrically-Small Antennas," IEEE Transactions on Antennas and Propagation, vol. 44, no. 5, May 1996, pp.672-676.

[5] J.L. Volakis, C.C. Chen, and K. Fujimoto, *Small Antennas: Miniaturization Techniques and Applications,* New York: McGraw-Hill, 2010

[6] A.D. Yaghjian, S.R. Best, "Impedance, Bandwidth, and Q of Antennas," IEEE Transactions on Antennas and Propagation, vol 53, no. 4, April 2005, pp.1298-1324.

[7] H.A. Wheeler, "The Radiansphere Around a Small Antenna," Proc. IRE, vol. 47, 1959, pp. 1325-1331.

[8] H.A. Wheeler, "Antenna Topics in My Experience," IEEE Transactions on Antennas and Propagation, vol. AP-33, no. 2, February 1985, pp. 144-151.

# 5 CHAPTER - Wideband ESA Models

## 5.1 Introduction

The previous chapter investigated the single-resonant PIFA in several configurations to characterize the performance in practical settings. Low-profile, self-resonant impedance properties, in addition to a predominately omnidirectional radiation pattern, are examples of their attributes. The fundamental disadvantage of a low-profile PIFA ($h<\lambda/15$) is the antenna is typically band-limited with 2:1 VSWR bandwidths of less than five percent.

Electronic switch-tuning control of the PIFA was also investigated as a means to enhance the narrow instantaneous bandwidth and improve the margin or operating bandwidth of the device. The concept and simulation of a PIFA prototype with ideal switching characteristics is straightforward, however experience has shown the validation of the simulated data with measured results is elusive. Loss mechanisms, additional surface current paths, and unintended reactances due to the presence of physical switches are examples challenges preventing the transition of reconfigurable small antennas to the consumer market.

Passive, wideband electrically-small antennas may provide a better solution to create a margin or operating bandwidth for a mobile terminal in an unknown environment. Most wideband electrically-small antennas are volume-centric, utilizing the volume within the radiansphere. Additional structures coupling different surface current paths broaden the antennas band of efficient radiation.

Several of the antennas presented in the chapter are in the upper limit of the $ka<1$ bound for electrically-small antennas (ESAs). The designs include frequency-dependent reactances and/or current paths integrated directly in the radiating structure without the addition of external tuning elements. Bandwidth enhancement is made possible with closely spaced double-tuning(s) or multiple resonances. ESAs defined by the lower bound of $ka<0.5$ typically are not self-resonant and require external matching networks.

The sensitivity of the double-tuned antenna properties to variations in the near-field or integration to a generic handset model is considered. The modal properties of several examples are presented in an attempt to evaluate different classes of wideband ESAs for portable device

applications. A quantitative investigation of frequency-dependent mode spectra and variations in finite ground plane properties may offer some insight to the nature of self-resonant wideband antenna design.

A spherically-shaped, axially-symmetric spiral with ideal omnidirectional (in azimuth) $TM_{01}$ modal characterization is introduced. One volumetric, monopole-class wideband electrically-small antennas that is suitable for limited portable applications are also considered. Two low-profile, non-monopole wideband antennas are also chosen as examples to compare with the earlier examples.

## 5.2 Multi-resonant Spiral

The spherically-shaped multi-resonant spiral shown in Fig. 5.1 is comprised of six axially-symmetric arms similar to the structure investigated by Stuart, Best, and Yaghjian [1], scaled to *f=1.0 GHz* and fed with one voltage source. Surface currents are induced on the remaining arms via capacitive coupling.

A tradeoff for the structural symmetry and simplicity is the absence of structural tuning. The antenna reactance is tuned to zero at the target frequency with a *20 nH* inductance. The normalized impedance (Smith Chart) and VSWR responses for two, four, six and eight arm geometries are shown in Fig. 5.2 (a) and (b) respectively.

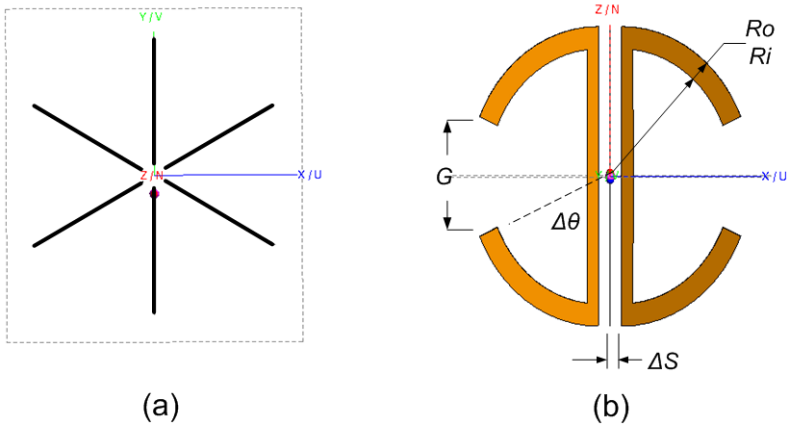


**Fig. 5.1. Engineering Perspectives shown of the Stuart-Best multi-resonant spiral generated in CADFEKO. The top-view (a) and side-view (b) of show overall design parameters and the location of the source excitation. A discrete inductance of *20 nH* was required at the feed to achieve resonance.**

| *Ro* [cm] | *Ri* [cm] | $\Delta\theta$ [deg] | *G* [cm] | $\Delta S$ [mm] | $X_{SER}$ [ nH ] | *ka* [ ] |
|---|---|---|---|---|---|---|
| 2.81 | 2.37 | 55.0 | 2.34 | 2.6 | 20.0 | 0.61 |

**Table 20. Dimensions of the Stuart-Best double resonant spiral antenna geometry shown in Fig. 5.1.**

Fig. 5.2 (a) and (b) show the double resonance due to each arm-pairs added to the structure. Coupling with the additional arms pairs decreases the first resonance, but the geometry of the arm ($\Delta\theta$, and *G)* establishes the first resonance. The second resonance is controlled by the capacitance-coupling to the parasitic arm-pairs. There are several natural modes of oscillation. For the case of the low-*Q* ($TM_{01}$) electric-dipole mode, all six arms oscillate in phase.

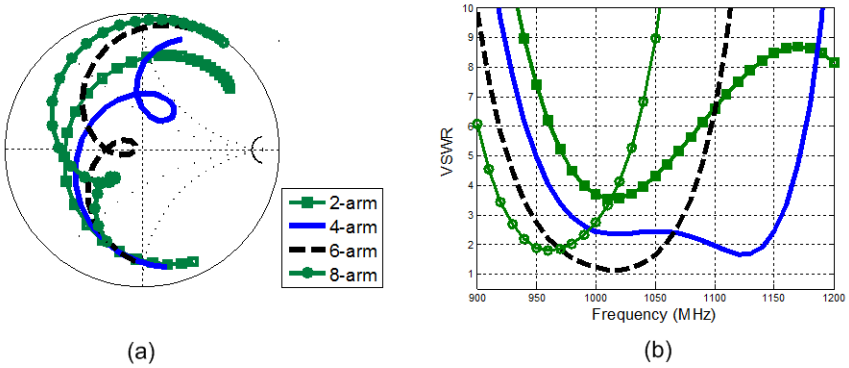


**Fig. 5.2. Calculated Smith Chart (a) and VSWR (b) responses for double-resonant spiral comprised of 2, 4, 6, and 8 arms. The geometry is based upon the model shown in Fig. 5.1. Impedance calculations were obtained using FEKO. The four-arm geometry has wider spaced resonances for potentially greater bandwidth. The resonant frequency is higher which also increases the effective *ka* value.**

Fig. 5.3 includes an isometric view of the multi-resonant spiral (a) and the resulting complex impedance response with parallel and series resonance points marked $f_1$ and $f_2$ respectively. A voltage source excitation was integrated to one of the arms as shown. The corresponding increase in matched-load half-power bandwidth is shown in Fig. 5.4.

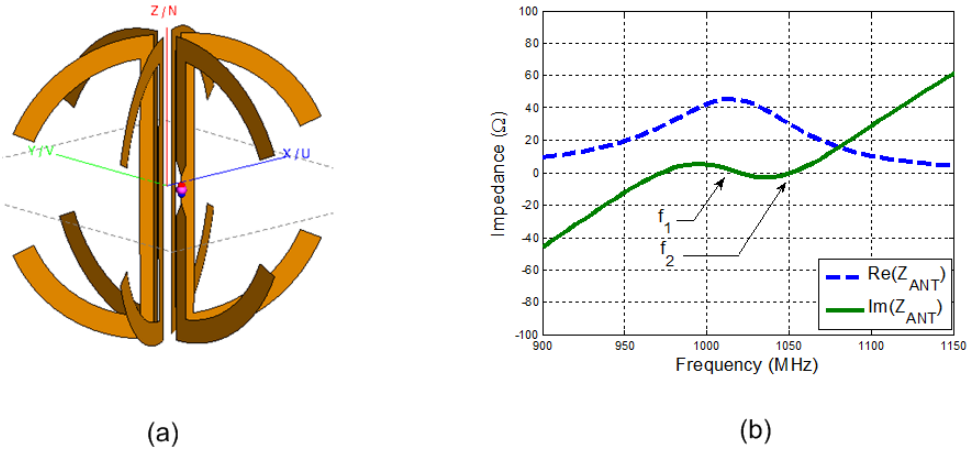


**Fig. 5.3. Multi-resonant spiral (a) geometry (see Fig. 5.1) and (b) complex impedance response. Impedance calculations were obtained using FEKO.**

For self-resonant structures, multiple (and increasing) values of $k_i a$ are the result of frequency-dependent surface current paths. Separate surface current distributions contribute to the total radiated power and near-field reactive energy within the bandwidth $B_i$. The frequency dependent current paths and corresponding fields generated may be represented with additional *TE* and *TM* spherical radiation modes.

For example, electrically-small wideband antenna design is achieved with a combination of two or more closely spaced resonant frequencies. Coupling between $f_1$ and $f_2$ increases the overall impedance bandwidth.

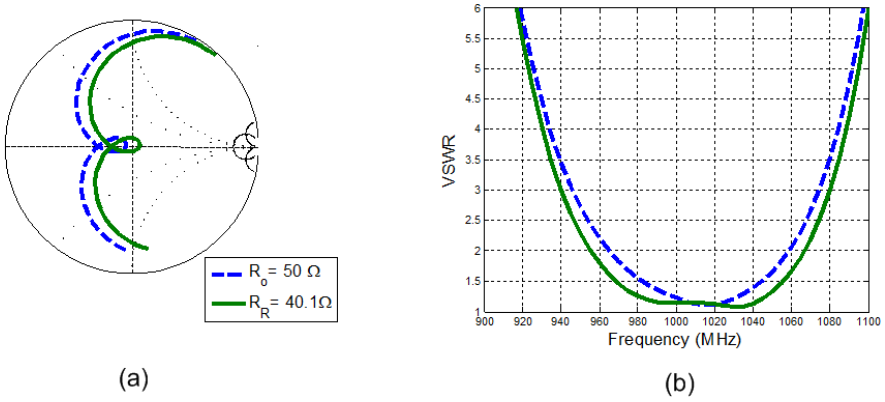


**Fig. 5.4. Resonance-tuned impedance responses and VSWR responses for the multi-resonant spiral antenna example shown in Fig. 5.1. Impedance calculations were obtained using FEKO.**

The bandwidth enhancement is explained by the introduction of additional mode(s) and the resulting distribution of radiated power and near-field energy into the corresponding *TE* and *TM* components. From an engineering perspective, if the second antenna in the hypothetical communication link is not similar (identical), the power radiated from the additional mode(s) of the transmit antenna is potentially wasted; antenna efficiency decreases at a cost of bandwidth enhancement.

Fig. 5.5 (a) and (b) are renderings of the $E_\theta$ and $E_\Phi$ radiation patterns for the multi-resonant spiral antenna. The feed location accounts for the slight asymmetry seen in the $E_\theta$ pattern (a). Table 5.2.1 also indicates more than 99% of the radiated power may be represented by the ideal $TM_{01}$ radiation mode. Cross-polarization represented by the $E_\Phi$ radiation pattern shown in Figure 5.2.4 (b) is more than 20 dB below the peak $E_\theta$ values.

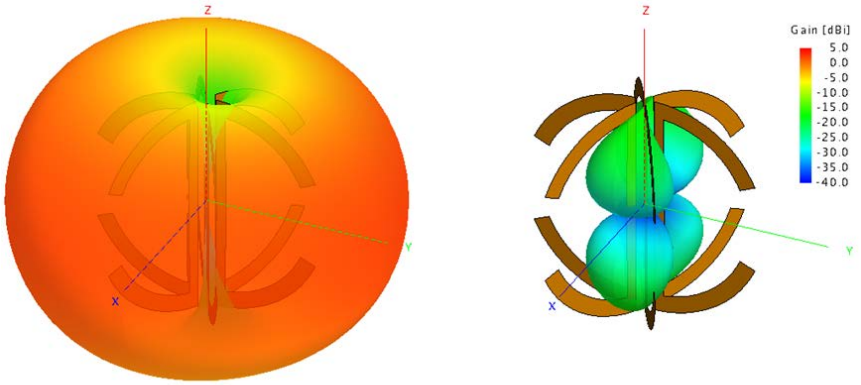


**Fig. 5.5. Three-Dimensional $E_\theta$ and $E_\Phi$ radiation patterns for the multi-resonant spiral antenna example shown in Fig. 5.1. Far-field radiation patterns were calculated using FEKO.**

| ***m=0*** | ***n=1*** | ***n=2*** | ***n=3*** | ***n=4*** | ***n=5*** |
|---|---|---|---|---|---|
| $TM_{0n}$ | 99.5 | - | - | - | - |
| $TE_{0n}$ | - | - | - | - | - |

**Table 21. Far-Field *TM* and *TE* mode Compositions for multi-resonant spiral antenna. Far-field radiation patterns and corresponding mode decompositions were obtained using FEKO.**

The multi-resonant spiral element generates a near ideal $TM_{01}$ omnidirectional pattern and may be used for comparisons to more practical examples in the following sections. The addition of multiple arms produces a coupled resonator effect, providing a wider bandwidth similar to coupled resonator circuits.

## 5.3 Ravipati Antenna

The Ravipati antenna is representative of several small, wideband antennas utilizing internal frequency-dependent reactances to achieve double-tuning(s) and multiple resonances. Dr. Best cited the Ravipati antenna which is physically similar to the popular Goubau antenna [9]. The author's interest in the Ravipati design is in part due to having the privilege of briefly working for Dr. Ravipati at Applied EM, Inc.

The enclosed model shown in Fig. 5.6 was reproduced from the illustration cited by Best [2]. Table 22 lists the dimensions for the model shown in Fig. 5.6. The impedance response plots shown in Fig. 5.7 indicate the double-tuned, multi-resonant characteristic of a wideband ESA design. Two tuning bars and a partial cylinder interact with frequency dependent coupling to the disk-loaded cone.

The Ravipati antenna is slightly larger than the familiar Goubau antenna. The multiple-tuning resonances seen on the Smith Chart in Fig. 5.7 are important characteristics of the Ravipati antenna. The Ravipati antenna was introduced earlier with the impact of each tuning circuit (shorting bars + partial cylinder) added to the central disk-loaded cone. The two shorting bars couple with the disk-loaded cone to set the lower resonance. The partial cylinder sleeve implements a higher second resonance. Careful design couples the two tuning circuits to create a second resonance that establishes a broad-band multi-resonant small antenna.

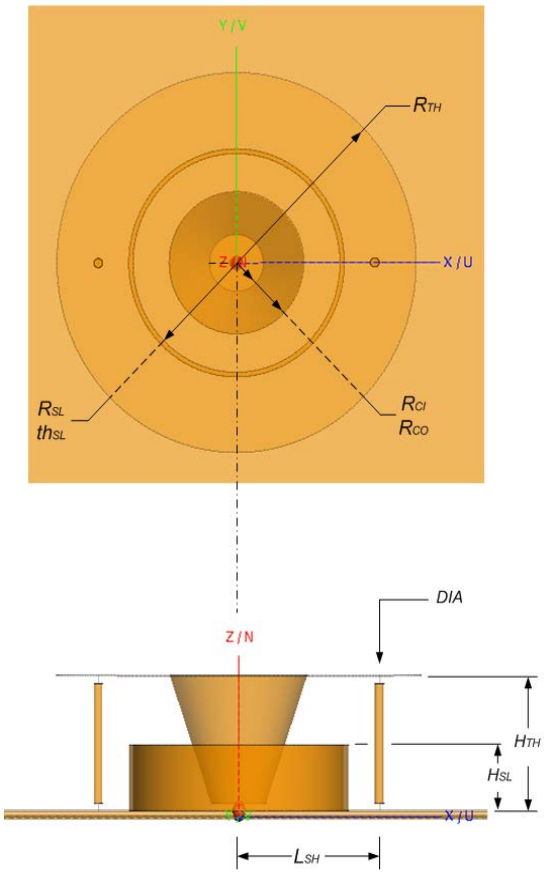


**Fig. 5.6. CADFEKO geometry of Ravipati antenna. The structure is built upon a disk-loaded cone with shorting-bars and a partial cylinder to increase bandwidth via multiple double-tuning mechanisms.**

| $R_{SL}$ [cm] | $th_{SL}$ [mm] | $R_{CI}$ [cm] | $R_{CO}$ [cm] | $R_{TH}$ [cm] | $L_{SH}$ [cm] | $DIA$ [mm] | $H_{SL}$ [cm] | $H_{TH}$ [cm] |
|---|---|---|---|---|---|---|---|---|
| 2.35 | 1.0 | 0.60 | 1.47 | 3.90 | 3.00 | 2.00 | 1.33 | 2.73 |

**Table 22. Dimensions of the CADFEKO geometry of the Ravipati antenna shown in Fig. 5.6.**

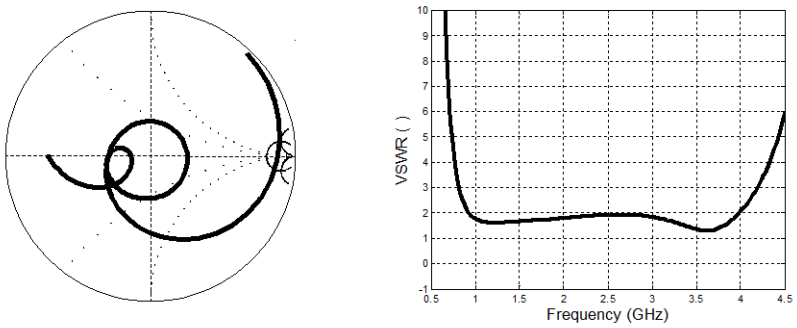


**Fig. 5.7. Simulated input impedance response for the Ravipati wideband antenna with double-tuning structures. Impedance calculations were obtained using FEKO.**

The far-field $E_\theta$ and $E_\theta$ Directivity Patterns of the Ravipati antenna on a relatively large finite ground plane are shown in Fig. 5.8 (a) and (b). All radiated power is represented by $TM_{0N}$ modes.

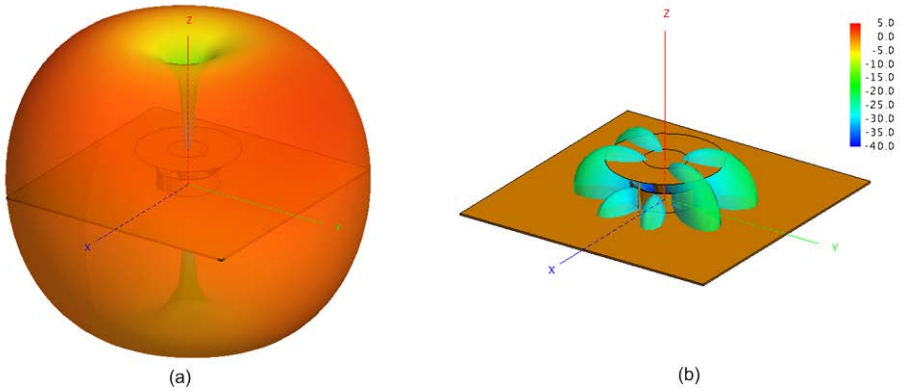


**Fig. 5.8. $E_\theta$ and $E_\phi$ Directivity Patterns of the Ravipati antenna (shown in Fig. 5.6) mounted on a finite ground plane $S_{GP}=0.4\lambda$ at $f=1.0$ GHz. Far-field radiation pattern calculations were obtained using FEKO.**

| *m=0* | *n=1* | *n=2* | *n=3* | *n=4* | *n=5* |
|---|---|---|---|---|---|
| $TM_{0n}$ | 69.2 | 30.4 | - | - | - |
| $TE_{0n}$ | - | - | - | - | - |

**Table 23. Far-Field *TM* and *TE* mode Compositions for Ravipati WB Antenna at *f=1.0 GHz*. Far-field radiation pattern calculations and corresponding mode decompositions were obtained using FEKO. Relative power percentages *Pmn<0.5%* were omitted from the table for clarity.**

The Ravipati antenna integrates two double-tuning circuits in the volume enclosed by the radiansphere. The low frequency range is established with the coupling of the tuning bars to the disk-loaded cone. A second high-frequency resonance is created with the partial cylinder interacting not only with the narrow diameter section of the cone, but coupling with the low frequency tuning bars enhances the overall bandwidth of the structure.

The use of the volume to initiate low-frequency radiation with shorting bars, and to extend high-frequency radiation with the partial cylinder, is different than the Stuart-Best multi-resonant spiral approach of simplicity (and elegance). The Ravipati is similar to other wide impedance bandwidth volume-centric designs near the uppermost limit of the definition of electrically-small. The Ravipati antenna is perhaps larger and taller than other candidates, but the impressive bandwidth response and stable modal characteristics would lead to a practical bandwidth/size design tradeoff for any antenna engineer to consider.

The Ravipati antenna is similar to other volume-centric antennas that efficiently utilize the volume circumscribed by the radiansphere. Double tuning and capacitive coupling to additional structures are effective techniques to create passive wideband monopole class antennas. Radiated power is predominately $TM_{0N}$. The next section will investigate modal compositions of the Ravipati antenna attached to small and large ground planes.

Fig. 5.9 is a rendering of the Ravipati antenna scaled to $ka \approx 1$, where $a \approx 5cm$ at a resonant frequency of $f = 1.0\ GHz$. The structure is similar to several wideband small antennas that begin with a central cone and implement double-tuning structures. The Ravipati adds low-frequency shorting bars and a high frequency partial cylinder for bandwidth enhancement.

Spherical Mode Decompositions of the wideband antenna to different ground planes offers insight. Fig. 5.10 illustrates three-dimensional plots of z-axis oriented $TM_{0N}$ modes for $N=[1,2,3,4]$. The nulls seen in the higher order modes shown are typically present in finite ground plane geometries and shape the $E_\theta$ patter in the shadow region below the ground plane.

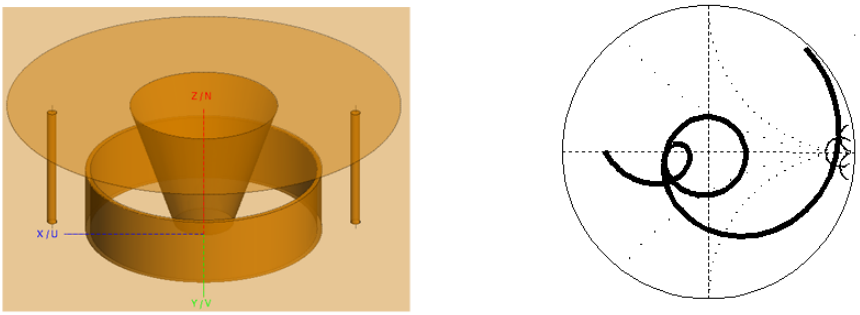


**Fig. 5.9. CADFEKO rendering of the (a) Ravipati antenna shown in Fig. 5.6 with the calculated Smith chart impedance response (b). The impedance response was calculated using FEKO.**

The $TM_{0N}$ mode components shown in Fig. 5.10 help visualize the stem-plot representations of the following example illustration the changes in modal content for low and high frequency operations of the Ravipati antenna on different ground planes.

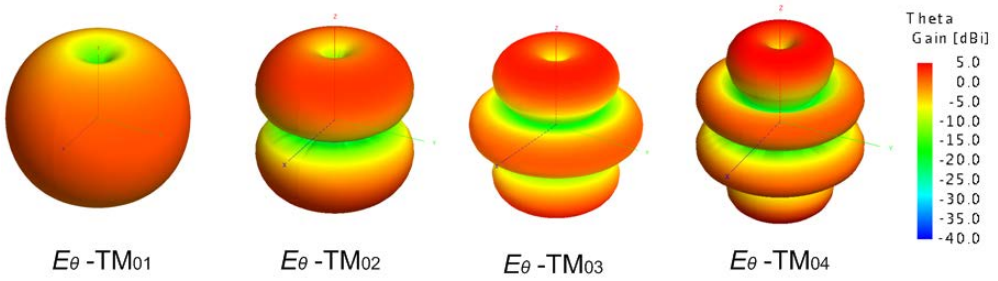


**Fig. 5.10. $E_\theta$ mode components shown for $TM_{0N}$. The four far-field patterns are calculated in FEKO for independent $TM_{0N}$ source excitations.**

Fig. 5.11 illustrates the $TM_{0N}$ mode distributions for the Ravipati antenna at *f=1.0 GHz* and *f=2.0 GHz* respectively. Representative of other similar wideband ESAs, at the low frequency (*f=1.0 GHz*) the Ravipati antenna is radiating at a $TM_{01}$ dipole. The small finite ground plane is enclosed by the radiansphere, except for the corners which result in a very small amount of $TM_{02}$ percent power. At the higher frequency, the ground plane essentially doubles and the $TM_{02}$ component becomes comparable to the $TM_{02}$ power radiated into the far-field.

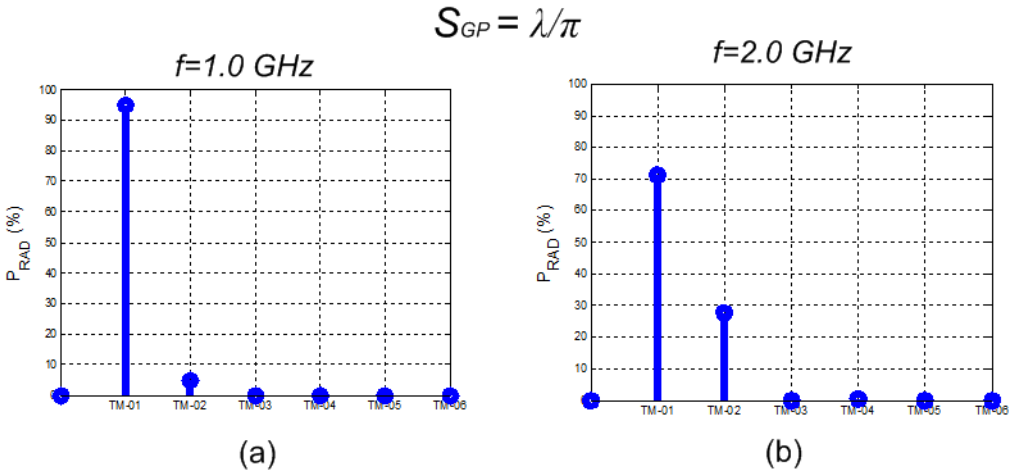


**Fig. 5.11. Low and High Frequency *TM* Percent Power Mode Distributions for Ravipati Antenna on Small Finite Ground Plane – $S_{GP}=2a$. Far-field mode decompositions were obtained using FEKO.**

Far-field mode distributions seen on Fig. 5.12 (a) and (b) are remain constant for the Ravipati antenna at both frequencies. The monopole structure is attached to the center of the finite ground plane, where image currents contribute to the far-field radiation and resulting mode distributions.

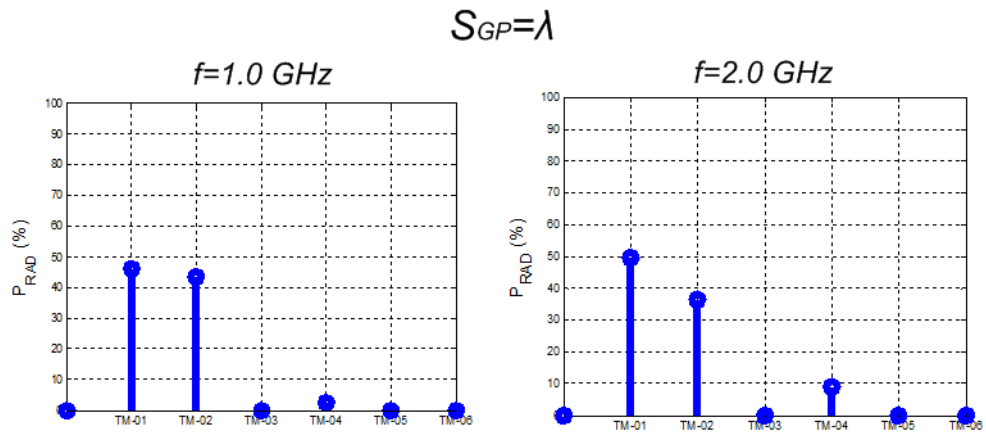


**Fig. 5.12 Low and High Frequency TM Percent Power Mode Distributions for Ravipati Antenna on Finite Ground Plane – $S_{GP}=\lambda$. Far-field mode decompositions were obtained using FEKO.**

The Ravipati antenna, scaled to *ka=1*, is at the uppermost limit of an electrically-small antenna. Similar to other wideband ESAs, the Ravipati is perhaps larger and taller that other candidates, but the very attractive bandwidth and stable modal characteristics would lead to a practical bandwidth/size design trade-off for consideration.

The next example is a very low-profile antenna with an attractive multi-resonant bandwidth characteristic. The wideband antenna was developed at Virginia Tech and will find multiple commercial applications, however mode decomposition will illuminate very different radiation properties from the monopole-class antennas shown previously. Sensitivity to device integration and resulting variations in the near-field will also be demonstrated.

## 5.4 Wideband Compact J-Pole Antenna

The wideband compact J-pole antenna introduced was developed by M.C. Huynh who is an alumnus of the Virginia Tech Antenna Group [3]. A United States patent (#6,795,028) was awarded for the low-profile wideband antenna introduced by the Virginia Tech Antenna Group. The antenna is similar in appearance to the planar inverted-F antenna (PIFA), where the wideband compact J-pole Antenna (WC J-pole) utilizes a capacitive feed and the small ground plane is designed to participate in the radiation. The 'ground plane' for the WC J-pole antenna is the principal radiator and very different than the PIFA, through the examples shown previously, has minimal ground plane requirements.

Fig. 5.13 is illustration of the geometry of the compact J-pole antenna. The model was scaled from the low S-band ($f \approx 2.1GHz$) in [3] to $f = 1.0\ GHz$ for comparison to the other antennas presented. Huynh describes in detail in [3], the antenna characteristics can best be described as a planar, capacitive-feed, J-pole antenna, which is essentially an end-fed half-wave planar dipole.

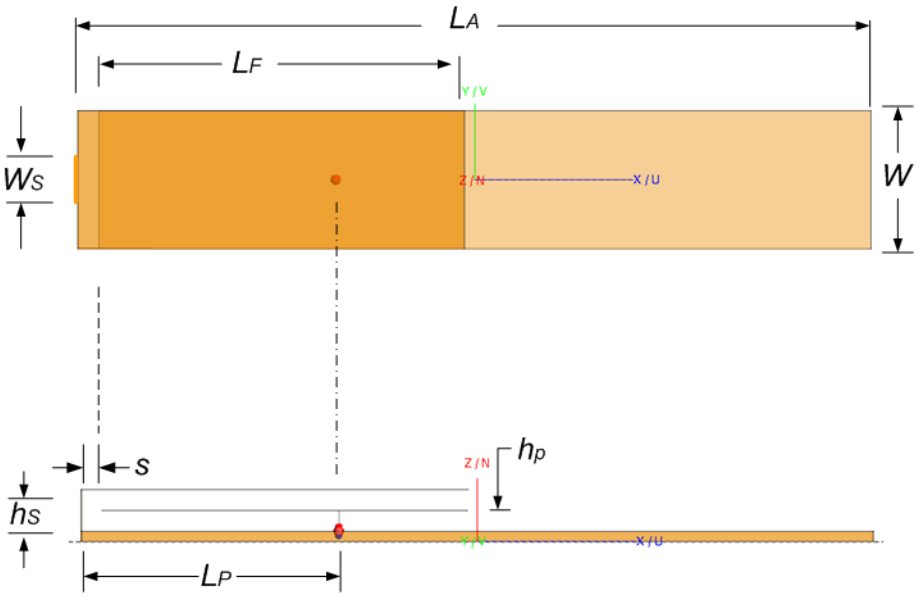


**Fig. 5.13. CADFEKO rendering of wideband compact (WC) J-pole antenna.**

| $W_S$ [mm] | $L_F$ [cm] | $L_A$ [cm] | $W$ [cm] | $h_S$ [mm] | $s$ [mm] | $L_P$ [cm] | $h_P$ [mm] |
|---|---|---|---|---|---|---|---|
| 7.3 | 6.11 | 12.54 | 2.2 | 6.6 | 3.3 | 4.0 | 3.3 |

**Table 24. Dimensions for the air-backed WC J-pole antenna shown in Fig. 5.13**

The multi-resonant characteristic of the WC J-pole antenna is the result of two structural features. The width of the shorting plate, $W_S$ influences the effective surface current path length and lower resonant frequency in the multi-resonant design. The capacitive feed compensates for the inherent self-inductance of a probe-feed structure. Fig. 5.14 illustrates the double-tuned impedance characteristic as a result of the two design techniques.

Fig. 5.15 (a) and (b) are three-dimensional renderings of the $E_\theta$ and $E_\phi$ directivities for the wideband compact J-pole antenna. The Far-Field *TM* and *TE* mode compositions for the antenna shown are presented in Table 25 and indicate a negligible amount of power is represented by the $TM_{0N}$ vertically-polarized omnidirectional modes. Nearly all of the power is contained in the $TM_{11}$ modes. The result distributes comparable percentages of vertically and horizontally polarized power.

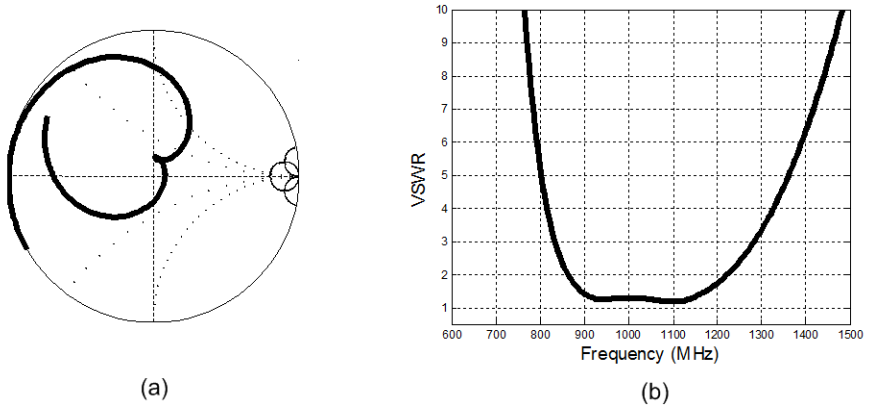


**Fig. 5.14. Simulated input impedance (a) and VSWR Response (b) for wideband compact J-pole antenna shown in Fig. 5.13. The impedance response was calculated using FEKO.**

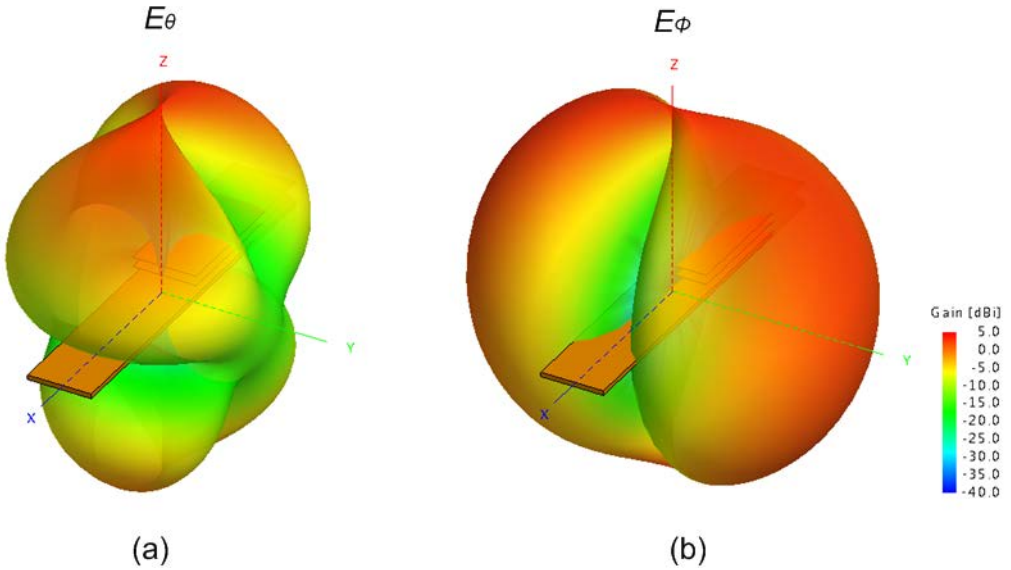


**Fig. 5.15. $E_\theta$ and $E_\Phi$ Directivities for wideband compact J-pole antenna. Far-field radiation patterns were calculated using FEKO.**

| | $TM_{mn}$ | | | $TE_{mn}$ | | |
|---|---|---|---|---|---|---|
| ***m*** | *n=1* | *n=2* | *n=3* | *n=1* | *n=2* | *n=3* |
| ***-1*** | 48.5 | - | - | 1.0 | - | - |
| ***0*** | 1.0 | - | - | - | - | - |
| ***1*** | 48.5 | - | - | 1.0 | - | - |

**Table 25. Far-Field *TM* and *TE* mode compositions for wideband compact J-pole antenna at *f=1.0 GHz*. Far-field radiation patterns and corresponding mode decompositions were obtained using FEKO. Relative power percentages *Pmn<0.5%* were omitted from the table for clarity.**

The planar compact J-pole antenna shown in this example is similar to the class of 'feed antennas' described by Sievenpiper [4]. Feed antennas are mounted on small ground planes that are typically shaped as a mobile phone or handheld device, in which a small resonant structure serves as an exciter of feed for a mode which involve the entire ground plane.

The geometry of the planar compact J-pole antenna may have a structural component that appears to be a ground plane, but a system designer would soon learn the antenna cannot arbitrarily be positioned on a typical handheld fixture shown earlier. The planar compact J-pole may also appear similar to a PIFA, but the far-field mode composition distinguished radiation properties between the two antennas. The following example demonstrates the result of incorrect antenna placement.

For this example the form factor of the handheld device was similar to dimensions of the WC J-pole shown in Table 26. The base plate was essentially extruded ten centimeters in an attempt to create a compatible handheld fixture. Fig. 5.16 is an illustration of the geometry.

The dashed traces in Fig. 5.17 show the degradation of the double-tuning and VSWR responses. The solid traces are the original baseplate structure similar to Fig. 5.14 for comparison.

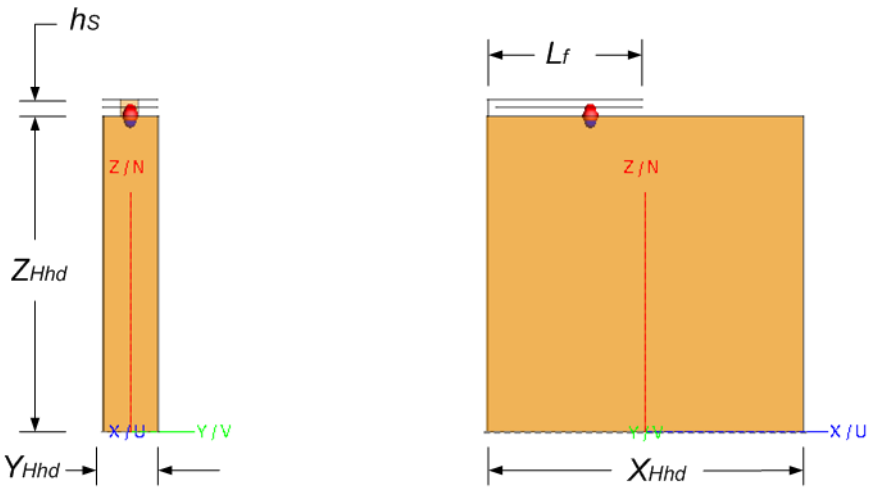


**Fig. 5.16. CADFEKO rendering of WC J-pole antenna mounted on handheld with same form-factor as original base plate.**

| $hs$ [mm] | $Z_{Hhd}$ [cm] | $Y_{Hhd}$ [cm] | $X_{Hhd}$ [cm] | $L_f$ [cm] |
|---|---|---|---|---|
| 6.6 | 10.0 | 2.2 | 12.5 | 6.1 |

**Table 26. Dimensions for the Wideband-Compact J-Pole Antenna mounted on handheld fixture shown in Fig. 5.16.**

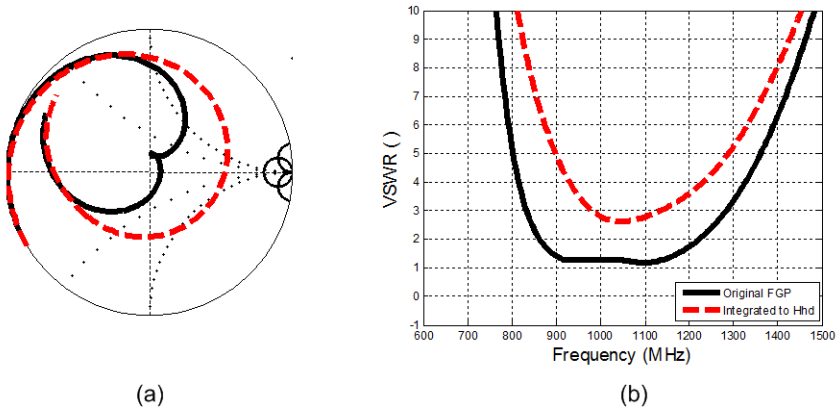


**Fig. 5.17. Smith Chart and VSWR Responses of WC J-pole antenna on original baseplate (solid) and mounted on the hand-held fixture shown in the previous figure (dashed). Impedance responses were calculated using FEKO.**

Fig. 5.18 (a) and (b) are three-dimensional radiation patterns for the WC J-pole antenna mounted on the handheld fixture. Table 27 shows some interesting changes in the modal content of the antenna-fixture system. Currents fed to the metallic fixture generate nearly 25% of the far-field radiated power in the $TM_{01}$ modes. The remaining 75% is divided into $TM_{11}$, $TM_{22}$, $TM_{23}$, $TE_{11}$, $TE_{22}$, and $TE_{23}$ modes. The integration of the metallic handheld device, even with consideration for the form factor generated dramatic results.

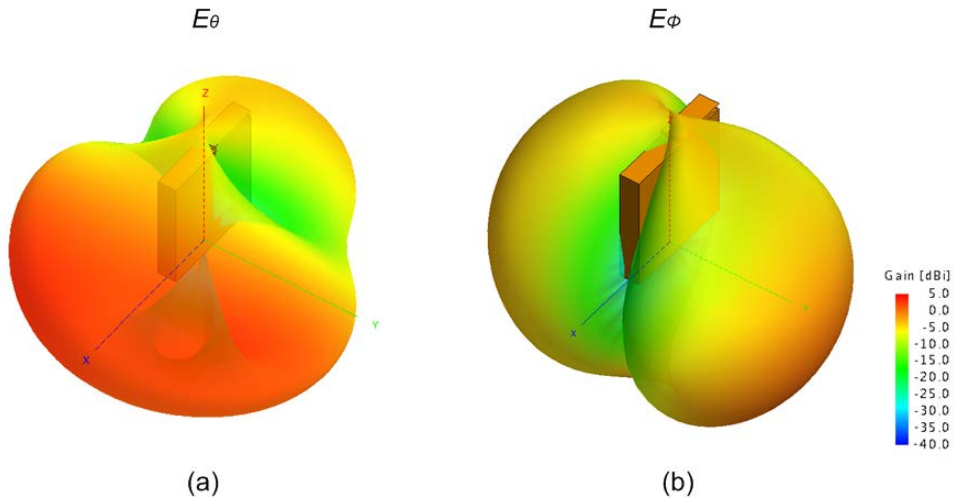


**Fig. 5.18. $E_\theta$ and $E_\phi$ Directivities for the wideband compact J-pole antenna mounted on a handheld fixture, $f_o$=1.0 GHz. Far-field radiation patterns were obtained using FEKO.**

| | $TM_{mn}$ | | | $TE_{mn}$ | | |
|---|---|---|---|---|---|---|
| ***M*** | *n=1* | *n=2* | *n=3* | *n=1* | *n=2* | *n=3* |
| ***-1*** | 3.6 | 15.2 | 8.4 | 5.2 | 3.1 | 1.0 |
| ***0*** | 12.6 | 9.0 | 2.4 | - | - | - |
| ***1*** | 3.6 | 15.2 | 8.4 | 5.3 | 3.1 | 1.0 |

**Table 27. Far-Field *TM* and *TE* mode compositions for wideband compact J-pole antenna mounted on handheld fixture, $f_o$ = 1.0 GHz (See Fig. 5.16). Far-field radiation patterns and corresponding mode decompositions were obtained using FEKO. Relative power percentages *Pmn<0.5%* were omitted from the table for clarity.**

Consideration for antenna placement is critical with the WC J-pole antenna. A dielectric handheld shell would mitigate the modal distribution of power shown for the metallic example. Another consideration would be how to practically feed such an antenna.

The wideband antenna over small ground plane example presented earlier would likely have similar problems in a laboratory environment. For the case where $S_{GP}=2a$, the coaxial feed cable connected to the antenna would require a great deal of care to minimize counterpoise currents setting up on the shield.

The following section introduces a low-profile multi-resonant structure that couples a U-slot to a microstrip patch antenna. The radiation characteristics are similar to the microstrip and the WC J-pole where most of the modal power not in the $TM_{0n}$ . The coupling interactions of the antenna are not yet completely understood in the community, but its low-profile, wide bandwidth characteristics make it another interesting antenna for consideration.

## 5.5 Multi-Resonant Patch - U-Slot Antenna

The physical properties of a microstrip antenna (e.g. low-profile and light weight) are optimal for many applications including military (UAV), mobile satellite communication, and Direct Broadcast system (DBS). Bandwidth requirements for the three examples shown preclude the use of a conventional microstrip antenna.

A single-resonant microstrip antenna (MSA) has a $VSWR \leq 2$ bandwidth of 3-5%. The addition of parasitics in stacked or coplanar geometries increases bandwidth but also increases the height and/or form-factor of the antenna. The bandwidths of single patch antennas can also be increased by implementing internal structures such as slots or shorting pins [5].

T. Huynh (no relation to M.C. Huynh of [3]) and Lee presented a probe-fed air-backed rectangular MSA with the addition of a U-slot to introduce double-tuning. The measured results indicated a single-layer, single-patch wideband MSA with an impedance bandwidth of 47%. [6]. The U-slot MSA antenna geometry from T. Huynh was scaled to $f_r = 1.0\ GHz$, where an engineering perspective and tabulated dimensions are shown in Fig. 5.19 and Table 28 respectively.

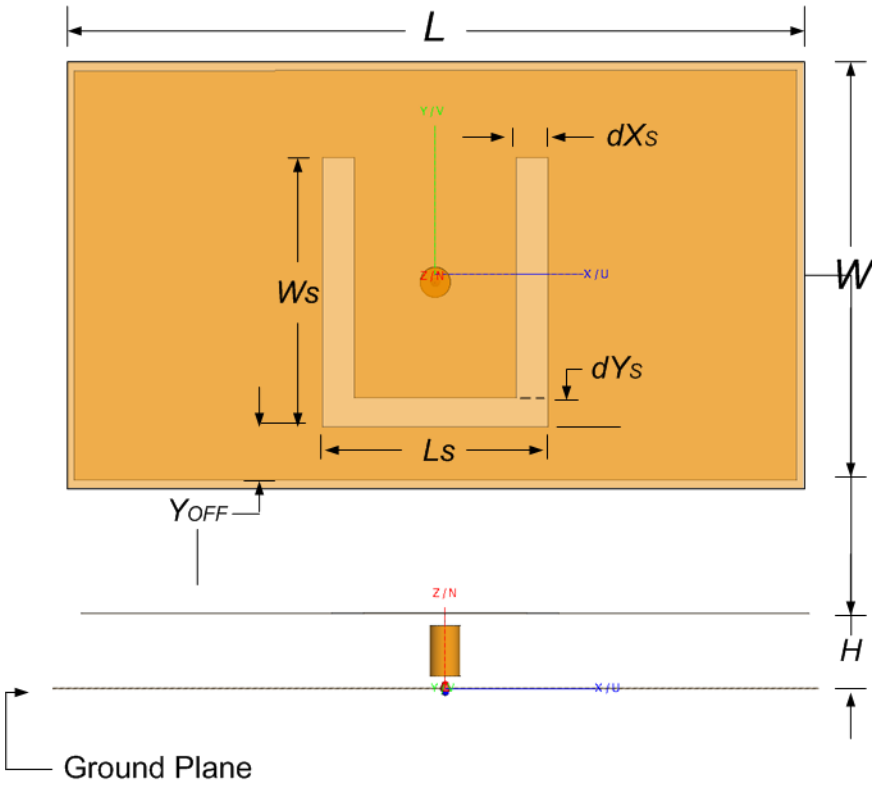


**Fig. 5.19. CADFEKO rendering of the U-slot microstrip antenna model.**

| $L$ [cm] | $W$ [cm] | $L_S$ [cm] | $W_S$ [cm] | $dX_S$ [mm] | $dY_S$ [mm] | $Y_{OFF}$ [cm] | $H$ [cm] |
|---|---|---|---|---|---|---|---|
| 21.97 | 12.45 | 6.86 | 7.79 | 9.7 | 8.5 | 1.86 | 2.29 |

**Table 28. Dimensions for the air-backed U-Slot antenna shown in Fig. 5.19. The antenna is mounted on a square ground plane, $S_{GP}$=38.7 cm.**

The U-slot is a multi-resonant structure with double-tuning characteristics that are difficult to characterize. Part of the U-slot antennas wideband impedance response is due to a resonance between the capacitive U-slot and the inductive probe-feed and/or the currents around the slot. A comprehensive parametric study of a similar patch by Weigand and Bernhard [7] indicated a qualitative explanation does not capture the complex relationships between the patch and U-slot geometries. For example, the currents on the patch surface cannot be separated into pure modes of either the slot or the patch.

Fig. 5.20 (a) and (b) are impedance responses of the separate radiation components of the U-slot microstrip antenna. A simple microstrip patch and a center-fed U-slot over a ground plane are shown as separate dashed traces. The U-slot establishes the lower resonant frequency and the

microstrip patch roughly sets the higher resonance. The coupling of the two is synergetic and generates a lower low-frequency and impressive impedance bandwidth characteristic.

$$a = \sqrt{\left(\frac{L}{2}\right)^2 + H^2} = 11.22\ cm \tag{1}$$

Approximating $f_L \approx 825\ MHz$, $\lambda_L \approx 36.4cm$

$$k_L a = 2\pi\left(\frac{a}{\lambda_L}\right) = 1.94 \tag{2}$$

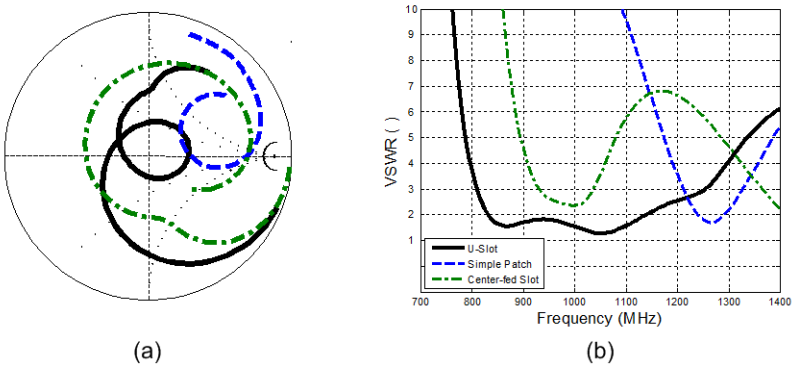


**Fig. 5.20. Composite VSWR responses of the radiation components of the U-slot microstrip antenna. Impedance responses for all cases shown were obtained using FEKO. Impedance responses for a simple patch and a center-fed U-slot over a ground plane are shown with the combined geometry showing the complementary interaction to create a double-tuning.**

Fig. 5.21 (a) and (b) are three-dimensional $E_\theta$ and $E_\phi$ radiation patterns for the U-slot microstrip antenna at $f = 1.0\ GHz$. Pattern shapes are very similar to the microstrip antenna from Chapter 3. Fig. 5.22 (a) and (b) are the three-dimensional for the square microstrip patch antenna mounted on a finite ground plane shown earlier in Chapter 3.

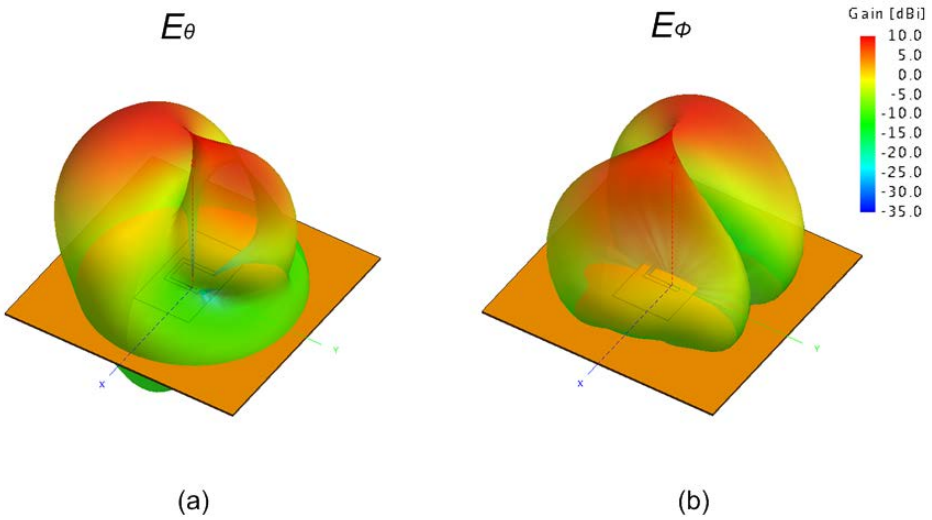


**Fig. 5.21.** ***$E_\theta$*** **and** ***$E_\Phi$*** **Directivities for the U-slot microstrip antenna mounted on a finite ground plane at** ***f =1.0 GHz*** **(see Fig. 5.19). The far-field radiation patterns shown were obtained using FEKO. Patterns shapes are very similar to the microstrip antenna from Chapter 3 with the only noticeable difference in pattern orientation.**

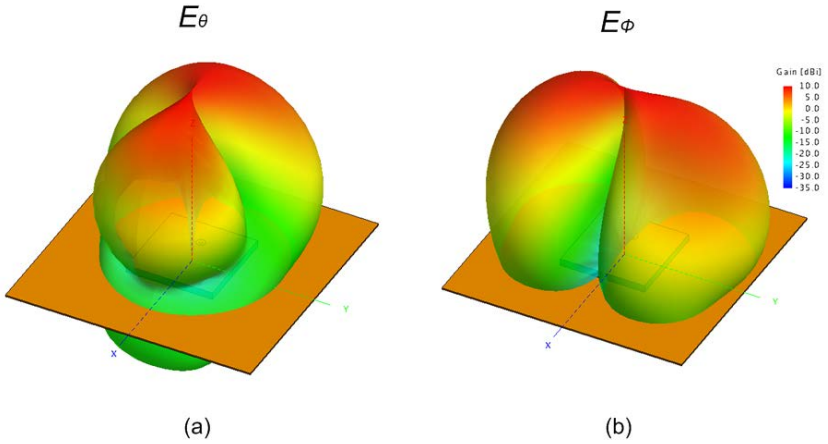


**Fig. 5.22.** ***$E_\theta$*** **and** ***$E_\Phi$*** **Directivities for the square microstrip patch antenna mounted on a finite ground plane at** ***f =1.0 GHz*** **(see Fig. 3.6). The far-field radiation patterns shown were obtained using FEKO. Patterns shapes are very similar to the microstrip antenna from Chapter 3 with the only noticeable difference in pattern orientation.**

| | $TM_{mn}$ | | | $TE_{mn}$ | | |
|---|---|---|---|---|---|---|
| ***M*** | ***n=1*** | ***n=2*** | ***n=3*** | ***n=1*** | ***n=2*** | ***n=3*** |
| ***-1*** | 13.8 | 7.7 | 1.9 | 12.8 | 5.3 | 1.0 |
| ***0*** | 6.0 | 2.9 | 0.3 | - | - | - |
| ***1*** | 13.9 | 7.7 | 1.9 | 12.8 | 5.3 | 1.0 |

**Table 29. Far-Field *TM* and *TE* mode Compositions for U-slot wide-band antenna at *f=1.0* GHz. Far-field radiation patterns and corresponding mode decompositions were obtained using FEKO. Relative power percentages *Pmn<0.5%* were omitted from the table for clarity.**

### 5.5.1 Sensitivity to Finite Ground Plane

Fig. 5.20 indicated the low-frequency radiation of the U-slot microstrip antenna is due primarily to the U-slot on the top of the patch antenna. The high-frequency response is the result of the antenna operating in a microstrip patch mode. Fig. 5.23 is an illustration showing the U-slot microstrip antenna mounted on a small square ground plane. A second case with the model boundary condition set to an infinite ground plane was created for comparison.

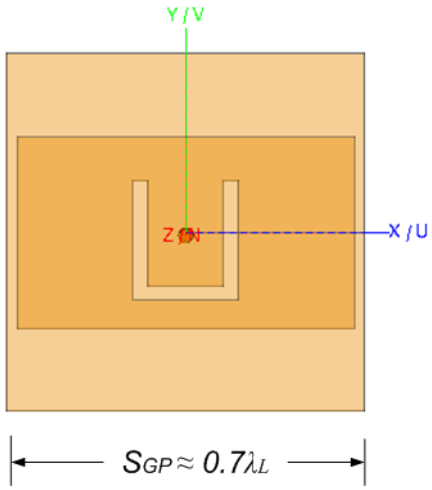


**Fig. 5.23. CADFEKO rendering of U-slot microstrip antenna mounted on small square ground plane.**

Fig. 5.24 (a) and (b) present normalized impedance and VSWR responses for limiting boundary conditions. One may observe the low-frequency response shows negligible variation due to changes in the ground plane. The higher frequency impedance response shows some (insignificant) variation.

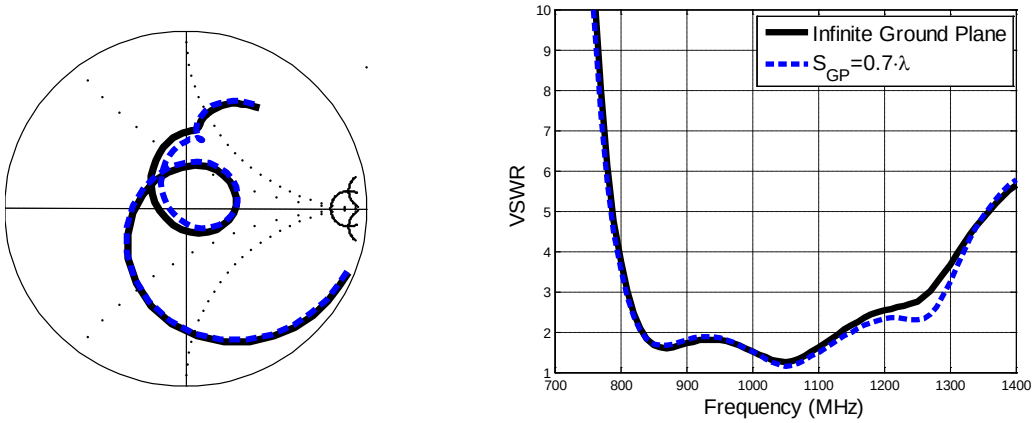


**Fig. 5.24. Smith Chart (a) and VSWR (b) Responses of U-slot microstrip antenna on minimum square ground plane. Impedance calculations were obtained using FEKO.**

### 5.5.2 Discussion - U-Slot Microstrip Patch Antenna

Most of the multi-resonant antennas reviewed in the chapter have some coupling characteristics that may not be observed independently. For example, two of the resonances in the Ravipati antenna are double-tuning structures coupling to the conical body-of-revolution. The third resonance presumably is the coupling of the two parasitics independently.

The authors in [7] observe the lower resonance is tied to the U-slot impedance response as shown in Fig. 5.20. The second resonance is strongly related to the fundamental mode of the microstrip patch. The third resonance is a complex interaction involving both structures. Their conclusion after a comprehensive investigation was that additional study is necessary to develop a more complete picture of the antenna characteristics.

## 5.6 Conclusions

Chapter five has introduced and reviewed a series of passive multi-resonant antennas and one ultra-wideband antenna to consider for wireless applications. The multi-resonant spiral and the Ravipati antennas efficiently utilized the volume enclosed by the radian sphere to create multiple radiation mechanisms. The three aforementioned antennas may be represented by combinations

of $TM_{0N}$ mode radiation. The Ravipati antenna maintains omnidirectional patterns and exhibit ground-plane compatibility similar to the monopole structures in Chapter 4.

Two low-profile multi-resonant antennas were also introduced. The wideband compact J-pole and the U-slot microstrip patch antennas are incorporate different double-tuning structures, but are similar in that both have a majority of the far-field radiated power outside the $TM_{0N}$ modes with peak power directed normal to the planar surface. The passive volume-centric antennas are ideal in terms of RF performance, but hardly acceptable in the current consumer wireless industry.

Chapter 6 will consider two active-device approaches to the quest for high throughput, multifunction small antenna solutions with long operating battery-cycle times. A harmonic tuning concept for the direct integration of a low-valued resistance small antenna as a direct load to a high efficiency switched power amplifier is also investigated as a means to improve antenna amplifier efficiency. A survey of the state of reconfigurable antenna hardware will also be included.

## 5.7 References


[1] H.R. Stuart, S.R. Best, A.D. Yaghjian, "Limitations in Relating Quality Factor and Bandwidth in a Double Resonance Small Antenna," IEEE Antennas and Wireless-Propagation Letters, vol. 6, 2007, pp. 460-463.

[2] S.R. Best, "The State of the Art in Small Wideband Antennas," The MITRE Corporation, 202 Burlington Road.

[3] M.C. Huynh, "Wideband Compact Antennas for Wireless Communication Applications," Ph.D. Dissertation, Virginia Tech Dept. of Electrical and Computer Engineering, Nov 22, 2004, pp. 85-131.

[4] D.F. Sievenpiper et al. ,"Experimental Validation of Performance Limits and Design Guidelines for Small Antennas," IEEE Transactions on Antennas and Propagation, vol. 60, no.1, January 2012, pp. 8-19.

[5] C.A. Balanis, *Antenna Theory, Analysis and Design*, 2nd ed. Wiley 1997, pp.722-752.

[6] T. Huynh, K.F. Lee, "Single-Layer, Single-Patch Wideband Microstrip Antenna," Electronic Letters-3rd, vol. 31, no. 16, August 1995, pp. 1310-1312.

[7] S. Weigand, G. Huff, J.T. Bernhard, "Analysis and Design of Broad-Band Single Layer Rectangular U-Slot Microstrip Patch Antennas," IEEE Transactions on Antennas and Propagation, vol. 51, no. 3, March 2003, pp. 457-467.

# 6 CHAPTER - Hardware Technologies

## 6.1 Introduction

The previous chapter investigated several passive multi-resonant, electrically-small antennas as potential solutions to market interest in better coverage, higher throughput, smaller form factors and longer battery cycles. Several wideband antennas were found to have ideal electrical qualities and require no active devices. Most of wideband antennas considered in Chapter 5 offered efficient use of the volume within the radian sphere, but did not have low-profile form factors, or were not representative monopole-class antennas. A reconfigurable, switch-tuned low-profile antenna monopole-class antenna was investigated in Chapter 4, where active tuning circuitry demonstrated implementation issues due to switch technology. One may conclude the ultimate system design solution would be a low-profile passive element with omnidirectional monopole-class radiation and a multi-resonant impedance response.

Additional consideration for the integration of a battery-driven power amplifier to a low-profile antenna transforms the original antenna design problem to a system design. Both the antenna and the battery-driven power amplifier are ‘long poles in the tent’ in the development of a portable, reliable and high-throughput device. Incredible advances in processing power of microelectronics, in addition to commensurate reductions in their respective size and weight, have revolutionized the microelectronics industry. Battery and antenna technologies have made advances albeit on (considerably) smaller scales.

This chapter will investigate two aspects of integrating hardware with small antennas on portable terminals. Engineering battery power for wireless personal communication systems strives to achieve a balance between the mutually exclusive goals of longer operating times and lightweight, compact design(s). Two strategies to reduce the RF power budget include power amplifier efficiency improvement, and minimization of DC power requirements for active element switching circuitry.

## 6.2 High Efficiency Power Amplifiers for Portable Applications

In wireless transmitters, the output power amplifier typically consumes the largest percentage of DC power [1]. One approach to increase battery life-span is to offset decreases in battery size and weight with improvements in DC to RF power conversion efficiency.

High efficiency, non-linear classes of power amplifiers have emerged from linear, controlled-current source class A and B power amplifiers. Class-F and inverse class-F power amplifiers are current examples of nonlinear, high-efficiency power amplifier topologies developed for battery-powered cellular phone handsets. These high drive-level power amplifiers boost efficiency and output by using harmonic resonators in the outputs to shape voltage and current drain waveforms.

For class-F, the voltage waveform includes one or more odd harmonics and approximates a square wave, while the current includes even harmonics and approximates a half sine wave. For inverse class-F, the voltage can approximate a half sine wave and the current a square wave. The efficiency of an ideal PA increases from 50% (class A) toward unity as the number of harmonics increases [2].

Power amplifiers for cellular applications implement harmonic tuning of class-F and inverse class-F amplifiers to optimize power conversion efficiency. The example in the next section considers integrating an inverse class-F amplifier directly to a single resonant low-profile antenna without a matching network. The single resonant antenna is modified to approximate the optimal load impedances at the first and second harmonics.

## 6.3 Integrated Inverse Class-F Amplifier Design with low-profile PIFA

Liw and Ellis investigated the adaptation of a low-profile PIFA to provide harmonic terminations to an inverse class-F amplifier [3]. Direct integration of a low-profile, electrically-small antenna to an integrated power amplifier would eliminate the requirement for a matching network between components. The antenna element is not only a radiating mechanism, but also part of the tuning network to appropriately terminate harmonics at the output of the amplifier. Integration of the antenna to the power amplifier is approached from both system components. The antenna would be designed to optimize harmonic loading to improve the transmitted power

efficiency, and the power amplifier would be designed for a load termination equal to the radiation resistance of the antenna ($R_{RAD}$ <*50 Ω*).

Liw and Ellis modified the structure of a conventional planar inverted-F antenna (PIFA) to improve the termination impedances at the first and second harmonics. Table 30 summarizes the optimal harmonic terminations for class-F and inverse class-F amplifiers. The harmonic loading for the inverse class-F amplifier geometry ideally provides an open circuit at the first harmonic and a short at the second harmonic[2].

| | ***1st* Harmonic *(n=1)*** | ***2nd* Harmonic *(n=2)*** |
|---|---|---|
| **Class –F** | **short** | **open** |
| **Inverse Class -F** | **open** | **Short** |

**Table 30. Class-F and Inverse Class-F Amplifier Harmonic Terminations**

Fig. 6.1 is an illustration of the PIFA model developed for inverse class-F amplifier integration. The model is an adaptation of [3] with an air-backed, parallel-plate transmission line mounted in series at the feed point beneath the ground plane. The second shorting pin is added to achieve a monotonic impedance response from the fundamental to the third harmonic shown in Fig. 6.2.

[2] $f_n = (n+1) \cdot f_0$

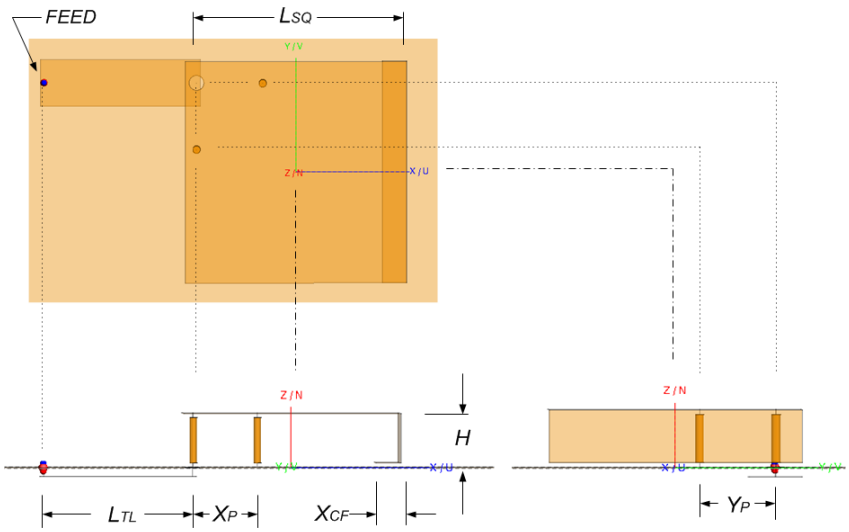


**Fig. 6.1. Three-view illustration of PIFA FEKO model designed for inverse class-F amplifier integration. An air-backed, parallel plate transmission line is mounted in series at the feed point beneath the finite ground plane. A second shorting pin is added to achieve a monotonic impedance response from the fundamental to the third harmonic.**

| $L_{SQ}$ [cm] | $L_{TL}$ [cm] | $X_P$ [cm] | $Y_P$ [cm] | $X_{CF}$ [cm] | $H$ [cm] |
|---|---|---|---|---|---|
| 3. 34 | 2. 3 | 1. 00 | 1. 00 | 0. 37 | 0. 84 |

**Table31. Dimensions for the PIFA model (shown in Fig. 6.1) designed for direct integration to and inverse class-F amplifier.**

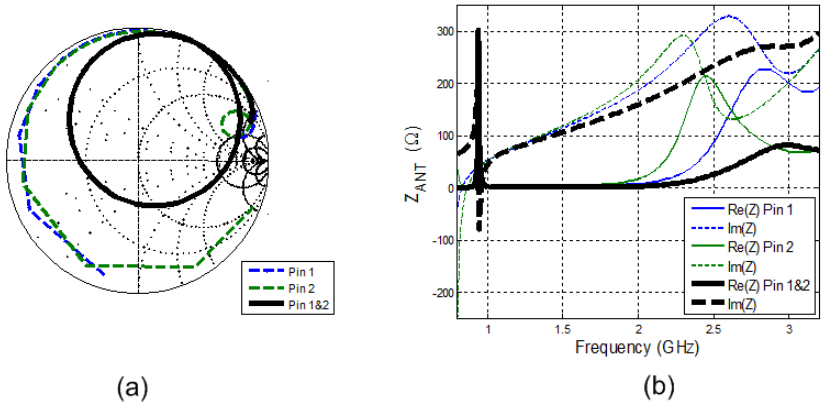


(a) (b)

**Fig. 6.2. Complex impedance responses versus shorting pin for the PIFA model (shown in Fig. 6.1) designed for integration to an inverse class-F amplifier. Impedance response calculations were obtained using FEKO. The complex impedance at the feed input for Pin 1 and Pin 2 are shown in blue and green respectively. The complex impedance response for the final geometry with both shorting pins is shown in black. For the final geometry both the real and imaginary parts are essentially monotonic across the bandwidth covering the third harmonic.**

Inductances of the shorting pins add in parallel and the combination shifts the inflection point above the third harmonic. The result is a monotonic complex impedance response. However, a second tuning element is required to utilize the monotonic impedance for $f_0<f<f_2$.

A series transmission line between the source and the antenna presents an additional degree of freedom to control the frequency dependent impedance. Impedance values versus line lengths for the fundamental, second, and third harmonics are used to determine the optimum line length to approximate the harmonic terminations for the inverse class-F power amplifier. Fig. 6.3 is a Smith chart representation of the pre-tuned and harmonically-tuned impedance responses for the inverse class-F amplifier integration with a PIFA termination. The ideal locations for the second and third harmonics are shown on the harmonically-tuned impedance response for the model shown in Fig. 6.1.

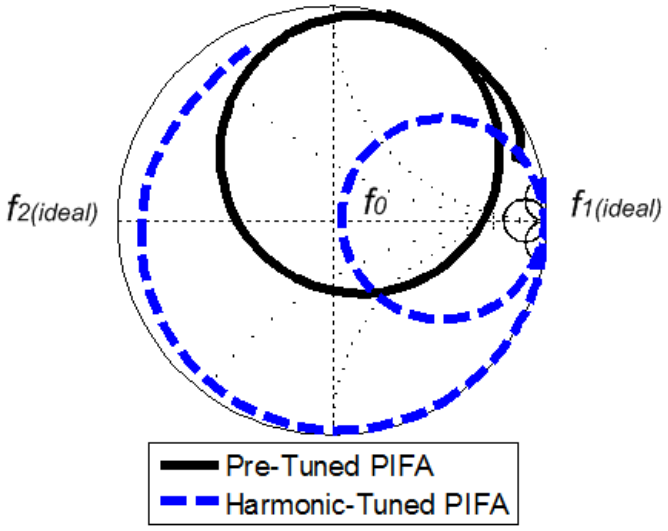


**Fig. 6.3. Smith Chart Format of Harmonic-Tuned PIFA (shown in Fig. 6.1) optimized for Inverse Class-F Amplifier Integration. Impedance responses were calculated using FEKO.**

The addition of tuning elements to improve the harmonic response characteristics of a small antenna for a portable application is an interesting example of modern small antenna design. The antenna element under consideration is passive, single-resonant and low-profile, however it is cleverly integrated with an active device for efficient portable operation. The next section focuses on current hardware technologies applied to active, reconfigurable antenna structures.

## 6.4 Hardware Evaluation

Active, reconfigurable antenna research generates high interest in both public and private sectors of the wireless communication industry. A portion of the dissertation research was supported by collaboration with Applied EM, Inc., where a preliminary objective was to consider a switch-tunable 'PIFA-as-a-package' similar to the work of Feldner et al for a portable UHF communication device [4].

The term 'PIFA-as-a-package' was first observed in [4] which demonstrated the potential utility of switch-tunable reconfigurable antennas for portable UHF wireless devices. The electrically-small, frequency-agile prototype was fabricated by technical staff at Sandia Laboratories. Pin diodes replaced the original MEMS switches to satisfy actual power-handling requirements due to the current transformation between the feed and the tuning strap surface

area(s). The overall height for the prototype was approximately $h \approx \lambda/90$. Measured performance included a near-contiguous tuning coverage between 407.8-463.1 MHz with a total realized gain of better than -10 dBi across the tuning range. The operational bandwidth based upon the tuning range corresponds to approximately 13%.

The single mode Wheeler-Chu fundamental lower bound based upon the circumscribing radius was determined to be approximately $Q_A \approx 45$. A half-power quality factor corresponded to twice the antenna quality factor $Q_{HP} \approx 22.5$ resulting in a half-power bandwidth estimate for a single-mode monopole-class structure, $B_{HP} \approx 4.5\%$. The combination of switch-tuning in addition to the losses incurred due to the circuitry nearly tripled the total operating bandwidth as a composite ensemble of several tuned instantaneous bandwidths.

Measured results for both the Sandia Laboratories and Applied EM, Inc. prototypes were significantly impacted by the presence of the PIN diode DC bias lines integrated to the antenna. Both the Sandia and Applied EM prototypes utilized commercial-off-the-shelf surface mount PIN diodes (NEC UPG2214TK) as active-switch control of the tuning straps. The insertion loss and isolation of each switch at *f= 500 MHz* is approximately *0.25 dB* and *70dB* respectively.

High quality micro-electromechanical (MEMS) switches potentially offer lower insertion loss and isolation properties, but are typically current-limited and require a high DC activation voltage which may be problematic with a portable device. Micro-electromechanical switches were originally chosen for the Sandia prototype, however the resulting impedance transformed maximum current(s) through the tuning straps and individual switches exceeded MEMS specifications.

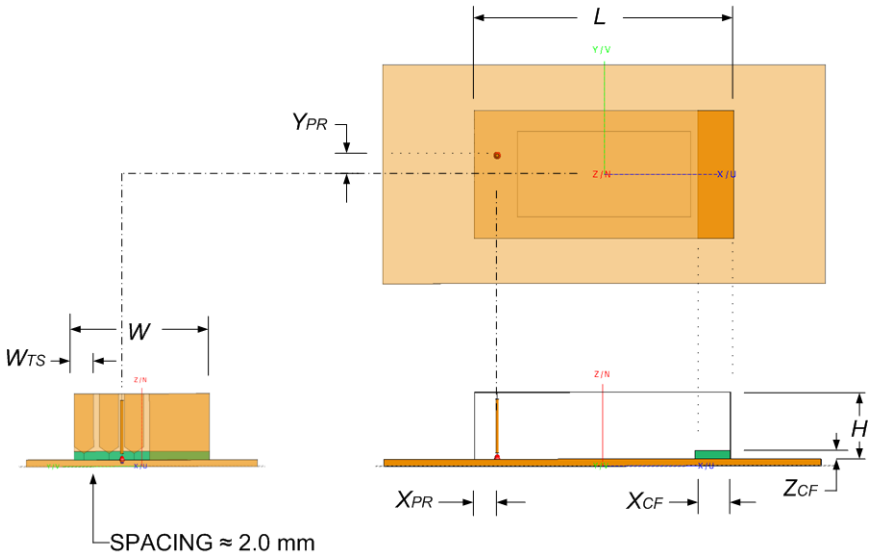


**Fig. 6.4. CADFEKO rendering of switch-tuned PIFA with capacitive-loading.**

PIN diode and similar solid-state switch properties may be modeled with lumped elements: a resistor for the 'on' state, and a capacitor for the 'off' or open state. Parasitic effects of the biasing circuitry and DC ground paths affected the closed switch states, particularly with respect to an apparent loss. The largest influence was due primarily to the relatively long RF paths to ground through the active switches and possible interaction with the DC bias lines. Chapter 4 presented measured antenna impedance results for the Applied EM, Inc. active, switch-tuned PIFA antenna designed for UHF ($f_o \approx 450\ MHz$) shown again in Fig. 6.5.

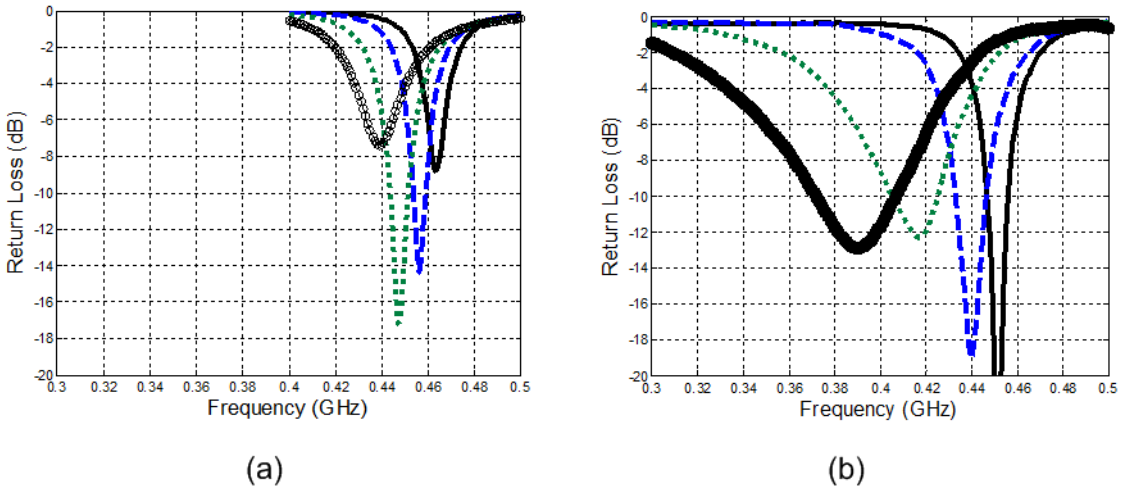


**Fig. 6.5. Ideal switch simulated Return Loss (a) and active-switch measured Return Loss responses. The ideal impedance response characteristics were calculated using the FEKO model shown in Fig. 6.4. The measured responses were obtained from the active-switch prototype introduced in Chapter 4 (see Fig. 4.25. VTAG original test setup of the switch-tuned PIFA shown in Fig. 4.24**

Additional examples of active switch integration to Low-Profile antenna structures to achieve reconfiguration have been investigated for multi-band cellular applications [5, 6]. Both Boyle [5] and Karmakar [6] pursued non-contiguous multiband structures to switch between cellular bands over a bandwidth of approximately one octave. Boyle observed that switch circuitry located on a reconfigurable antenna structure is a challenging design tradeoff since isolation must be maintained with a minimum required number of connections between the antenna and the supporting device.

The fabrication and implementation of a reconfigurable antenna structure presents engineering challenges to achieve consistent efficient operation. Switch isolation and fabrication difficulties continue at the proof-of-concept stage of antenna research and design. The integration of surface-mount commercial-off-the-shelf (COTS) switch elements in an antenna fabrication presents additional challenges. Huff and Bernhard at University of Illinois [7] document modifications and difficulties encountered integrating COTS MEMS switches to an endfire-to-broadside reconfigurable antenna. Some of the problems they encountered include the following:

1. modification of switch packaging to avoid impedance mismatch with antenna
2. inclusion of bias networks on antenna structure

3. utilize the RF ground as shared DC power-plane

In a subsequent paper, Dr. Bernhard [8] made an interesting observation, “The reconfigurability mechanism for antennas is typically one of the most challenging yet often ignored aspects of reconfigurable antennas. Researchers often find it difficult to implement switching or control mechanisms into antennas originally developed using hard-wired connections for proof-of-concept prototypes.”

## 6.5 Summary

Two aspects of integrating hardware with small antennas on portable terminals were introduced. The modification or design of passive low-profile antennas to provide harmonic terminations for high-efficiency power amplifiers is an interesting and current research area for portable communication devices. The example illustrated the potential for improved power efficiency for a low-profile, single resonant, narrow-band antenna element.

Reconfigurable antennas with active, switch-tuning for both contiguous and multi-band operation were also discussed. The strategy for reconfigurable antenna applications is to increase or optimize a total operating bandwidth comprised of a finite number of instantaneous bandwidths. Engineering challenges and fabrication incompatibilities limit the success of current research efforts.

Chapter 7 will introduce a double-resonant passive low-profile antenna that is suitable for portable device applications.

## 6.6 References


[1] F.H. Raab et al., “Power Amplifiers and Transmitters for RF and Microwave,” IEEE Trans. on Microwave Theory and Techniques, vol. 50, no.3, Mar 2002, pp. 814-818.

[2] F. H. Raab, “Maximum Efficiency and Output of Class-F Amplifiers,” IEEE Trans. on Microwave Theory and Techniques, vol. 49, no. 6, June 2001, pp. 1162-1166.

[3] Saxon Liw, G. A. Ellis, "Planar Inverted-F Antennas as an Inverse Class-F Termination for Wireless Applications," IEEE Antennas and Propagation Letters, vol. 2, Feb 2003, pp. 250-253.

[4] L. Feldner, "Electrically Small, Frequency-Agile Antenna-as-a-Package for Portable Wireless Devices," IEEE Transactions on Antennas and Propagation, vol. 55, no. 11, , Nov 2007, pp. 3310-3319.

[5] K. R. Boyle, "A Five-Band Reconfigurable PIFA for Mobile Phones," IEEE Transactions on Antennas and Propagation, vol. 55, no. 11, Nov 2007, pp. 3300-3310.

[6] N. C. Karmakar, “Shorting Strap Tunable Stacked Patch PIFA,” IEEE Trans. Antennas and Propagation, vol. 52, no. 11, Nov 2004, pp. 2877-2883.

[7] G.H. Huff, J.T. Bernhard, “Integration of Packaged RF MEMS Switches with Radiation Pattern Reconfigurable Square Spiral Microstrip Antennas,” IEEE Trans. Antennas and Propagation, vol. 54, no. 2, Feb 2006, pp. 464-469.

[8] J.T. Bernhard, “Reconfigurable Multifunction Antennas: Next Steps for the Future,” IEEE 2007 International Symposium on Microwave, Antenna, Propagation, and EMC Technologies for Wireless Communications (MAPE 2007)

# 7 CHAPTER - Multi-resonant Low-Profile Example

## 7.1 Introduction

This chapter introduces a passive, low-profile multi-resonant antenna element that is well-suited for portable communications. The antenna combines the attractive low-profile geometry of a planar inverted-F antenna with a double-tuned structure to create a low-profile multi-resonant element with monopole-class radiation properties. The form factor and overall dimensions are held constant for comparisons to a similar single-resonant antenna in both the finite ground plane and handheld geometries shown previously.

## 7.2 The Antenna Structure

The geometry of the double-tuned planar inverted-F antenna is shown in Fig. 7.1. The dimensions for the antenna listed are presented in Table 32. The antenna is an extension of the conventional PIFA discussed in Chapter 4. Some miniaturization is achieved with air-backed capacitive-loading. Air-backed dielectrics and perfectly conducting metal are utilized to create a lossless antenna model in a commercial method-of-moments software (FEKO).

The geometry of the slot controls the coupling between the two elements. The two critical parameters include the slot-width or the separation between the two elements, and the nature of the slot-termination on the vertical shorting element. The vertical shorting bar is common at the base of the PIFA and increases the coupling to the parasitic element. The overall height of the antenna is less than one centimeter corresponds to an electric height of $h \approx \lambda/35$.

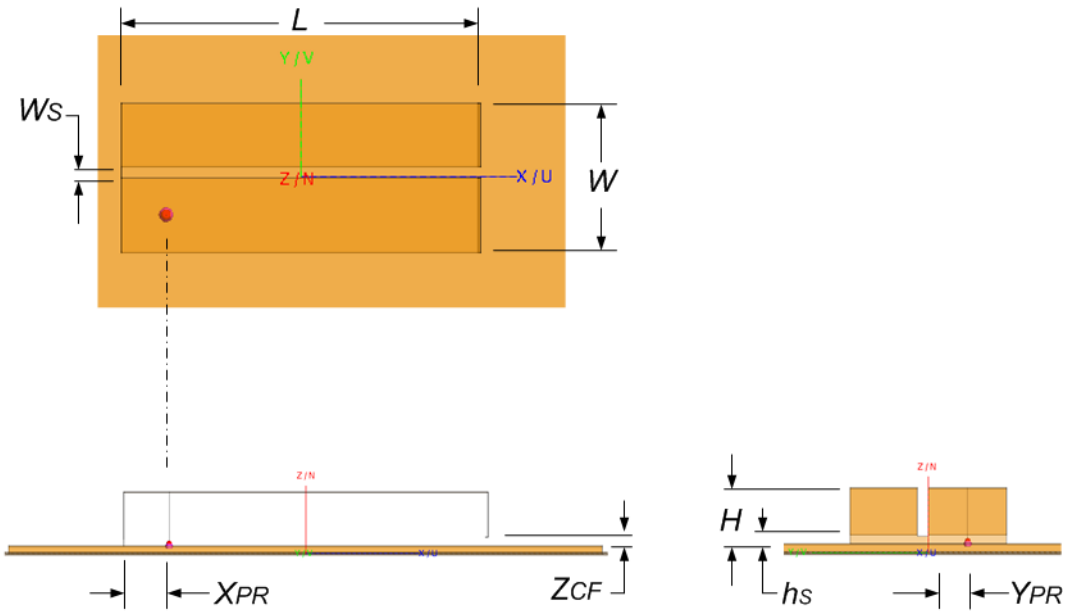


**Fig. 7.1. CADFEKO rendering of multi-resonant planar inverted-F antenna.**

| $L$ [cm] | $W$ [cm] | $H$ [cm] | $W_S$ [mm] | $h_S$ [mm] | $X_{PR}$ [mm] | $Y_{PR}$ [mm] | $Z_{CF}$ [mm] |
|---|---|---|---|---|---|---|---|
| 5.52 | 2.29 | 0.83 | 1.65 | 1.10 | 8.9 | 5.7 | 1.4 |

**Table 32. Dimensions for the model geometry of the multi-resonant PIFA shown in Fig. 7.1.**

Fig. 7.2 (a) and (b) are combined plots of the impedance responses for the multi-resonant (solid) and single-resonant (dashed) planar inverted-F antennas with similar form-factors. The boundary condition for the simulations shown was set for infinite ground plane. A significant double-tuning loop due to the slot-coupling between the source-driven and parasitic elements seen in the Smith chart (a) corresponds to the double-resonant bandwidth enhancement shown in the VSWR plot (b). The half-power bandwidths observed from the VSWR responses are approximately *82 MHz* and *54 MHz* for the multi-resonant and single-resonant elements respectively. The integration of the parasitic element within the same structural form factor results in greater than $\Delta B_{HP} > 50\%$ increase in half-power bandwidth.

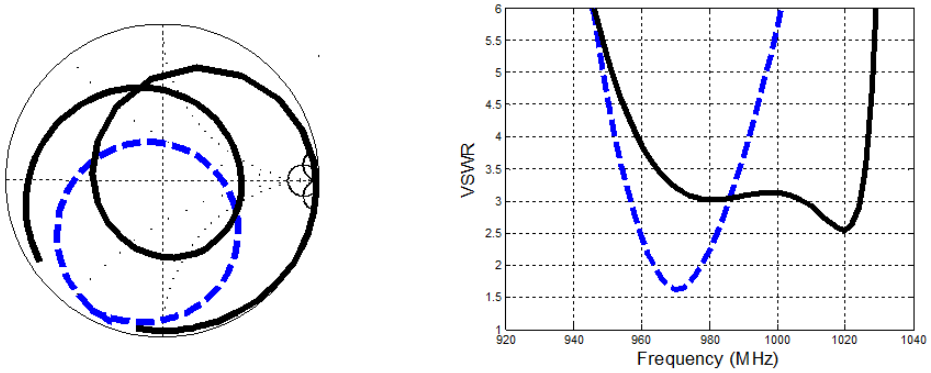


**Fig. 7.2. Normalized Impedance (a) and VSWR (b) responses for multi-resonant (solid – see Fig. 7.1) and single-resonant (dashed) planar inverted-F antennas with similar form-factors. Impedance response calculations were obtained using FEKO. The boundary condition for the simulations shown was a perfectly-conducting infinite ground plane.**

The multi-resonant impedance response obtained with the addition of the parasitic element. Coupling control was achieved primarily with adjustment of the slot height along the vertical shorting element and the slot width. Fig. 7.3 and Fig. 7.4 are illustrations of the parametric variations in the impedance response as functions of the slot height and slot width, $h_S$ and $W_S$ respectively.

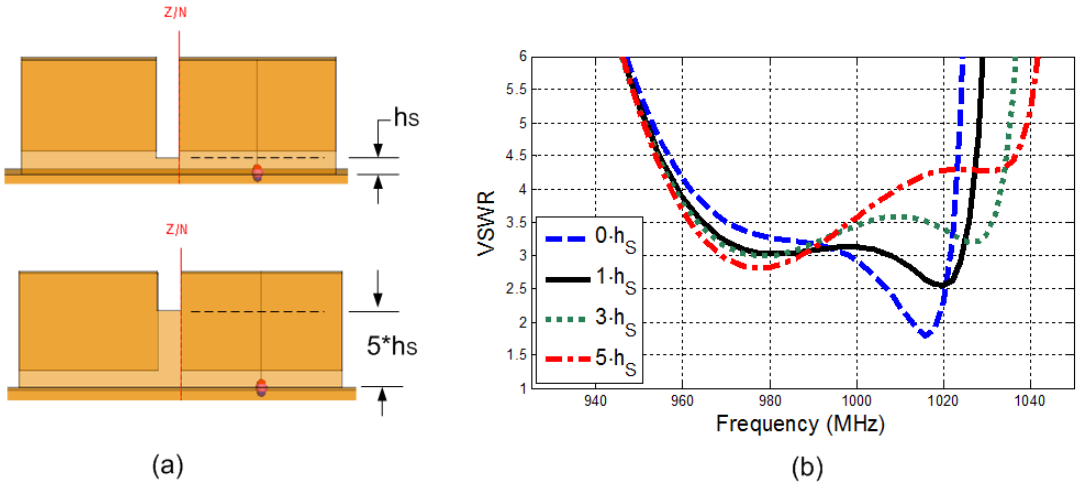


**Fig. 7.3. VSWR Response versus slot-height on PIFA vertical shorting bar. Impedance response calculations were obtained using FEKO. The slot width parameter, $W_S$ is the value shown in Table 7.2.1**

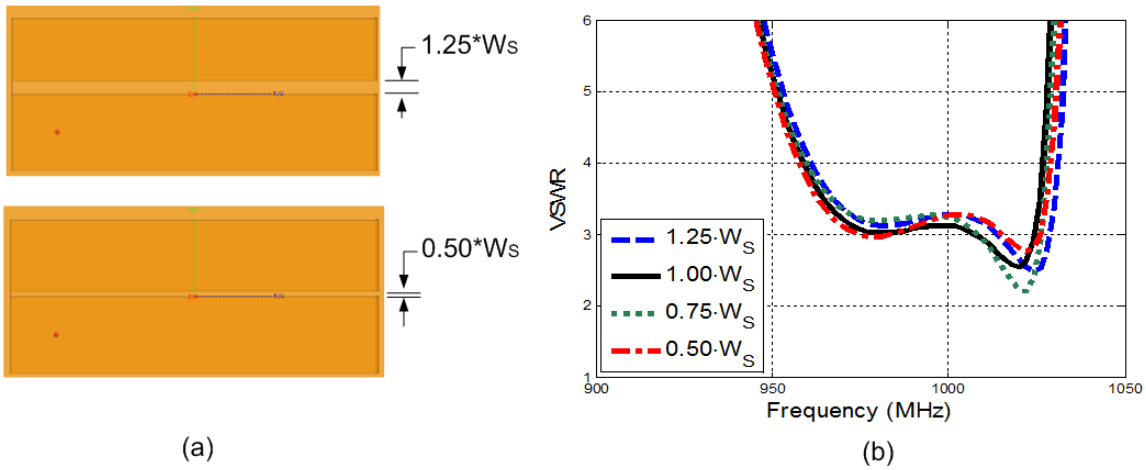


**Fig. 7.4. VSWR response versus slot-width on PIFA. Impedance response calculations were obtained using FEKO. The slot height parameter, $h_S$ is the value shown in Table 32.**

Some insight may be obtained from planar coupled-resonators that yield wide bandwidths similar to multistage tuned circuits. Multiple configurations for gap-coupling a driven planar microstrip patch antenna to parasitic(s) along radiating edges, non-radiating edges, and along all edges are available in literature [1, 2]. However, comparisons of the vertical and horizontal coupling controls seen in Fig. 7.3 and Fig. 7.4 indicate the sensitivity was more pronounced with adjustments to the slot-height on the vertical shorting bar than the slot-width. The increased sensitivity seen in Fig. 7.3 compared to Fig. 7.4 is due to the higher surface current densities on the vertical shorting bar compared to the entire structure. Surface current magnitudes on the vertical shorting bar(s) are directly related to the impedance transformation between the impedance seen at the feed and the radiation resistance. The increased vertical current on the shorting bar(s) accounts for the predominant $TM_{0N}$ monopole-class radiation that characterizes the PIFA.

Fig. 7.5. Three-Dimensional $E_\theta$ (a) and $E_\phi$ (b) radiation patterns for the multi-resonant PIFA mounted on a square finite ground plane $S_{GP}=\lambda$. (a) and (b) are three-dimensional $E_\theta$ and $E_\phi$ radiation patterns for the multi-resonant PIFA mounted on a finite ground plane $S_{GP}=\lambda$. The $E_\theta$ radiation pattern shown is similar to the conventional PIFA mounted at the center of a small square ground plane shown in Chapter 4. The $E_\phi$ radiation pattern for the multi-resonant PIFA shows a nominal increase in ripple on the horizon ($\theta \approx 90^o$).

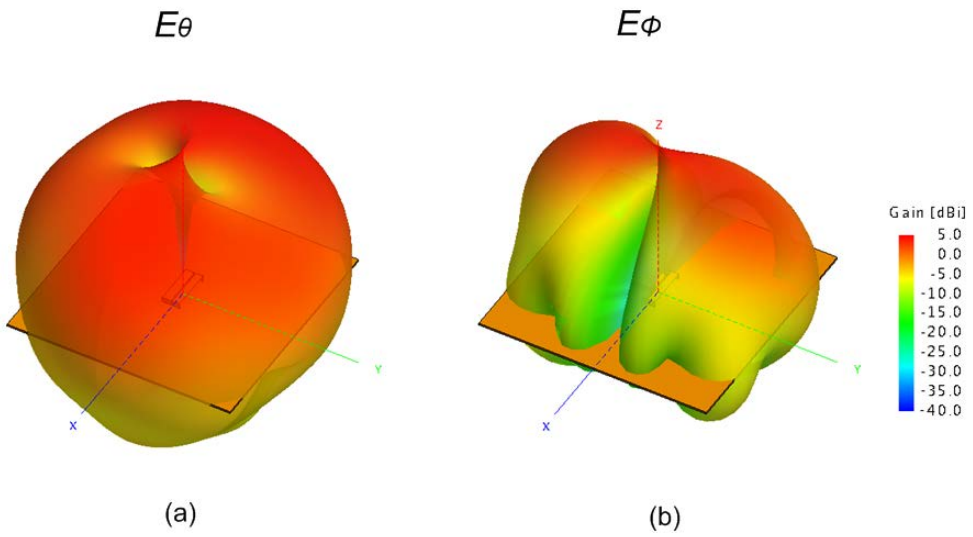


**Fig. 7.5. Three-Dimensional $E_\theta$ (a) and $E_\phi$ (b) radiation patterns for the multi-resonant PIFA mounted on a square finite ground plane $S_{GP}=\lambda$. Far-field radiation patterns were calculated using FEKO.**

Fig. 7.6 displays top-views of the multi-resonant (a) and single-resonant (b) PIFAs with their respective percent power *TM* and *TE* mode decompositions. The feed locations and overall form-factors are identical for both models mounted on square ground planes $S_{GP}=\lambda$. The multi-resonant and single resonant models are nearly identical in terms of modal power distributions. Both have nearly equal percentages in the $TM_{01}$ and $TM_{02}$, where the $TM_{02}$ component accounts for the pattern 'shaping' below the finite ground plane. Nearly 30% modal power contained in the $TE_{mn}$ modes, where $|m|=1$.

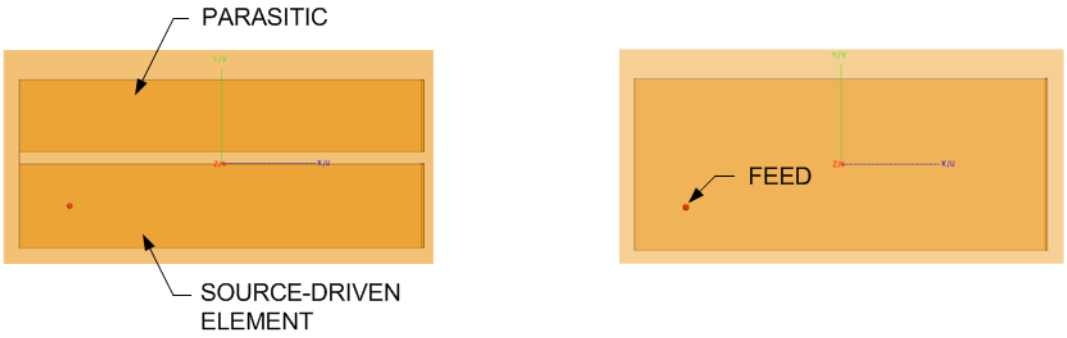


| $TM_{mn}$ | | | | |
|---|---|---|---|---|
| *m* | *n=1* | *n=2* | *n=3* | *n=4* |
| -4 | - | - | - | **2.3** |
| -3 | - | - | **1.1** | - |
| -2 | - | - | - | - |
| -1 | **7.6** | - | - | - |
| 0 | **24.3** | **21.3** | - | **1.4** |
| 1 | **7.7** | - | - | - |
| 2 | - | - | - | - |
| 3 | - | - | **0.9** | - |
| 4 | - | - | - | **2.3** |

| $TE_{mn}$ | | | | |
|---|---|---|---|---|
| *m* | *n=1* | *n=2* | *n=3* | *n=4* |
| -2 | - | - | - | - |
| -1 | **11.3** | **2.8** | - | - |
| 0 | - | - | - | - |
| 1 | **12.5** | **3.1** | - | - |
| 2 | - | - | - | - |

(a)

| $TM_{mn}$ | | | | |
|---|---|---|---|---|
| *m* | *n=1* | *n=2* | *n=3* | *n=4* |
| -4 | - | - | - | **2.3** |
| -3 | - | - | **1.0** | - |
| -2 | - | - | - | - |
| -1 | **7.8** | - | - | - |
| 0 | **24.5** | **21.3** | - | **1.4** |
| 1 | **7.5** | - | - | - |
| 2 | - | - | - | - |
| 3 | - | - | **1.0** | - |
| 4 | - | - | - | **2.3** |

| $TE_{mn}$ | | | | |
|---|---|---|---|---|
| *m* | *n=1* | *n=2* | *n=3* | *n=4* |
| -2 | - | - | - | - |
| -1 | **12.1** | **3.0** | - | - |
| 0 | - | - | - | - |
| 1 | **11.6** | **2.9** | - | - |
| 2 | - | - | - | - |

(b)

**Fig. 7.6. Far-Field *TM* and *TE* mode Compositions for multi-resonant PIFA mounted on a finite ground plane $S_{GP}=\lambda$. Far-field mode decompositions were calculated using FEKO.**

Differences observed in the radiation pattern and percent power modal distributions are minimal between the multi-resonant and single-resonant models mounted on square ground planes. A second step to evaluate the multi-resonant PIFA is to mount on the handheld chassis. Chapter 4 demonstrated single-resonant monopole-class antennas were less sensitive to antenna placement/structure interaction, where Chapter 5 illustrated an example of a multi-resonant low-profile antenna that suffered significant detuning with a similar change in boundary conditions. The purpose of the step is to determine if the multi-resonant PIFA maintains the double-tuning impedance characteristic and omnidirectional radiation in azimuth when subjected to a different boundary condition and near-field environment.

Fig. 7.7 illustrates the integration of the multi-resonant PIFA to the handheld device platform utilized previously. The dimensions of the lossless chassis are approximately *H=10 cm, W=6.5 cm* and *D=4.0 cm.*

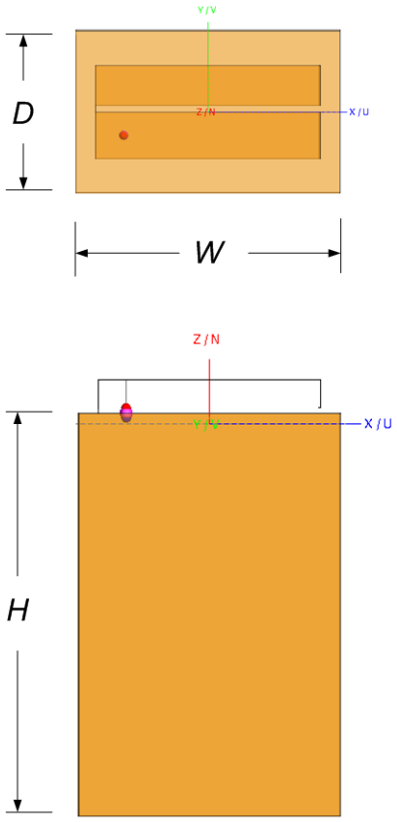


**Fig. 7.7. CADFEKO renderings of multi-resonant PIFA integrated to a handheld device. The dimensions of the chassis are approximately *H=10 cm, W=6.5* cm and *D=4.0* cm.**

Fig. 7.8 illustrates the normalized impedance (a) and VSWR (b) responses for the multi-resonant PIFA integrated to a handheld device. The position of the probe and parameters of the slot were unchanged from the finite ground plane example shown earlier. The result indicates the double-tuning characteristic is maintained with the change in finite ground plane/near-field environment of the radiating structure.

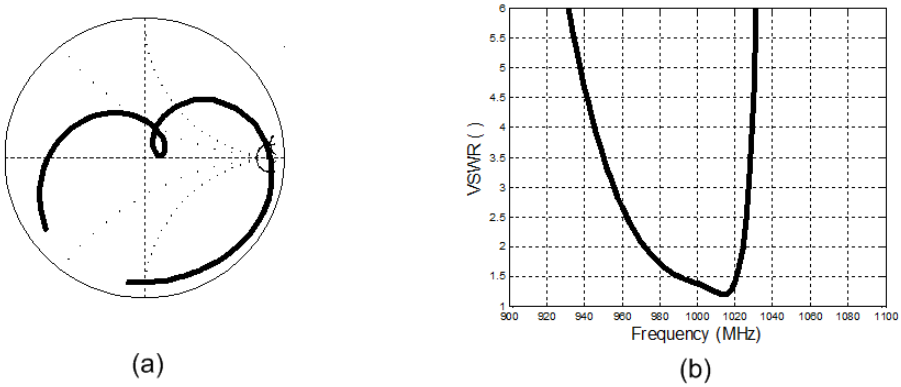


**Fig. 7.8. Normalized Impedance (a) and VSWR (b) responses for multi-resonant planar inverted-F antenna mounted on a handheld device (see Fig. 7.7). The impedance response was calculated using FEKO. The position of the probe and parameters of the slot were unchanged from the finite ground plane example.**

Fig. 7.9 presents the $E_\theta$ (a) and $E_\phi$ (b) radiation patterns for the multi-resonant PIFA mounted on a handheld chassis. The significant coupling between the driving element and the parasitic creates nearly symmetric patterns with negligible differences in comparison to the single resonant PIFA mounted to the same chassis.

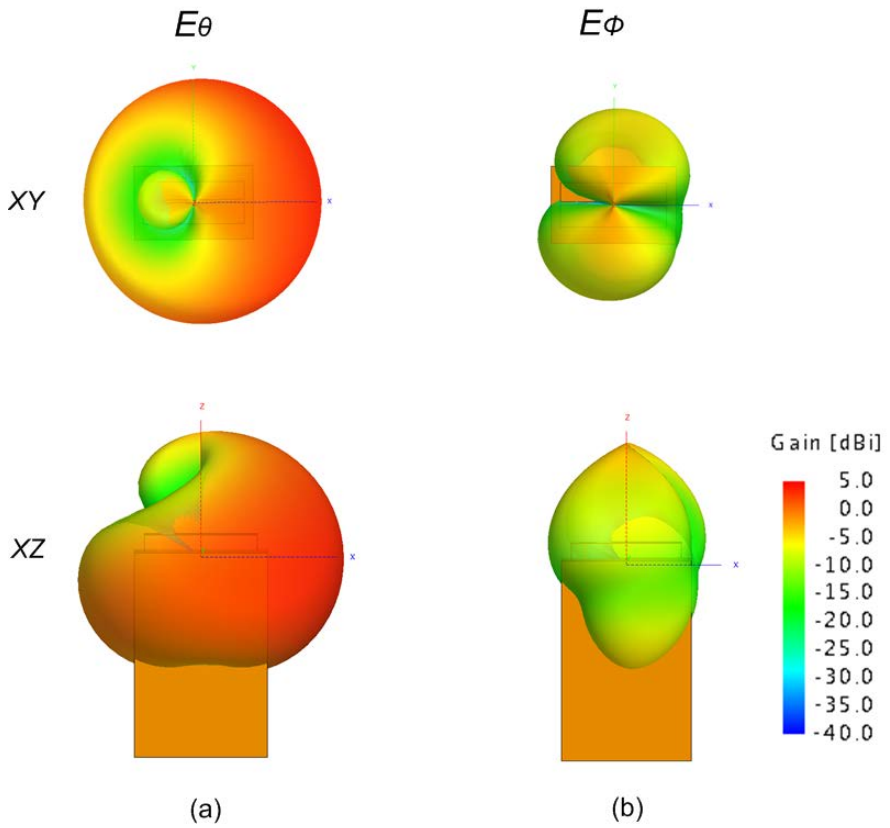


**Fig. 7.9.** ***$E_\theta$*** **(a) and** ***$E_\phi$*** **(b) Radiation Patterns for the multi-resonant PIFA mounted on a handheld chassis (see Fig. 7.7). The far-field radiation patterns were calculated using FEKO.**

Table 33 provides the far-field *TM* and *TE* mode compositions for the multi-resonant PIFA mounted on a handheld chassis (see Fig. 7.7) for the far-field *TM* and *TE* percent power mode distributions for the multi-resonant PIFA mounted on the handheld chassis. The absence of the square ground plane reduces the $TM_{mn}$ components for $n \geq 2$. Nearly 20% of the modal power is *TE* mode.

| | $TM_{mn}$ | | $TE_{mn}$ | |
|---|---|---|---|---|
| ***m*** | ***n=1*** | ***n=2*** | ***n=1*** | ***n=2*** |
| -1 | 0.7 | 0.5 | 8.1 | - |
| 0 | 68.2 | 7.5 | - | - |
| +1 | 3.2 | - | 10.7 | - |

**Table 33. Far-Field *TM* and *TE* mode Compositions for the multi-resonant PIFA mounted on a handheld chassis (see Fig. 7.7). Far-field radiation patterns and corresponding mode decompositions were calculated using FEKO.**

Tuning of the multi-resonant PIFA on the handheld chassis can be improved with minor adjustments to the coupling factors and probe position. Fig. 7.10 presents the normalized impedance (a) and VSWR (b) responses for the double-resonant inverted-F antenna mounted on the handheld chassis. The 2:1 VSWR bandwidths for the single-resonant and multi-resonant antennas are 46 MHz and 65 MHz respectively. The double-tuning seen clearly in Fig. 7.10 (a) results in a 2:1 VSWR bandwidth improvement of greater than 40%.

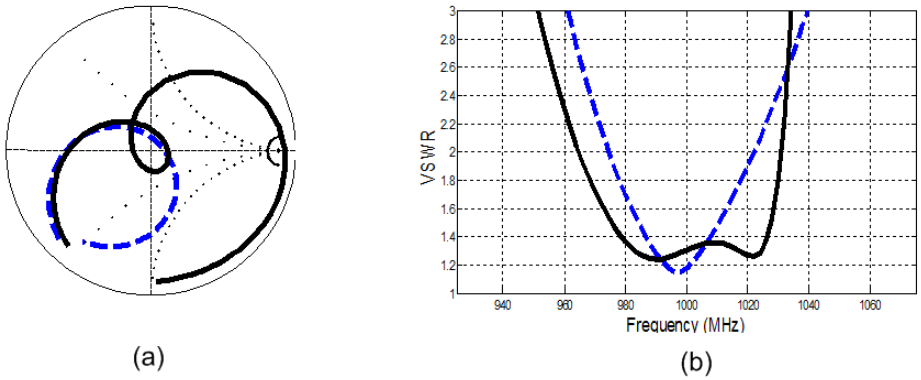


**Fig. 7.10. Normalized Impedance (a) and VSWR (b) Responses for tuned multi-resonant (black-solid) and single-resonant (blue-dashed) PIFAs mounted on the handheld chassis (see Fig. 7.7). Impedance response calculations were obtained using FEKO. The double-tuning improves the 2:1 VSWR bandwidth, *ΔB=41%*.**

Fig. 7.11 (a-d) are post-processed renderings of the surface current distributions on the multi-resonant PIFA mounted on the handheld chassis. The magnitudes of the surface current densities on both the driven and parasitic elements are comparable. Some phasing is observed at $\omega t=[0^o,180^o]$ where the currents on the parasitic element are lagging the driven element currents.

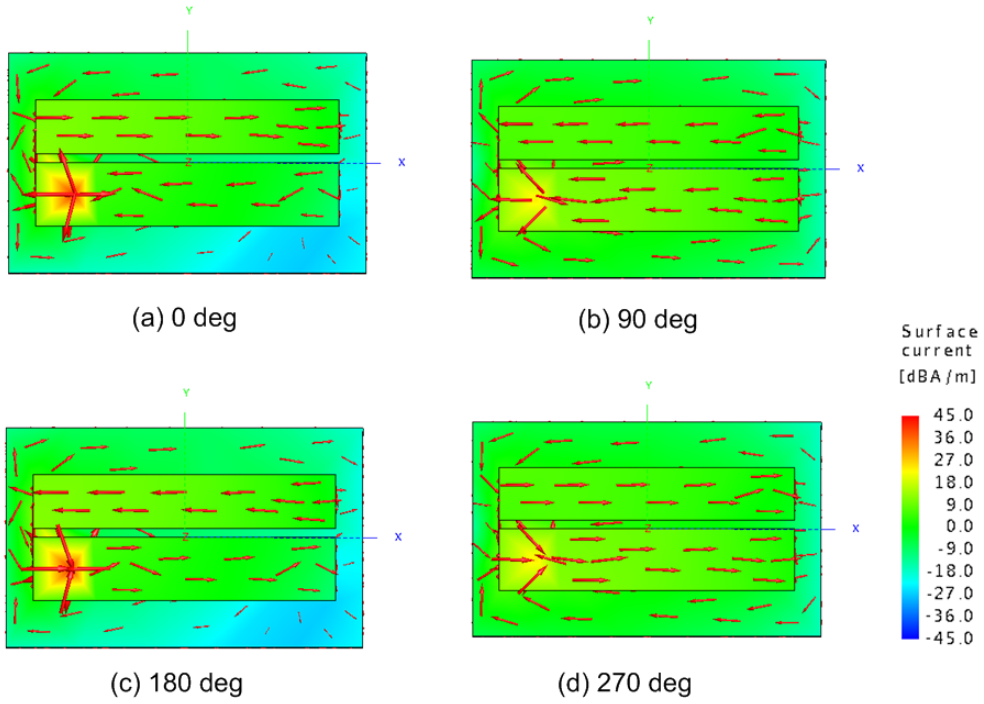


**Fig. 7.11. Surface current distributions on handheld PIFA geometry (shown in Fig. 7.7) for $\omega t$=[$0^o$,$90^o$,$180^o$,$270^o$]. Surface current calculations shown were obtained using FEKO.**

Bandwidth performance for antenna designs can be improved with the reduction of sharp edges, mechanically in the structural design of the antenna [3], and electrically, in terms of reducing the slope discontinuities in the surface current distributions [4]. Both the source-driven and parasitic elements share part of the shorting bar to increase coupling. The increased coupling balances the surface current distributions and minimizes asymmetries in the far-field radiation patterns.

Fig. 7.12 (a) and (b) are renderings of the tangential near-fields of the multi-resonant PIFA antenna mounted on the handheld chassis. Near-field intensities seen clearly on the side view show a significant increase at the capacitive-feed end of the PIFA. The near-field characteristic is similar to the current slope discontinuity seen at the end of a monopole. The remaining top-views shown in the figure indicates a balanced distribution of near-field energies in both the $E_\theta$ and $E_\Phi$ for $\omega t$ = [*0, 90, 180, 270*] degrees.

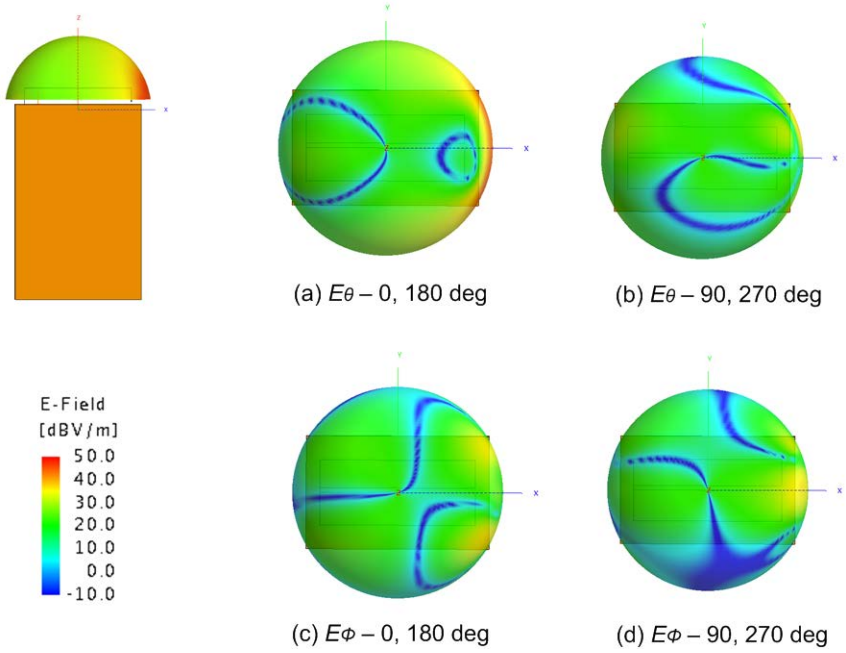


**Fig. 7.12. Tangential Near Fields in Spherical Coordinates for the handheld PIFA geometry (shown in Fig. 7.7) for $\omega t=[0^o,90^o,180^o,270^o]$. Near field calculations shown were obtained using FEKO.**

## 7.3 Summary

A passive, low-profile multi-resonant antenna element with monopole radiation characteristics has been introduced. The structure is an extension of the planar inverted-F antenna with a double-tuned structure to enhance reliable operation in unknown environments. Comparisons to a similar low-profile single-resonant antenna in both the finite ground plane and handheld geometries were shown. The source-driven element and parasitic are joined at the base of the shorting bar to improve the capacitive coupling. The result is a balanced element in terms of radiation and modal performance with a double-tuned impedance response and 2:1 VSWR bandwidth improvement of over forty- percent.

## 7.4 References

[1] G. Kumar, K.P. Ray, *Broadband Microstrip Antennas*, Artech House Inc., Boston 2003.

[2] M.C. Huynh, "Wideband Compact Antennas for Wireless Communication Applications," Ph.D. Dissertation, Virginia Tech Department of Electrical and Computer Engineering, Nov 22, 2004, pp. 28-35.

[3] W.L. Stutzman, G.A. Thiele, *Antenna Theory and Design*, 2nd ed. pp.250-270.

[4] T. Yang et al, "Cellular-Phone and Hearing-Aid Interaction: An Antenna Solution," IEEE Antennas and Propagation Magazine, vol. 50, No. 3, June 2008, pp. 51-64.

# 8 Chapter - Conclusions

## 8.1 Summary

A review of small antenna research was presented in Chapters 1 and 2. Chapter 2 reviewed the relation of antenna quality factor to the volume and height for radiating elements that easily fit within a radiansphere. Also discussed was the oscillatory relation of antenna impedance to the finite ground plane dimensions. Published work relating resonant length monopoles to finite ground planes was extended to consider the impedance characteristics of the short disk-loaded monopole. Low-profile single-resonant and wideband multi-resonant antennas were considered in the same context.

Chapter 3 proposed the restriction of electrically-small antennas to $ka \leq 0.5$ within the research community as too restrictive for practical applications. Very good wideband and self-resonant antennas exist in the $0.5 \leq ka \leq 1.0$ range with radiation properties typically characterized by an appreciable percentage of radiated power outside the lowest-order mode. The well-known expression (1) relating antenna quality factor to the

$$Q_{MIN} = \frac{1}{(ka)^3} \tag{1}$$

circumscribing radius assumes single-mode radiation and would be an incorrect small antenna metric for these examples. Chapter 3 proposed a combined approach of utilizing the quality factor extracted from impedance response data, in addition to near-and- far-field modal analyses, facilitates the analysis and characterization of ‘larger’ wide-bandwidth small antennas.

Chapter 4 observed the sensitivities of a single-resonant monopole and the planar inverted-F antenna are minimal in terms of modal content and bandwidth. The dominant majority of the far-field radiated power can be represented as combinations of $TM_{01}$ and $TM_{02}$ modes. A straightforward equivalent volume estimation method for bandwidth and quality factor was introduced with good agreement to results from fundamental limit theory. A low-profile planar inverted-F antenna with active impedance control was introduced, with comparisons between a simulation model and measured results for a prototype developed as part of an industrial

collaboration. The contrasts between the simulated and measured results indicate loss typical of radiation surface current and DC bias current path switch interaction.

Chapter 5 reviewed several simulation models of passive multi-resonant antennas and one ultra-wideband antenna to consider for wireless applications. Volume-efficient monopole-class antennas in addition to low-profile multi-resonant antennas were considered. The low-profile antennas incorporate different double-tuning structures, but a majority of their respective powers radiated outside the $TM_{0N}$ modes with peak power directed normal to the planar surface. The volume-efficient structures are optimal in terms of electromagnetic performance, but hardly acceptable for portable wireless applications.

In Chapter 6 the system integration of small antennas and portable power amplifiers was considered. An interesting modification of a single-resonant low-profile antenna to provide harmonic terminations for high-efficiency amplifiers was explored. Current, public-domain state-of-the-art active-switch tuning for reconfigurable antenna structures was also considered with published results similar to the experimental results in Chapter 4.

In Chapter 7 a passive, low-profile multi-resonant antenna element with monopole radiation characteristics was introduced. The structure is an extension of the planar inverted-F antenna with the addition of a capacitance-coupled parasitic to enhance reliable operation in unknown environments. The antenna is simple in construction, utilizes no loss or dielectric substrates, and is fully scalable. Favorable comparisons to a similar low-profile single-resonant antenna in both the finite ground plane and handheld geometries were shown.

The multi-resonant planar inverted-F antenna is an example of a fully-scalable, moderately low-profile ($h \approx \lambda/35$) antenna with a stable double-tuned impedance response. Active reconfigurable antennas with frequency-agility are attractive options to consider from the system level and may improve with advancing technology. But the antenna research community still struggles with the engineering challenge of isolating DC current paths from radiation-inducing surface currents.

Theoretical, simulated and measured results presented in the previous seven chapters support a fundamental conclusion reached for practical antenna design with current state-of-the-art microelectronics. A small-antenna design strategy with a cost function weighting a passive device with monopole class radiation, moderately low-profile structures, and multi-resonant

impedance response, ensures optimal and realizable performance of an efficient radiation element.

The current trend to incorporate of multiple-tuning structures (which may be considered the strategic utilization if volume) continues to show promise in the research and development of lossless small wideband antennas. State-of-the-art technology for active switching of reconfigurable antenna designs requires further development. However, the integration of a passive antenna to a high-efficiency power amplifier is a more promising path to commercial portable communication devices.

## 8.2 Contributions

The contributions of the dissertation research may be subcategorized into the theoretical and the practical. The theoretical contribution can be summarized by the development of an approach to analyze geometries for multi-resonant small antennas ($0.5 \leq ka \leq 1.0$), including both the half-power impedance bandwidth and direct evaluation of modal power distributions. Self-resonant wideband antennas with multiple applications exist in this range, and small antenna theory is typically limited to $ka << 0.5$. Application of the two accepted analysis tools, instead of the direct comparison of the antenna quality factor and its lower bound, is a straightforward approach to facilitate wideband small antenna characterization.

The practical contributions include the introduction of a fully scalable, passive, low-profile multi-resonant antenna element (see Fig. 7.1) characterized by monopole-class radiation. The antenna is simple in construction and utilizes no loss or dielectric substrates. A second practical contribution is the resultant compilation of small antenna simulation models all scaled to the same operation frequency and subjected to similar boundary conditions/near-field environments; see Chapters 4 and 5. A third practical contribution is the development of a near-field mode decomposition algorithm based upon Harrington [1] and Yang [2] that may be readily integrated to process measured spherical near-field scans data in addition to simulation output data files; see Chapter 3.

## 8.3 Future work

Three immediate areas for extending the research presented in this dissertation are immediately apparent. The first area for follow-on research and design would develop a commercial prototype development of the multi-resonant planar inverted-F antenna presented in Chapter 7. Additional parametric analyses of single and multiple parasitic configurations with the driven element would precede the development of initial prototypes and proof-of-concept models.

The likelihood of successful commercialization would increase if the low-profile multi-resonant design was modified for direct integration to a high-efficiency inverse class-F power amplifier. High-efficiency power amplifiers with small form-factors integrated to low-profile, multi-resonant antennas with enhanced bandwidths shift the small antenna research realm into viable market-driven applications.

The third potential application future research would be the integration and validation of the spherical mode decomposition algorithms for measured three-dimensional near-field data.

## 8.4 References

[1] R.F. Harrington, *Time-Harmonic Electromagnetic Fields*, McGraw-Hill, 1961

[2] Personal Notes from W.A. Davis and Taeyoung Yang